Vertical Silicon Nanowires for Image Sensor Applications

HARVARD UNIVERSITY
Graduate School of Arts and Sciences

DISSERTATION ACCEPTANCE CERTIFICATE

The undersigned, appointed by the

School of Engineering and Applied Sciences

have examined a dissertation entitled:

"Vertical Silicon Nanowires for Image Sensor Applications"

presented by : Hyunsung Park

candidate for the degree of Doctor of Philosophy and here by certify that it is worthy of acceptance.

Signature Ken Crozier

Typed name: Professor K. Crozier

Signature Fawwaz Habbal

Typed name: Professor F. Habbal

Signature T Zickler

Typed name: Professor T. Zickler

Signature R Wood

Typed name: Professor R. Wood

Date: September 5, 2014

Vertical Silicon Nanowires for Image Sensor Applications

A dissertation presented

by

Hyunsung Park

to

The School of Engineering and Applied Sciences

in partial fulfillment of the requirements

for the degree of

Doctor of Philosophy

in the subject of

Engineering Sciences

Harvard University

Cambridge, Massachusetts

September 2014

Dissertation Advisor
Kenneth B. Crozier

Author
Hyunsung Park

Vertical Silicon Nanowires for Image Sensor Applications

Abstract

Conventional image sensors achieve color imaging using absorptive organic dye filters. These face considerable challenges however in the trend toward ever higher pixel densities and advanced imaging methods such as multispectral imaging and polarization-resolved imaging. In this dissertation, we investigate the optical properties of vertical silicon nanowires with the goal of image sensor applications. First, we demonstrate a multispectral imaging system that uses a novel filter that consists of vertical silicon nanowires embedded in a transparent medium. Second, we demonstrate pixels consisting of vertical silicon nanowires with integrated photodetectors. We show that their spectral sensitivities are governed by nanowire radius, and perform color imaging. In addition, we demonstrate polarization-resolving photodetectors consisting of silicon nanowires with elliptical cross sections. Finally, we discuss a dual detector device. Each pixel consists of vertical silicon nanowires (incorporating photodetectors) formed above a silicon substrate (that also incorporates a photodetector). Our method is very practical from a manufacturing standpoint because all filter functions are defined at the same time through a single lithography step. In addition, our approach is conceptually different from current filter-based methods, as absorbed light in our device is converted to photocurrent, rather than discarded. This ultimately presents the opportunity for very high photon efficiency.

Contents

Title page i

Abstract iii

Table of contents iv

List of publications vii

Citations to previously published work ix

List of contributions x

Acknowledgements xii

Chapter 1 Introduction 1

1.1 Overview 1

1.2 Image sensor technologies: challenges and opportunities 2

1.2.1 Image sensor with higher efficiency 2

1.2.2 Multispectral imaging 5

1.2.3 Polarization-resolved imaging 6

1.3 Semiconductor nanowires 8

1.3.1 Synthesis of nanowires 9

1.3.2 Optical characteristics of absorbing horizontal nanowires 11

1.3.3 Optical characteristics of absorbing vertical nanowires 14

1.4 Structure of the dissertation 20

Chapter 2 Adding colors to polydimethylsiloxane by embedding vertical silicon nanowires 22

2.1 Method for transferring vertical silicon nanowires into PDMS 25

2.2 Optical characteristics of PDMS embedded silicon nanowires 28

2.3 Light absorption and scattering of silicon nanowires embedded in transparent medium 32

2.4 Conclusions 35

Chapter 3 Multispectral imaging with vertical silicon nanowires 36

3.1 Fabrication of silicon nanowire based multispectral filter 38

3.2 Characteristics of fabricated multispectral filter 42

3.3 Multispectral imaging experiment 46

3.4 Conclusion 52

Chapter 4 Filter-free image sensor pixels comprising silicon nanowires with selective color absorption 53

4.1 Fabrication of vertical silicon nanowires photodetector 54

4.2 Electrical measurement and optical simulation 62

4.3 Color imaging with nanowire based photodetectors 70

4.4 Conclusion 74

Chapter 5 Elliptical silicon nanowire photodetectors for polarization-resolved imaging 76

5.1 Vertical silicon nanowires photodetector with elliptical cross-section 77

5.2 Device characterization 82

5.3 Polarization-resolved imaging with elliptical nanowire photodetector 87

5.4 Conclusion 92

Chapter 6 Implementation of substrate photodetector for higher efficiency 93

6.1 Fabrication of dual detector device 94

6.2 Measurement of fabricated device 100

6.3 Conclusion 104

References 105

List of publications

Journals:

H. Park and K. B. Crozier, “Elliptical silicon nanowire photodetectors for polarization-resolved imaging” (submitted).

H. Park, Y. Dan, K. Seo, Y. J. Yu, P. K. Duane, M. Wober and K. B. Crozier, “Filter-free image sensor pixels comprising silicon nanowires with selective color absorption,” *Nano Letters*, vol. 4, 1804-1809 (2014).

K. B. Crozier, H. Park, K. Seo, P. Steinvurzel, E. Schonbrun, Y. Dan, T. Ellenbogen, P. Duane and M. Wober, “Research highlights harnessing the nano-optics of silicon nanowires for multispectral imaging,” *IEEE Photonics Society News*, vol. 27, 11-18 (2013).

H. Park, K. Seo and K. B. Crozier, “Multispectral imaging with vertical silicon nanowires,” *Scientific Reports*, vol. 3, 2460 (2013).

Y. M. Song, Y. Xie, V. Malyarchuk, J. Xiao, I. Jung, K. J. Choi, Z. Liu, H. Park, C. Lu, R. H. Kim, R. Li, K. B. Crozier, Y. Huang and J. A. Rogers, “Digital cameras with designs inspired by the arthropod eye,” *Nature*, vol. 497, 95-99 (2013).

S. J. Koppal, I. Gkioulekas, T. Young, H. Park, K. B. Crozier, G. L. Barrows and T. Zickler, Toward wide-angle microvision sensors, *IEEE Transactions on Pattern Analysis and Machine Intelligence (TPAMI)*, vol. 35, 2982-2996 (2013).

K. Seo, Y. J. Yu, PK Duane, W. Zhu, H. Park, M. Wober and K. B. Crozier, "Si microwire solar cells: improved efficiency with a conformal SiO_2 layer," *ACS Nano*, vol. 7, 5539-5545 (2013).

H. Park, K. Seo and K. B. Crozier, "Adding colors to polydimethylsiloxane by embedding vertical silicon nanowires," *Applied Physics Letters*, vol. 101, 193107 (2012).

Conference presentations:

H. Park and K. B. Crozier, "Polarization-resolved imaging using elliptical silicon nanowire photodetectors," *Conference on Laser and Electro-Optics (CLEO)*, San Jose, CA, Paper FTh4I.5 (2014).

H. Park, Y. Dan, K. Seo, Y. J. Yu, P. K. Duane, M. Wober and K. B. Crozier, "Vertical silicon nanowire photodetectors: spectral sensitivity via nanowire radius," *Conference on Laser and Electro-Optics (CLEO)*, San Jose, CA, Paper CTh3L.5 (2013).

H. Park and K. B. Crozier, "Multispectral imaging using PDMS embedded vertical silicon nanowires," *Conference on Laser and Electro-Optics (CLEO)*, San Jose, CA, Paper CTu3O.1 (2013).

H. Park, K. Seo and K. B. Crozier, "Polymer-embedded arrays of vertical silicon nanowires as color filters," *Conference on Laser and Electro-Optics (CLEO)*, San Jose, CA, Paper CM3M.5 (2012).

Citations to previously published work

Chapter 2 has been published as

> H. Park, K. Seo and K. B. Crozier, "Adding colors to polydimethylsiloxane by embedding vertical silicon nanowires," *Applied Physics Letters*, vol. 101, 193107 (2012).

Chapter 3 has been published as

> H. Park, K. Seo and K. B. Crozier, "Multispectral imaging with vertical silicon nanowires," *Scientific Reports*, vol. 3, 2460 (2013).

Chapter 4 has been published as

> H. Park, Y. Dan, K. Seo, Y. J. Yu, P. K. Duane, M. Wober and K. B. Crozier, "Filter-free image sensor pixels comprising silicon nanowires with selective color absorption, " *Nano Letters*, vol. 4, 1804-1809 (2014).

Chapter 5 has been submitted as

> H. Park and K. B. Crozier, "Elliptical silicon nanowire photodetectors for polarization-resolved imaging," (submitted).

List of contributions

1. We developed a fabrication method for embedding silicon nanowires into polydimethylsiloxane (PDMS). This presents a means for adding color to PDMS. Silicon nanowires are etched from a silicon wafer and transferred to a PDMS film. Each measured transmission spectrum exhibits a dip at a wavelength determined by the nanowire radius.

2. We demonstrate of a compact multispectral imaging system that uses vertical silicon nanowires to realize a filter array. Multiple filter functions covering visible to near-infrared wavelengths are simultaneously defined in a single lithography step on a silicon wafer. Nanowires are then etched and embedded into polydimethylsiloxane (PDMS), thereby realizing a device with eight filter functions. By attaching this device to a monochrome silicon image sensor, we realize an all-silicon multispectral imaging system. We demonstrate visible and near-infrared (NIR) imaging.

3. We invent a new method for color imaging based on all-silicon nanowire devices and no filters. We fabricate pixels consisting of vertical silicon nanowires with integrated photodetectors, demonstrate that their spectral sensitivities are governed by nanowire radius, and perform color imaging. Our approach is conceptually different from filter-

based methods, as absorbed light is converted to photocurrent, ultimately presenting the opportunity for very high photon efficiency.

4. We present a new type of image sensor pixel for polarization-resolved imaging based on an all-silicon nanowire device. We fabricate pixels consisting of vertical silicon nanowires with elliptical cross sections that incorporate vertical p-i-n junctions. We demonstrate that the absorption spectrum of our device depends on whether the incident light is polarized along the long or short axis of the elliptical cross section, and perform polarization-resolved imaging.

5. We fabricate a dual detector device that contains both nanowire and substrate photodetectors. The nanowire photodetector absorbs light in a spectrally-selective manner. The light not absorbed by the nanowires is largely transmitted into the substrate. The incorporation of a second photodetector in the substrate to convert this light to photocurrent could permit image sensor pixels with very high efficiency.

Acknowledgements

It is impossible to thank all people who contribute to this dissertation in many ways. I really appreciate all of them. Without their support, I could not have finished my dissertation. First of all, I would like to thank my advisor Prof. Kenneth B. Crozier for his guidance, absolute support, encouragement, endless source of knowledge and advice. He leads me to the world of nanowires. Thank you for all wonderful discussions we had.

I would like to thank Prof. Fawwaz Habbal, Prof. Todd Zickler and Prof. Robert J. Wood for being my PhD committee member. They provided valuable advice and comments on my work. Thank you Prof. Habbal especially for discussions and support during this summer.

I would like to thank all present and past members in the Crozier group. I am particularly grateful to Yaping and Kwanyong for their generous help. Their knowledge and experience is essential for my research. I would like to thank Wenqi, Dongxing, Tony, Shiyun, Yuhang, Kai, Yizhuo, Paul, Ethan, Turgut, Tal, Amit, Wuzhou and Reza. I really enjoyed talking, discussions and atmosphere. I would like to thank Young, Peter, Munib in Zena Technologies for very helpful discussions. I would like to thank all my friends in Cambridge includes my ELP Korean friends. It is great knowing all of you. Lingbo, thank you for everything. I am so happy that you are in my life. I dedicate this dissertation to my parents and sister. I would never be able to make this without their love and support.

Chapter 1 Introduction

1.1 Overview

Just as the human eye has a crystalline lens and a light sensitive retina, the digital camera has a glass lens and a semiconductor-based image sensor. Image sensors convert information carried by light to electrical signals. In a digital camera, these electrical signals are processed, recorded in memory (usually solid state), and displayed on a screen. Due to this convenience, the market share enjoyed by digital cameras has rapidly expanded in recent years meaning that, at the time of writing, it dwarfs that of traditional film cameras. Although there has been huge progress in the image sensor technology, still there is tremendous scope for improvement. For example, higher resolution images are desired by consumers meaning that, if the sensor size is kept constant, the pixel size must be scaled down. This results in a decrease in the light impinging on each pixel. To exacerbate this problem, the majority of digital cameras are in mobile devices such as laptop computers, cell phones and tablets. These require the camera modules to be as small and light as possible, meaning that, in turn, the image sensor needs to be as small as possible without sacrificing image quality. This challenges manufacturers to develop image sensor pixels that are smaller, with higher efficiency and with lower noise. Another trend is that image sensors are expanding beyond mimicking human vision into modalities that include multispectral and polarization-resolved

imaging. This is due to the advantages that these modalities offer for applications such as surveillance, automation and robot vision. The work described in this dissertation is focused on the use of silicon nanowires to improve the efficiency and functionality of image sensors. Specifically, we demonstrate a new type of image sensor pixel using vertical silicon nanowires.

1.2 Image sensor technologies: challenges and opportunities

1.2.1 Image sensor with higher efficiency

Conventional image sensors achieve color imaging using color filters based on organic dyes. These color filters are situated between the microlenses and photodetectors (Figure 1.1), and typically transmit red, green and blue spectral bands. These filters face considerable challenges[1] however in the trend toward ever higher pixel densities. The filters are inherently inefficient, in that they only transmit a portion of the visible spectrum, yet as discussed in the previous section, high pixel densities are generating the strong need for improved efficiency. This is evidenced by the introduction of back side illumination devices. In front-side illumination devices (Figure 1.1(a)), light can be reflected or scattered by the metal interconnection layers. Back side illumination devices were developed to reduce this source of loss.(Figure 1.1(b)) In the beginning of the fabrication process, the back side illumination device has same structure as front side illumination device. The photodetector

and interconnection layers are fabricated. At this point, for the back side illumination device, the wafer is flipped and substrate is thinned until the photodetectors are exposed. After that, the color filters and microlenses are fabricated on the thinned surface. This allows each pixel to collect more photons because there are no metal layers in the light path.

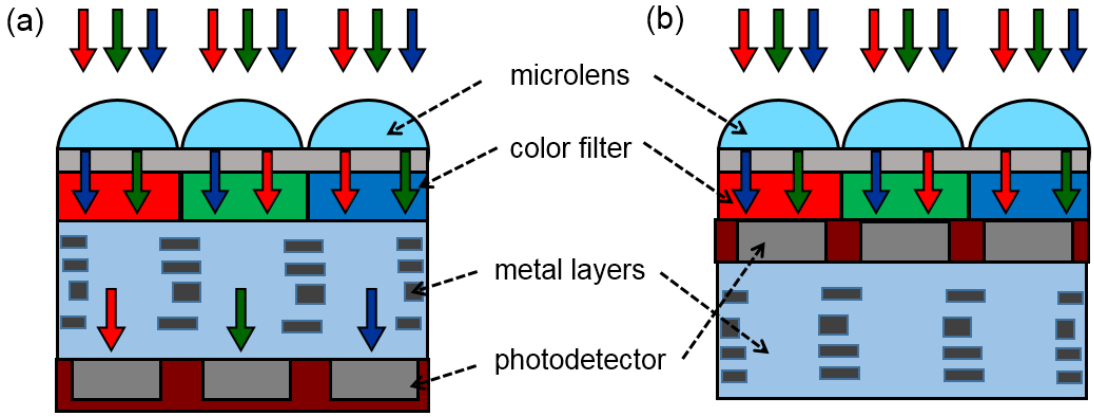

Figure 1.1 Conventional image sensor. (a) Front side illumination. (b) Back side illumination

Although back side illumination achieves higher efficiency, the color filter still poses a limitation in the scaling down of the pixels. The absorption coefficients of organic dyes set a lower bound to filter thickness, limiting the realization of very small pixels. In addition, organic dye filters degrade under ultraviolet illumination and at high temperatures. There is therefore currently considerable interest for alternative approaches. Plasmonic color filters present the advantages that the spectral response can be determined flexibly and that only one material is needed.[1-3] However, the basic approach is unchanged from that used with organic dyes: color filters transmitting certain wavelengths are formed on the detectors. The wavelengths that are not transmitted are absorbed or reflected. Ideally, to maximize

efficiency, we would instead prefer this light to be converted to photocurrent. To this end, image sensors based on color splitting have been proposed.[4] Another approach has been to make use of the wavelength-dependent absorption length of light in silicon (Foveon X3® image sensor, [5]).

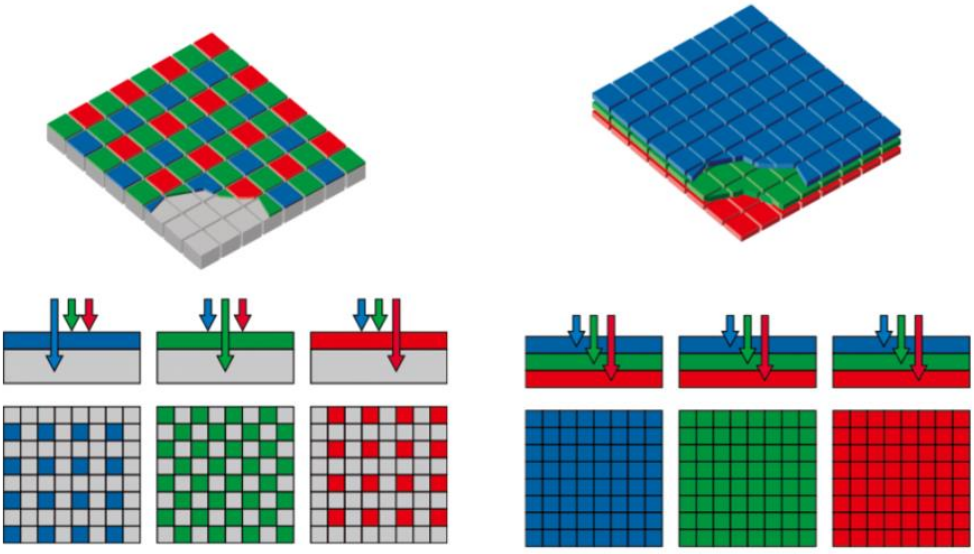

Figure 1.2 The comparison between conventional color filter array based color image sensor and Foveon X3® image sensor. Figure adapted from Reference [6].

Figure 1.2 presents a concept-level comparison between a normal color image sensor and the Foveon X3® image sensor. The Foveon X3® image sensor has vertically stacked photodetectors, while normal image sensor a two dimensional array of photodetectors and color filters. Each pixel of the Foveon image sensor can detect all three primary colors and there is therefore no need for the interpolation process that causes degradation of image sharpness in conventional image sensors. However, the Foveon X3® image sensor has a large overlap in the spectral response of three channels.[7] For example, the blue photodetector (top photodetector) has much wider spectral response than blue channel in the

tristimulus function. Although post processing using an appropriate color matrix can generate the correct color, the large off-diagonal terms of the color matrix add noise to the image. In addition, pixel size of the Foveon X3® image sensor is relatively large by comparison to conventional image sensors, which is probably due to the pixel structure being more complicated.

1.2.2 Multispectral imaging

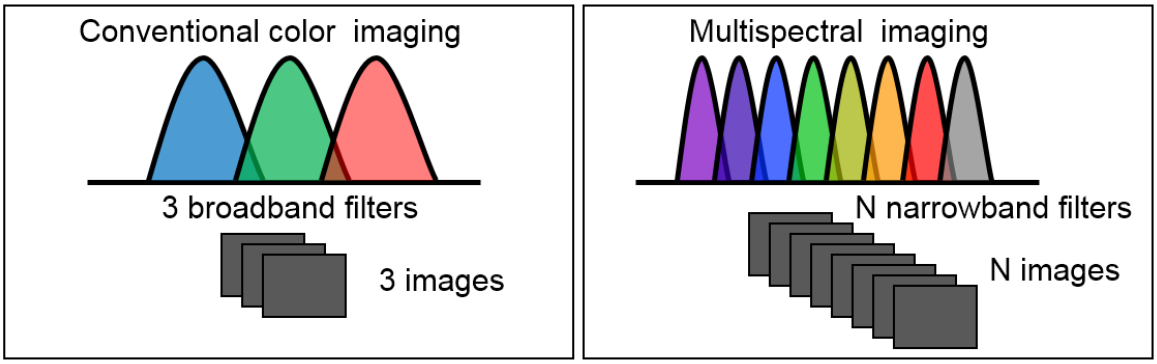

Figure 1.3 Color imaging and multispectral imaging.

In multispectral imaging, the spectrum is divided into multiple bands, enabling materials or objects in a scene to be identified from the characteristics of their absorption or reflection spectra. The conceptual difference between conventional color imaging and multispectral imaging is illustrated in Figure 1.3. Multispectral imaging generally employs multiple narrow band spectral filters, with each capturing a different portion of the spectrum. This approach permits many applications, including remote sensing[8], vegetation mapping[9], non-invasive biological imaging[10], food quality control[11] and face recognition[12]. Multispectral imaging systems generally use motorized filter wheels[13], multiple

cameras[14], line-scanning[15] or tunable filters[16] to obtain images in multiple spectral bands. Despite this wide range of uses, relatively few commercial systems are available and most are complicated, expensive and bulky. To address these limitations, several approaches based on filter arrays have been proposed [17, 18]. An array of containing four NIR filter functions was demonstrated. Because these filters were dielectric interference designs, however, the fabrication process was relatively complicated as the deposition of multiple dielectric layers was required for the realization of each filter function. Furthermore, this process had to be repeated to achieve the four filter functions. Plasmonic structures have also been proposed for color filtering [1-3, 19].

1.2.3 Polarization-resolved imaging

Although the human eye can perceive the color of visible light, it is not sensitive to its polarization. By contrast, in other parts of the animal kingdom, eyes have evolved with polarization sensitivity.[20-23] Polarization provides important additional information on materials and scenes because it is affected by material characteristics, surface curvature, the angle of incident light, as well as other factors. For example, objects with minimal intensity variation are often much more readily discerned via their degree-of-linear polarization [24, 25], as this is sensitive to surface curvature via the Fresnel reflection coefficients. These considerations have motivated the development of polarization-resolved imaging techniques for applications ranging from biological studies to remote sensing.[26-30]

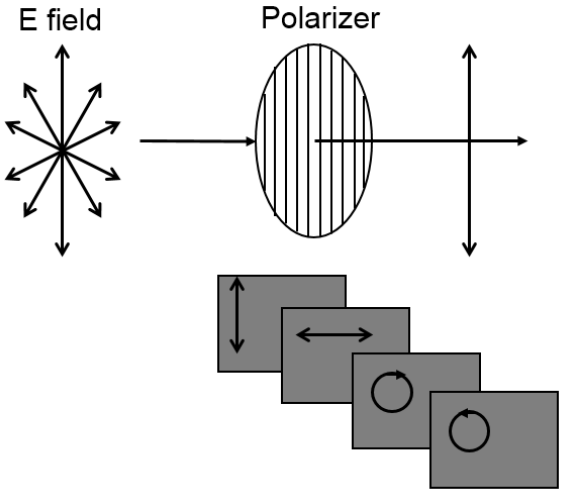

Figure 1.4 Polarization-resolved imaging

One simple way to capture a polarization-resolved image involves mounting a polarizing filter in front of a camera, mechanically rotating it to different orientations, and taking an image at each. Figure 1.4 shows the basic method of polarization-resolved imaging. In many cases, one would prefer to avoid mechanical rotation due to speed considerations. This has motivated the use of electrically-controlled liquid crystal polarization filters.[31, 32] The bulk and speed limitations of this approach however will be problematic for many applications (e.g. imaging fast moving objects), despite being an improvement over the mechanical rotation of a polarization filter. The integration of micro-polarization filters directly onto the image sensor is one solution to these limitations.[24, 33-36] This approach is analogous to the use of Bayer color filters in image sensors, and enables the realization of compact systems that can perform polarization-resolved imaging at the frame rate of the image sensor, i.e. there is no temporal overhead associated with filter rotation, et.c. These devices are inherently inefficient, however, as they function by absorbing or reflecting the unwanted polarization. The light being absorbed in the polarization filter cannot be captured.

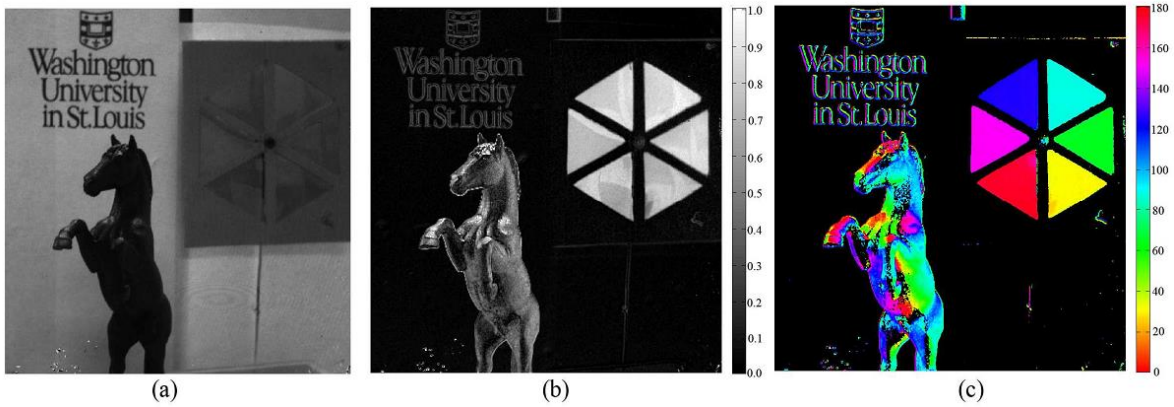

Figure 1.5 Polarization-resolved imaging example: (a) conventional imaging (b) degree of linear polarization (c) angle of polarization. Figure adapted from Reference [24].

The Figure 1.5 shows an example of polarization resolved imaging of a scene that consists of a black plastic horse figure and a polarizer that has been cut into six segments and arranged so that the orientation of the polarization axis of each segment is different. A conventional (i.e. intensity-based) image of the scene is shown as Figure 1.5(a). It can be seen that the shape of the horse figure is difficult to determine. On the other hand, the shape is much more easily ascertained in the degree of linear polarization image.(Figure 1.5(b)) Similarly, the orientation of the polarization axes of the polarizer segments can be seen in the angle of polarization image (Figure 1.5(c)).

1.3 Semiconductor nanowires

In this dissertation, we address the challenges and opportunities for image sensors discussed in Section 1.2 through the use of nanotechnology. Nanoscale materials can exhibit properties that differ from those of bulk materials, presenting opportunities for new

applications. Here, we investigate semiconductor nanowires. These have been widely studied [37-42], but we employ them in novel ways for image sensors.

1.3.1 Synthesis of nanowires

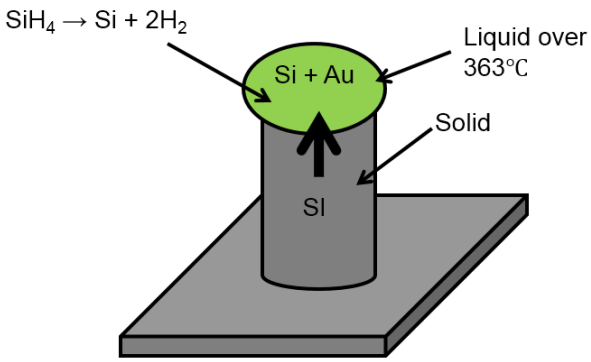

Figure 1.6 VLS growth nanowire method.[43]

Silicon nanowires are normally grown by the vapor-liquid-solid (VLS) mechanism (Figure 1.6, [43]). The VLS method uses gas precursors and metal catalyst. The position that the nanowire grows is determined by the position of the catalyst. Generally, there are three way to prepare the catalyst. The first is the thin-film method, in which a thin gold film is deposited then annealed, resulting in the formation of gold islands. The second method consists of placing gold particles, e.g. prepared by chemical synthesis, on the surface. The third method comprises gold deposition and lithographic patterning. Each catalyst particle (gold island) reacts with silicon, forming Au-Si alloy droplets when the temperature exceeds 363℃. This temperature is very low compared with the melting points of silicon and gold. Next, the precursor gas, i.e. silane (SiH_4) or tetrachlorosilane ($SiCl_4$), is injected. Au-Si

droplets absorb silicon from gas precursor until they are saturated, resulting in nucleation of silicon atoms at the liquid-solid interface. As this process continues, silicon nanowires are grown in areas containing metal catalyst. Importantly, the direction in which the nanowires grow is determined by the crystal orientation of the substrate. Vertical nanowires can be therefore synthesized if a silicon <111> wafer is used for substrate. The diameters of the nanowires are determined by the sizes of the gold catalyst particles. Figure 1.7 shows silicon nanowires grown by the author using the VLS method in the Harvard Center for Nanoscale Systems. We use the thin-film method, meaning that gold islands have non-uniform sizes. This leads grown silicon nanowires with a range of radii. In addition, the process results in the nanowires having random orientations. In other works, the growth of highly ordered vertical silicon nanowires was demonstrated using silicon tetrachloride ($SiCl_{4)}$ as a precursor gas.[44, 45] $SiCl_4$ often yields better control over the growth because the hydrogen chloride (HCl) produced cleans the surface of the substrate as the growth proceeds. However, the use of $SiCl_4$ requires higher process temperatures.

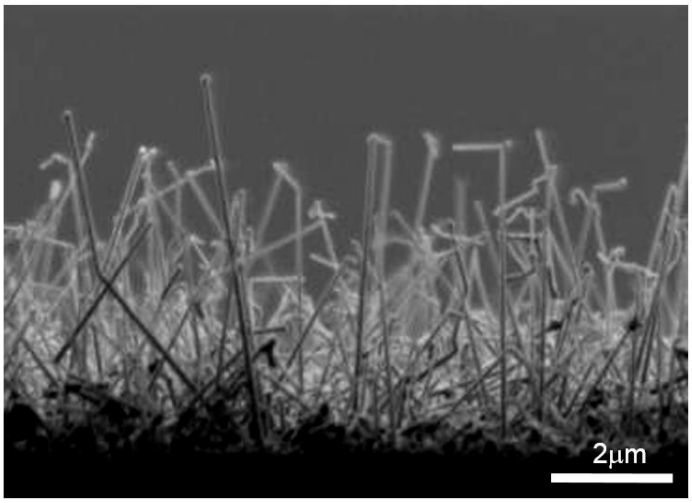

Figure 1.7 Silicon nanowires grown by the author using the VLS method. We use low pressure chemical vapor deposition (LPCVD) system with silane gas mixture (5 % silane, 95 % hydrogen). The gas flow rate is 100 sccm. Process temperature is 550 ℃ and growth time is 30 minutes.

1.3.2 Optical characteristics of absorbing horizontal nanowires

Nanomaterials such as quantum dots exhibit optical properties that differ from those of bulk materials due to quantum confinement effects. For the nanowires considered in this dissertation, however, quantum confinement effects are not applicable. Indeed, we take the silicon nanowires to have complex permittivity equal to that of bulk silicon. Interestingly however, the silicon nanowires considered here nonetheless have optical characteristics that differ substantially from bulk silicon. In particular, the absorption spectrum of bulk Si is determined by its complex permittivity, which is strongly dependent on its bandgap. The silicon nanowires considered in this dissertation however have radii that are smaller than the wavelength. Light therefore interacts very differently with silicon nanowires than it does with bulk silicon, leading to particularly different scattering and absorption spectra. Two

configurations that are instructive for understanding light-nanowire interactions are the cases of the nanowires being oriented horizontally (i.e. parallel to substrate) and vertically (i.e. perpendicular to substrate). We consider the first case in this section. The second case is considered in the next section.

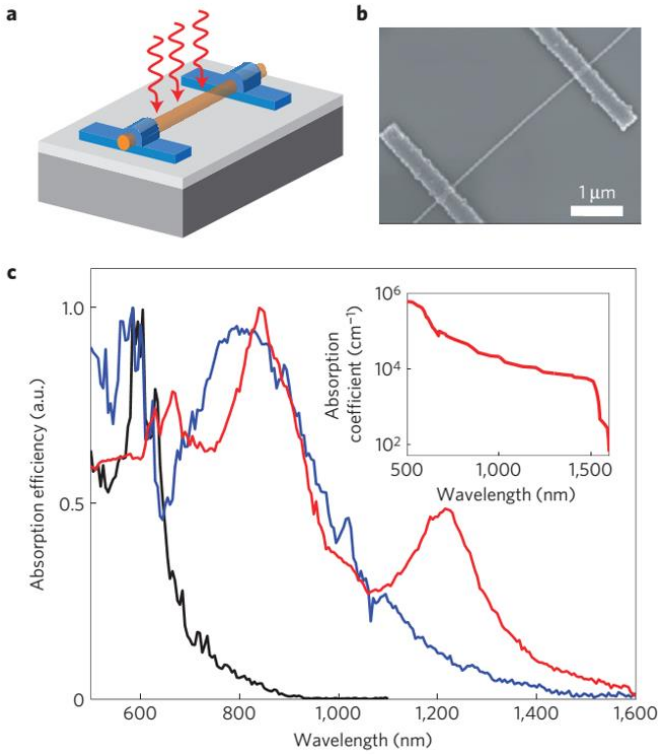

Figure 1.8 Measurement of light absorption by horizontal germanium nanowires. (a) Schematic of the germanium nanowire device (b) SEM image of nanowire with radius of 25 nm. (c) Measured absorption spectra of nanowires with the radii of 10 nm (black), 25 nm (blue) and 110 nm (red). From Reference [46].

Cao *et al* showed that horizontal germanium semiconductor nanostructures have leaky-mode resonances.[46] The manner with which these resonances confine light within a nanowire strongly depends on its size. This enables one to engineer the absorption of light

by nanowires, which could be useful for applications that include photodetectors.[47] Results obtained by Cao *et al* on the light absorption by individual germanium nanowires with different radii are shown in Figure 1.8. These results were obtained as follows. Germanium nanowires were grown by the VLS method. A nanowire was then placed on the substrates and metal contacts were established, with the end result shown in the scanning electron microscopy image of Figure 1.8(b). Light from a supercontinuum source was coupled to a monochromator. The light from the monochromator was focused onto the nanowire device. This allowed the photocurrent to be measured as a function of wavelength, and the absorption efficiency was found (in arbitrary units, Figure 1.8(c)), under the assumption that the internal quantum efficiency did not vary with wavelength. It can be seen from Figure 1.8(c) that the germanium nanowires have absorption spectra that are highly dependent on nanowire radius. This comes from the leaky mode resonances in which light is highly confined to the nanowire, resulting in enhanced absorption. A schematic illustration of such a leaky mode resonance is shown as Figure 1.9(a). The incident light couples to the nanowire and then circulates around the nanowire's circumference due to total internal reflection. At resonance, there is constructive interference between the incident light and that already circulating in the nanowire. This description is helpful for physical interpretation. For quantitative results, the leaky mode resonance of a nanowire can be calculated using Maxwell's equations with appropriate boundary conditions [46]. Although germanium has high refractive index, the nanowire supports a limited number of resonance modes, due to its small size. The resonance modes can be divided into transverse electric (TE) and transverse magnetic (TM) modes (Figure 1.9(b)). Absorption peaks occur near the leaky mode

resonances. The bottom of Figure 1.9(b) shows electric field intensity distributions of several transverse magnetic modes of the horizontal germanium nanowire. It can be seen that the electric fields are well-confined to the nanowire.

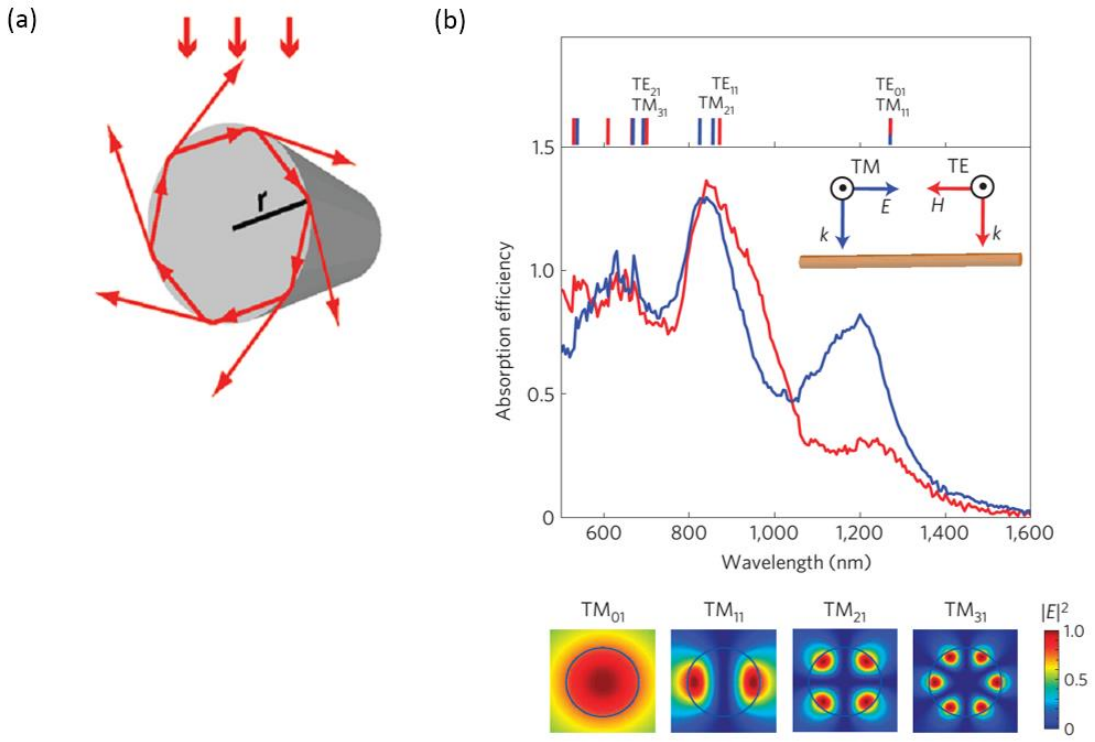

Figure 1.9 (a) Illustration of resonance mode in the nanowire. From Reference [47]. (b) Absorption efficiency of germanium nanowire (arbitrary units) under TM and TE illumination. Peaks correspond to leaky mode resonances, whose locations are shown as blue and red ticks above the spectrum. Nanowire has radius of 100 nm. Bottom: picture shows electric field intensity for transverse-magnetic leaky modes. From Reference [46].

1.3.3 Optical characteristics of absorbing vertical nanowires

While the VLS method produces highly quality nanowires, it does so with less control of the size, position and direction than would be desirable for many applications. By contrast, through lithography and etching, nanowires can be produced with precise control over

position, radius and length. Our group previously demonstrated that etched vertical silicon nanowires show vivid colors. This is a consequence of peaks in their absorption spectra that arise from the wavelength-dependence of the spatial distribution of the waveguide modes that they support.[48] The fabrication process employed in that work [48] was as follows. The starting substrate was a silicon wafer. Electron beam lithography was performed to define circular openings in the resist. Aluminum evaporation and the lift-off process were performed to produce a metal etch mask. Inductively-coupled plasma reactive ion (ICP-RIE) etching was used to etch the nanowires. The aluminum mask was then removed by wet etching. A scanning electron microscope image of nanowires with radii of 45 nm and heights of 1 μm is shown as Figure 1.10 (left). The pitch of nanowire array is 1 μm. We can see that the etching method provides excellent control over the geometrical parameters of the nanowires. An optical microscope image of arrays of vertical silicon nanowires with different radii is shown as Figure 1.10 (middle). It can be seen that the nanowire arrays have vivid colors. The reflection spectra measured from the nanowire arrays are shown as Figure 1.10 (right). It can be seen that each reflection spectrum shows a dip. This corresponds to the wavelength at which the nanowire absorption is maximized.

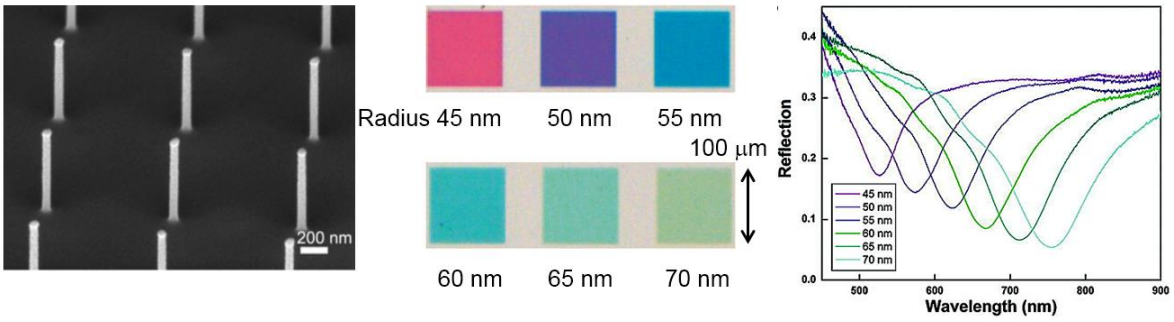

Figure 1.10 Etched vertical silicon nanowires. Figure adapted from Reference [48].

It is important to realize that the fact that the nanowires have color does not originate from grating-type effects. Rather, it comes from the wavelength-dependence of the spatial field distribution of the fundamental guide mode (HE_{11} mode) supported by each nanowire. The interaction between incident light and a vertical silicon nanowire is illustrated as Figure 1.11(a). A portion of the incident light can couple to the nanowire's mode, then propagate along it, being absorbed in the process. The light arriving at the air-substrate is reflected or transmitted.

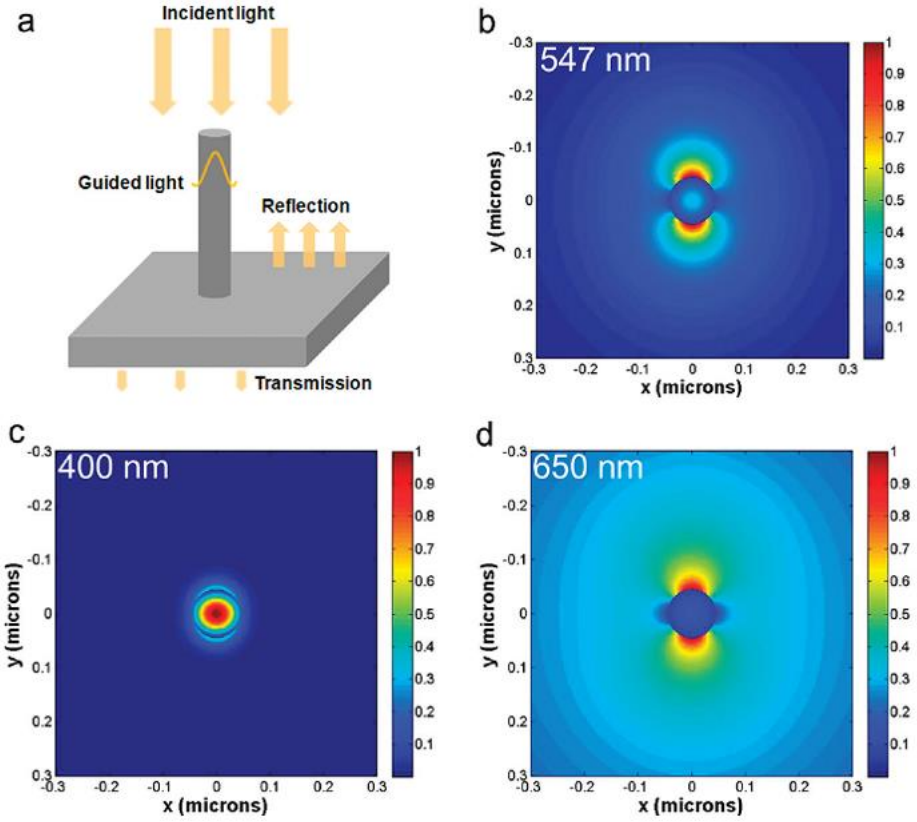

Figure 1.11 Wavelength selective coupling mechanism in vertical silicon nanowire arrays. (a) Illustration of wavelength-selective waveguiding system. (b-d) Electric field distributions (major transverse component, E_y) of fundamental mode of a 45 nm radius silicon nanowire for wavelengths of 547, 400, and 650 nm, respectively. From [48].

The simulation results shown in Figure 1.11 enable us to understand the wavelength-dependence of light absorption in vertical silicon nanowires. In Figure 1.11 (b-d), the spatial profiles of the major transverse component of the HE_{11} mode are shown at three different wavelengths. In all cases, the nanowire's radius is 45 nm. At a wavelength of 400 nm (Figure 1.11 (c)), the mode is tightly confined to the nanowire. The spatial mode overlap between the incident light and the nanowire is therefore low, leading to the coupling efficiency between the incident light and the nanowire's fundamental mode being poor. The absorption of light by the nanowire is therefore low at this wavelength. In Figure 1.11(d), the spatial field distribution is shown for illumination at a free space wavelength of 650 nm. It can be seen that the mode is not very confined to the nanowire. Although this results in a large spatial mode overlap, and therefore efficient excitation, a large portion of the guided light is located outside the nanowire. This results in low absorption in the nanowire. In contrast, at some intermediate wavelength (Figure 1.11(b)), the mode can be both efficiently excited by the incident light and have appreciable fields within the nanowire. This leads to the absorption being maximized. When the nanowire radius is increased, the wavelength at which the maximum absorption occurs red-shifts. In this dissertation, we will use this phenomenon, i.e. of wavelength-selective absorption by silicon nanowires, for various image sensor applications.

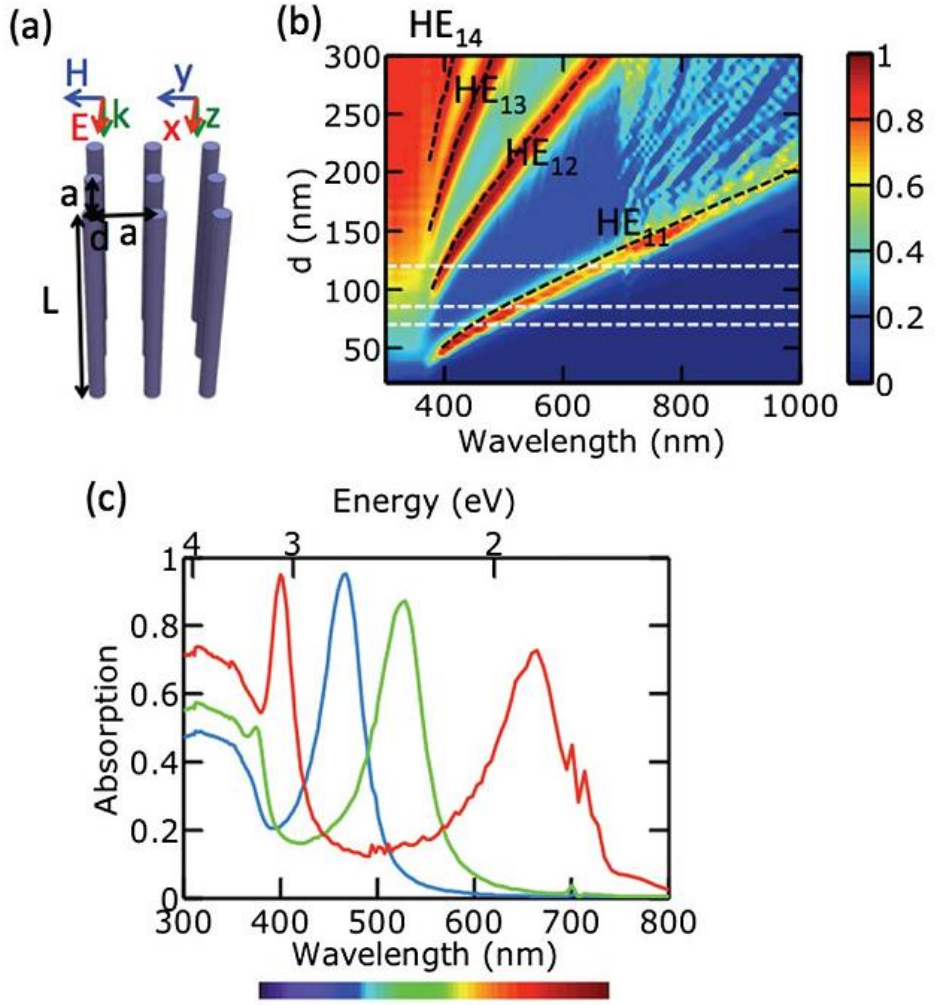

Figure 1.12 (a) Vertical silicon nanowire array (b) Absorption as a function of wavelength and diameter of nanowire (c) Absorption spectra of nanowires with diameters of 70 nm (blue curve), 85 nm (green curve) and 120 nm (red curve). From Reference [49].

The work described above was primarily concerned with the fundamental mode of vertical silicon nanowires in the visible wavelength region. In general, absorption peaks also appear due to coupling to higher order modes. Wang *et al* studied this by numerical simulations and optical waveguide theory.[49] They showed that light incident on vertical silicon nanowires excites HE_{1m} modes, resulting in absorption peaks. They explained this as

coming from symmetry matching conditions. If the incident light is polarized in the x-direction (Figure 1.12(a)), the electrical field is anti-symmetric under reflection about the $y-z$ plane. This means that the modes that are anti-symmetric under reflection about the $y-z$ plane have the possibility of efficient coupling to the incident light. The HE_{1m} modes satisfy this condition. Figure 1.12(b) shows calculated absorption spectra of vertical silicon nanowires as a function of nanowire diameter. Peaks corresponding to higher order modes (HE_{12}, HE_{13}) appear as the nanowire diameter increases. The data along the dashed white lines of Figure 1.12(b) are re-plotted as Figure 1.12(c). The nanowire with diameter of 120 nm has an absorption peak originating from the HE_{11} mode but also one originating from the HE_{12} mode. Figure 1.13 shows the electric field intensity distributions corresponding to these two modes along top- ($x-y$ plane) and side-views ($x-z$ plane). The HE_{11} mode for excitation with light with a free-space wavelength of 670 nm is shown as Figure 1.13 (a). Figure 1.13 (b) shows the HE_{12} mode for excitation with light with a free-space wavelength of 400 nm.

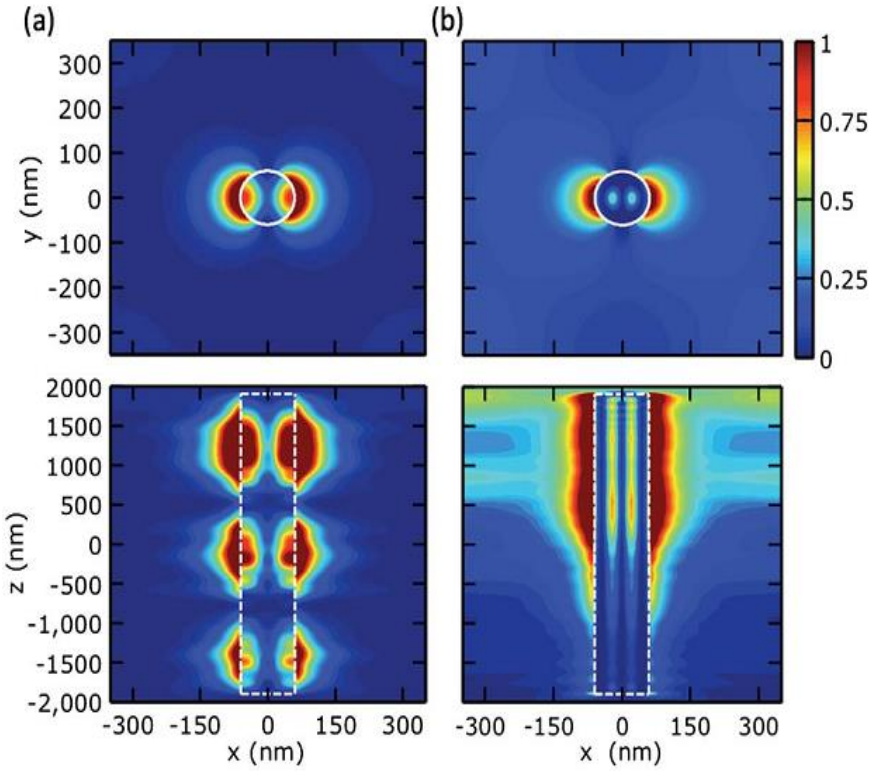

Figure 1.13 Electric filed intensity plots for silicon nanowire with diameter of 120 nm. (a) Wavelength of incident light is 670 nm. (HE_{11} mode) (b) Wavelength of incident light is 400 nm. (HE_{12} mode). From Reference [49].

1.4 Structure of the dissertation

The remaining chapters of the dissertation contain the following topics.

Chapter 2 describes a method I developed to transfer vertical silicon nanowires into a transparent medium (polydimethylsiloxane). This enables us to demonstrate optical filters based on the fact that the transmission spectra of the nanowires are governed by their radii.

Chapter 3 describes multispectral imaging experiments performed using the optical filters developed in Chapter 2. These are performed by attaching the filter to a monochrome image sensor.

Chapter 4 describes the demonstration of a conceptually-new type of image sensor pixel comprising silicon nanowire photodetectors (p-i-n junction) with selective color absorption. We perform color imaging using our device. This makes use of our ability to control the nanowire absorption spectrum by choice of nanowire radius, and no additional color filters are needed.

Chapter 5 describes our demonstration of polarization-resolved imaging using photodetectors formed in silicon nanowires with elliptical cross sections. We demonstrate that the absorption spectrum of our device depends on whether the incident light is polarized along the long or short axis of the elliptical cross section, and perform polarization-resolved imaging.

Chapter 6 describes our demonstration of a dual photodetector device that presents the opportunity for higher efficiency image sensor pixels. The device consists of an array of nanowires containing photodetectors. In addition, a photodetector is integrated into the substrate, i.e. below the nanowires. This enables us to collect the photons not absorbed by the nanowires.

Chapter 2

Adding colors to polydimethylsiloxane by embedding vertical silicon nanowires

Due to a range of exciting possibilities, numerous investigations have been made of silicon nanowires.[50-52] It is therefore surprising how little attention has been generally paid to their optical properties, particularly to the dramatic effects that arise from resonance and waveguiding phenomena. In the previous work, it was shown that vertical silicon nanowires take a surprising variety of colors, spanning the visible spectrum.[48] The effect arose from the guided mode properties of the individual nanowires, not from scattering or diffractive effects of the array. They could be readily observed in bright-field microscopy, or even with the naked eye. In that work, however, the nanowires were on a silicon substrate. Many applications, for example color filters, would be enabled by having the nanowires on a substrate that is transparent at visible and near-infrared wavelengths. This is the subject of this Chapter.

Polydimethylsiloxane (PDMS) is chosen as the substrate into which the silicon nanowires are transferred for several reasons. PDMS is a soft elastomer and can undergo large deformation, making it suitable for potential applications that achieve tunability via stretching. PDMS is optically transparent at visible and near-infrared wavelengths, and is biocompatible.[53, 54] Importantly, PDMS is widely used for microfluidic chips. Recently, there has been growing interest in the incorporation of optical elements into microfluidic chips[55-59], due to the possibility for optical sensing in a very small platform. Color filters are important optical components in optical sensing, and there have been several efforts at realizing these in PDMS. Dye-doped PDMS has been used as a long pass filter for fluorescent detection in a microfluidic channel.[60] Structural color has been realized in PDMS by self-assembled colloidal photonic crystals.[61, 62] The realization of multiple filter functions on a single substrate with dye-doped PDMS is challenging, however, due to the need for multiple fabrication steps and multiple dyes with appropriate properties. This task is similarly challenging with colloidal photonic crystals, as these achieve filtering via periodic effects, meaning that they cannot be scaled to arbitrarily-small footprints.

In this Chapter, we demonstrate that embedding vertical silicon nanowires in PDMS presents a means for adding color with several favorable attributes. Multiple colors can be implemented in a single substrate, all using the same material (silicon), by appropriate choice of nanowire radius, which is readily achieved in the lithography step. As the color effect arises at the level of the single nanowire, the patterning of color with high resolution is possible. Incorporation of vertical silicon nanowires into PDMS devices also opens up other interesting possibilities for optical sensing in microfluidic chips, e.g. silicon nanopillar-based

field-enhanced surface spectroscopy.[63] The process by which the etched nanowires are transferred from the silicon substrate to the PDMS is of key importance. Several previous works have demonstrated the transfer of vertical silicon micro- and nanowires to PDMS. Vertical silicon wire arrays were transferred into PDMS which was then removed from the substrate using a razor blade [64], but these were grown microwires rather than etched nanowires. In another method, the occurrence of horizontal cracks in silicon nanowires was used advantageously in the transfer process, enabling them to be broken from the substrate more easily.[65] This method is limited, however, to silicon nanowires made by metal-assisted etching. Shear forces have been used for transferring nano-and microwires. [66] The method intentionally leaves a gap between the silicon substrate and the medium to which the wires are transferred to facilitate the nanowires being broken from the substrate by shear force. However, controlling the gap is not easy, and the method was demonstrated for relatively large and long structures. In summary, the techniques mentioned above are not feasible for relatively small nanowires suitable for color filtering that are produced by top-down anisotropic dry etching, which have diameters of ~100 nm, are 1-2 μm tall. Here, we report a simple technique for transferring etched vertical nanowires into the PDMS. We demonstrate that multiple colors can be added to a sheet of PDMS using embedded arrays of silicon nanowires.

2.1 Method for transferring vertical silicon nanowires into PDMS

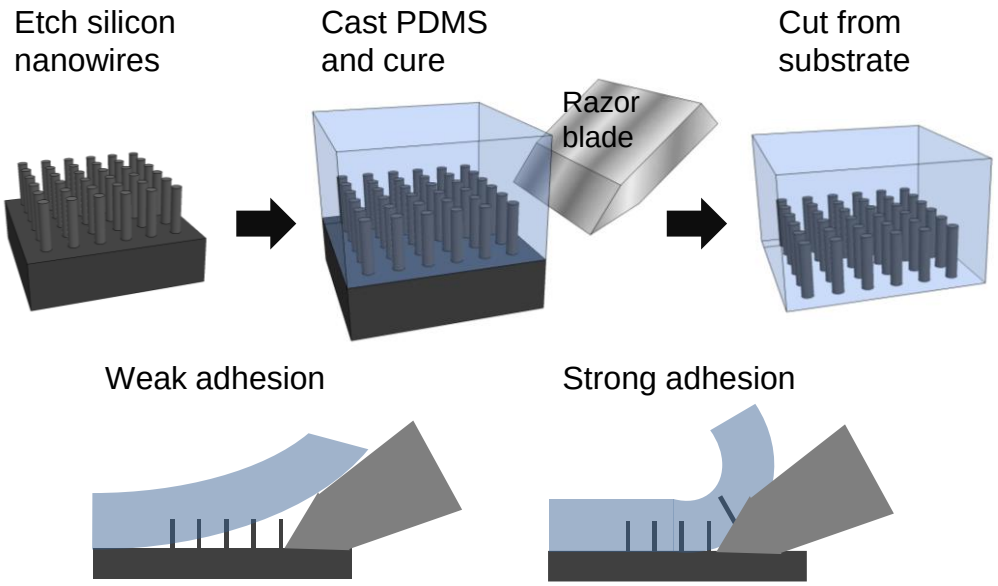

Figure 2.1 Method for transferring vertical silicon nanowires into PDMS.

The fabrication method for the PDMS-embedded vertical silicon nanowire array is shown as Figure 2.1. First, we fabricate silicon nanowires by dry etching.[48] Polymethylmethacrylate (PMMA) resist is spin coated onto the silicon wafer. Electron-beam lithography (Elionix ELS-7000), aluminum evaporation and lift-off are used to produce an etch mask that comprises aluminum disks. The wafer is then dry etched using inductively coupled plasma reactive ion etching (ICP-RIE, STS technologies) with 60 / 160 sccm of SF_6 / C_4F_8 gases for the etching and surface passivation. The etching speed was 60 nm per minute.

The fabricated nanowires are 1.5 μm tall, including the aluminum disks (0.04 μm thick) on top, and are on a square array with a pitch of 1 μm. A scanning electron microscopy (SEM) image of fabricated nanowires with radii of 65 nm is shown as Figure 2.2(left). We next spin coat PDMS at 1000 rpm for 60 seconds onto the wafer. A mixture with the PDMS base and curing agent in a ratio of 5:1 is used. The film is cured at 230 °C on a hotplate for one hour.

The PDMS film thickness is about 50 μm. The cured PDMS film is removed by scraping it from the substrate with a razor blade, using the method of Reference [64]. In that work, however, the wires were much larger (~100 μm tall, ~1.5-~2 μm diameter), and made by vapor-liquid-solid (VLS) growth. We initially applied the method of Reference [64] to our etched vertical nanowires, but the yield was small. Because their adhesion to the PDMS was low, the nanowires readily escaped from the PDMS during the razor blade scraping step (Figure 2.1). It is for this reason that we cure the PDMS at 230 °C which is higher than the standard PDMS curing temperature, as this increases the adhesion between the PDMS and silicon. This results in the nanowires remaining within the PDMS film during the razor blade scraping process (Figure 2.1), and excellent yield.

An SEM image of bottom surface of the PDMS film, the side into which the nanowires are embedded, is shown as Figure 2.2 (right). It can be seen that the surface of PDMS film is not very smooth. This is because small residues of broken nanowires are left on the substrate, preventing the PDMS from being cut cleanly. The razor blade also can be damaged during the process, which also affects the roughness. The root mean square (RMS) surface roughness is about 35 nm, as measured by atomic force microscopy (AFM). That the surface is not smooth could induce light scattering, although we did not observe any detrimental effects

from this in our work. We note however the surface could be smoothened by the spin coating of an additional PDMS layer if scattering were to prove problematic. The PDMS film shrinks after the fabrication process due to its large coefficient of thermal expansion (CTE) of ~310 ppm / ℃. We cure the PDMS at 230 ℃, but use it at room temperature (20 ℃). We therefore expect that, at room temperature, the nanowire pitch will be 0.935 μm rather than 1 μm. This is reasonably consistent with the measured nanowire pitch of 0.947 μm.

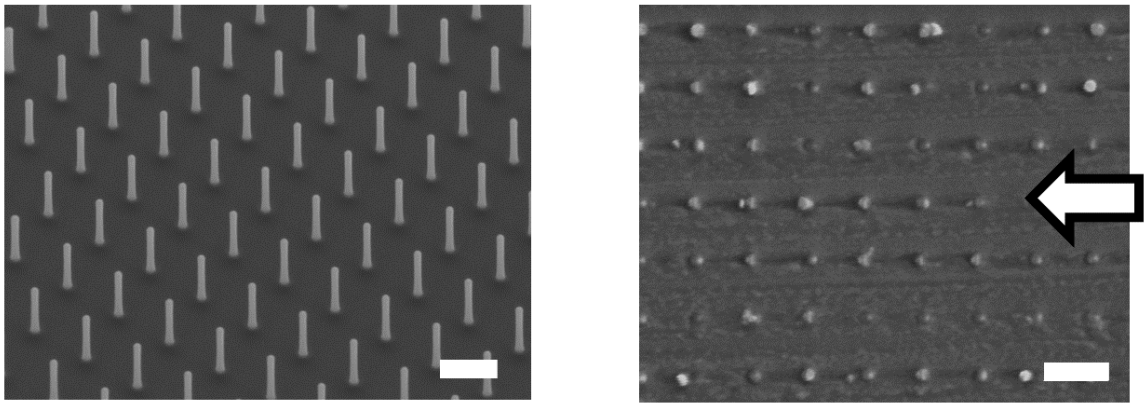

Figure 2.2 (Left) SEM images of vertical silicon nanowire array (30° tilted view). Radii of nanowires are 65 nm and heights are 1.5 μm. (Right) SEM images of bottom surface of PDMS embedded vertical silicon nanowires. Arrow indicates direction of razor blade insertion. Scale bars are 1 μm.

2.2 Optical characteristics of PDMS embedded silicon nanowires

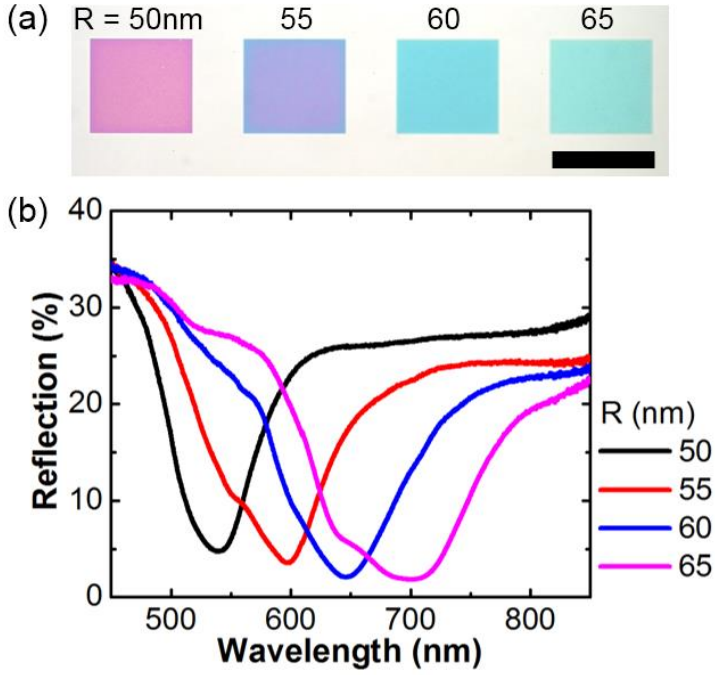

Figure 2.3 (a) Optical microscope images of etched vertical silicon nanowire arrays on silicon substrate in reflection mode. Scale bar is 100 μm. (b) Measured reflection spectra of nanowire arrays on silicon substrate.

An optical microscope image of four vertical silicon nanowire arrays on a silicon substrate before transfer is shown as Figure 2.3(a). The nanowire radii (R) range from 50 nm to 65 nm in steps of 5 nm. It should be noted that these, and all other radii quoted in this paper, are the design values in the electron beam lithography step. The nanowires are 1.5 μm

tall and have 1 μm pitch. Each array has an extent of 100 μm by 100 μm and contains 10,000 nanowires. The difference in color between the arrays is clearly seen. We use a microscope fitted with a spectrometer (Horiba Jobin-Yvon LabRAM) to measure the reflection spectrum of each array. Unpolarized white light is incident upon the sample through the objective lens (10×, NA = 0.25), with the reflected light collected by the same lens. Reflection spectra are normalized by the reflection measured from a silver mirror. As shown in Figure 2.3(b), each reflection spectrum shows a dip, whose position red shifts with increasing nanowire radius. This is due to wavelength selective coupling and spatial distribution of the nanowire's waveguide mode.[48] At short wavelengths, the mode is tightly confined to the nanowire core. The unfocused illumination does not excite it efficiently because of poor spatial overlap. At long wavelengths, the mode is expelled from the core, and is excited efficiently. The absorption within the core is small, however, due to the mode being delocalized from the nanowire. At intermediate wavelengths, both coupling and absorption are high, leading to a reflection dip. It is expected that the dip position shifts to the longer wavelength when the radius of nanowire increases because of the scale-invariance of Maxwell's equations.

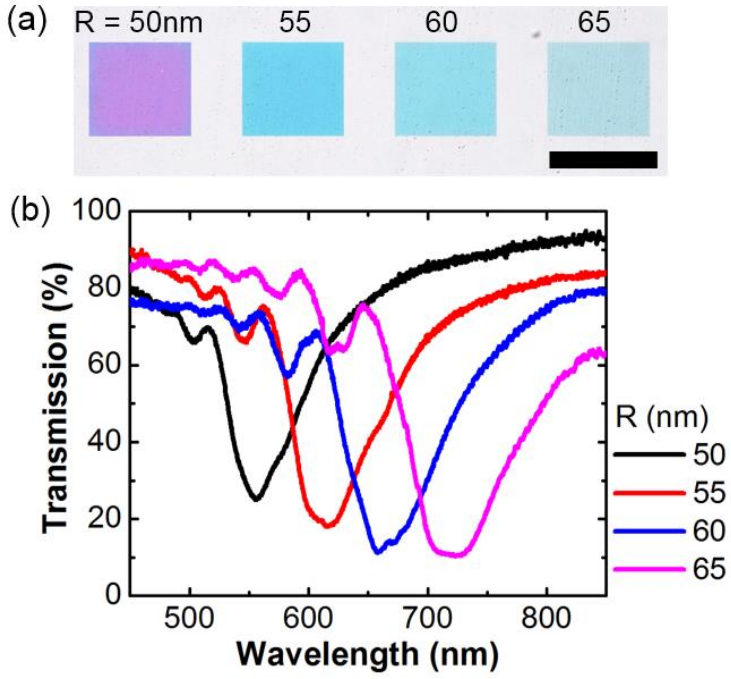

Figure 2.4 (a) Optical microscope image of PDMS embedded vertical silicon nanowire arrays in transmission mode. Scale bar is 100 μm. (b) Measured transmission spectra of PDMS embedded nanowire arrays.

A transmission mode microscope image of the vertical silicon nanowire arrays after transfer to the PDMS is shown as Figure 2.4(a). It can be seen that the goal of adding color to PDMS is achieved. Interestingly, it is evident that embedding the nanowires into PDMS modifies that color that they appear. The nanowires with radii of 50 nm, for example, appear magenta when on the silicon substrate, but purple when embedded in PDMS. A homebuilt set-up is used to measure transmission spectra of the arrays. Collimated unpolarized white light is incident upon the sample, with the transmitted light collected with a microscope objective lens (50×, NA=0.55) and into a spectrometer. The transmission spectra are normalized by spectra measured through a PDMS region not containing nanowires. The results are shown as Figure 2.4(b). Transmission dips are slightly red shifted compared to the

reflection dips. The average value of the dip shift is 15 nm. The dip shift arises because of the increase in the refractive index of the embedding medium from n=1 (air) to n=1.43 (PDMS). This effect is also seen in extinction spectra of spheres when the index of the surrounding medium increases, as predicted by Mie scattering theory.[67] We also simulate the implications of the change in nanowire pitch that results from the PDMS shrinkage. The transmission dip position is found to be almost unmodified and the transmission at the dip is reduced by 5% when pitch is decreased from 1 μm to 0.947 μm. We conclude that the change in pitch is therefore unimportant in the observed red-shift.

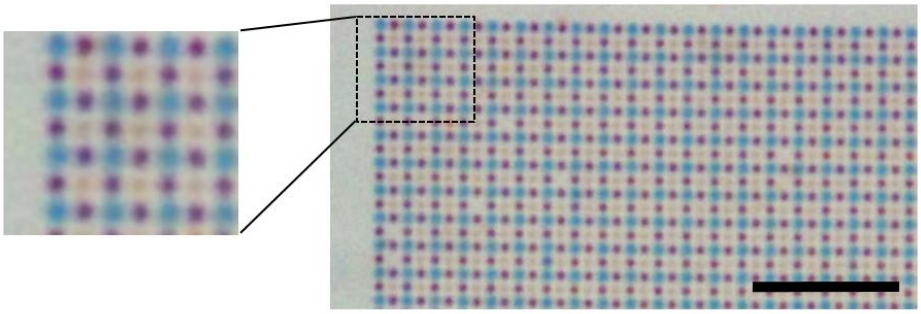

Figure 2.5 Bright-field optical microscope image of PDMS embedded nanowire arrays with different radii. Nanowires with design value radii of 50 nm, 60 nm, and 70 nm appear yellow, purple, and blue, respectively. Scale bar is 10 μm.

Our method permits the high resolution patterning of multiple colors in PDMS. Each nanowire independently shows a color that is controlled by its radius. Figure 2.5 is analogous to a Bayer pattern, but with yellow, purple and blue colors rather than red, green and blue. The nanowires are 1.98 μm tall and have a pitch of 0.95 μm pitch (in PDMS). The magnified-view inset of Figure 2.5 shows that individual nanowires exhibit color. An individual nanowire can therefore be thought of as the analog of a single ink dot in printing. The color

of the nanowires in Figure 2.5 can be seen to differ from nanowires of the same radius in Figure 2.4(a). This is because even though the lithography design value for nanowire radius is the same, the etching step differs. In addition, the nanowires of Figure 2.5 are longer than those of Figure 2.4(a) (1.98 μm rather than 1.5 μm).

2.3 Light absorption and scattering of silicon nanowires embedded in transparent medium

To quantify the roles of absorption and scattering, we simulate a single nanowire in PDMS with the finite-difference time-domain (FDTD) method. The silicon nanowire is taken as having a radius of 50 nm, a length of 1.46 μm, and the aluminum etch mask (0.04 μm thick) is included. The refractive index of background medium (PDMS) is taken to be 1.43.[68] Perfectly-matched layers are used on all boundaries, and the total-field scattered-field (TFSF) configuration is employed. The scattering, absorption, and extinction cross sections are calculated (Figure 2.6(a)). It can be seen that scattering contributes to the extinction cross section more than absorption. The dip in the transmission spectrum occurs around the extinction maximum. The simulation (Figure 2.6(a)) suggests that the majority of each transmission dip originates from scattering rather than absorption.

We next simulate arrays of nanowires, choosing the parameters to match those of the experiments. Periodic boundary conditions are applied in the x- and y-directions, where the z-direction is along the nanowire axis. The unit cell size is 947 nm x 947 nm. The nanowire

radii range from 50 nm to 65 nm in steps of 5 nm. The nanowires are again taken as being 1.46 μm long, with an additional 0.04 μm thick aluminum cap. The field monitor plane is located at 0.5 μm beyond the tops of the nanowires. To find the transmission, we take the integral of the outgoing power through the monitor plane and normalize it by the source power. We need to account, however, for the numerical aperture of the objective lens used in the experiments (NA = 0.55). To consider this, we calculate the far-field projection of the monitor plane, assuming that these far-fields are in air (n=1.0). This allows us to find the fraction of power within the collection angle of the objective lens. This is accounted for in the results of Figure 2.6(b). It can be seen that the transmission dip for the array of nanowires with radii of 50 nm occurs at the same position as the extinction peak for the single nanowire. We conclude that, like the single nanowire extinction, the transmission dip for the nanowire array is mostly due to scattering, rather than due to absorption.

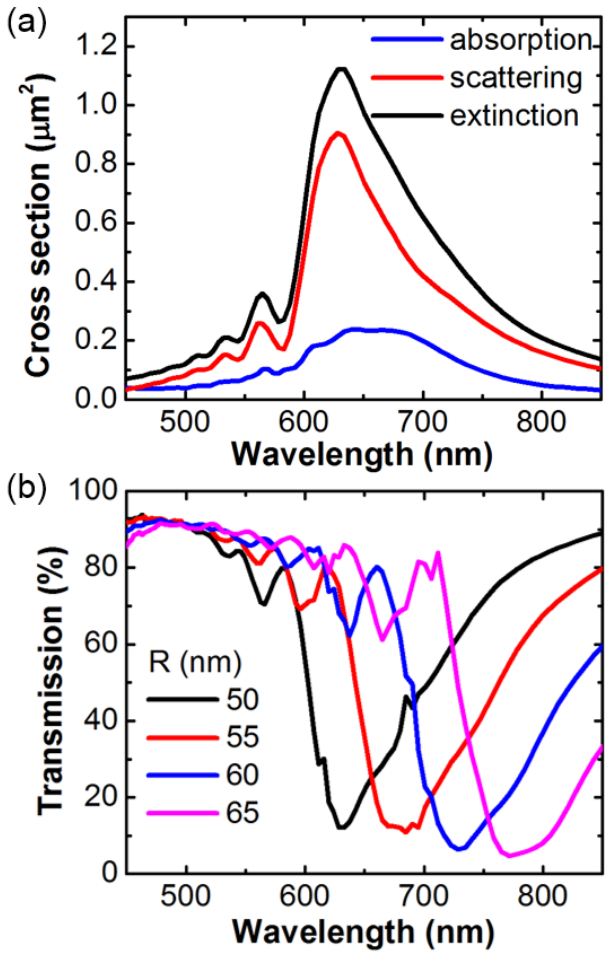

Figure 2.6 FDTD simulation results. (a) Extinction cross-section of single vertical silicon nanowire with 50 nm radius. (b) Simulated transmission spectra of vertical silicon nanowire arrays (947 nm period) with radii from 50 nm to 65 nm. Simulation models the transmitted light being collected by an objective lens with NA = 0.55.

It can be seen that the experiments (Figure 2.4(b)) and simulations (Figure 2.6(b)) are in reasonable agreement, apart from the simulations being red-shifted from the experiments in terms of dip position. We believe that this is due to the fact that simulated structures are perfect cylinders, and do not account for the tapered sidewalls present in the real structures

that result from undercutting in the etching step. Nanowires with radii of 40 nm and below collapse during the etching process due to this undercut. In addition, the top radius of etched nanowire tends to be slightly smaller than the actual mask size. In Reference [69], for example, ~5 nm notches were observed for nanowires with diameters of 100 nm. For this reason, the simulations are red-shifted with respect to the experimental results.

2.4 Conclusions

In summary, we described a method for transferring etched vertical silicon nanowire arrays into PDMS. We demonstrate that this presents a means for adding color to PDMS. We anticipate that this approach could find applications not only for color filtering, but potentially for nanowire-based sensing in lab-on-a-chip devices.

Chapter 3

Multispectral imaging with vertical silicon nanowires

In Chapter 2, we developed a method for transferring nanowires into a transparent medium (PDMS). Here, we demonstrate the use of the resultant device, i.e. a PDMS film containing the embedded nanowires, for multispectral imaging. Figure 3.1 shows a schematic representation of our approach. It was recently shown that silicon nanostructures show colors [48, 70]. We demonstrated that vertical silicon nanowires exhibit colors that span the visible and near-infrared (NIR) spectral ranges [48, 71]. The effect originates not from diffractive effects of the arrays in which the nanowires are fabricated, but from the wavelength-dependence of the spatial profile of the guided mode [48, 71]. The spectral response of each nanowire is therefore determined by its radius. This phenomenon is advantageous for the realization of multispectral filters as a single lithography step can define the optical response of all filters in the array. In our approach, an array of PDMS-embedded vertical silicon nanowires is attached to a monochrome image sensor (Figure 3.1). The unit cell of the array contains eight different spectral filters and a transparent window in its center. This configuration is analogous to the dye-based filter arrays (red/green/blue) used in color image

sensors, but with eight filter functions that span visible to NIR wavelengths, rather than three visible-wavelength filter functions. The device permits an image to be acquired from each spectral channel in a single exposure (Figure 3.1).

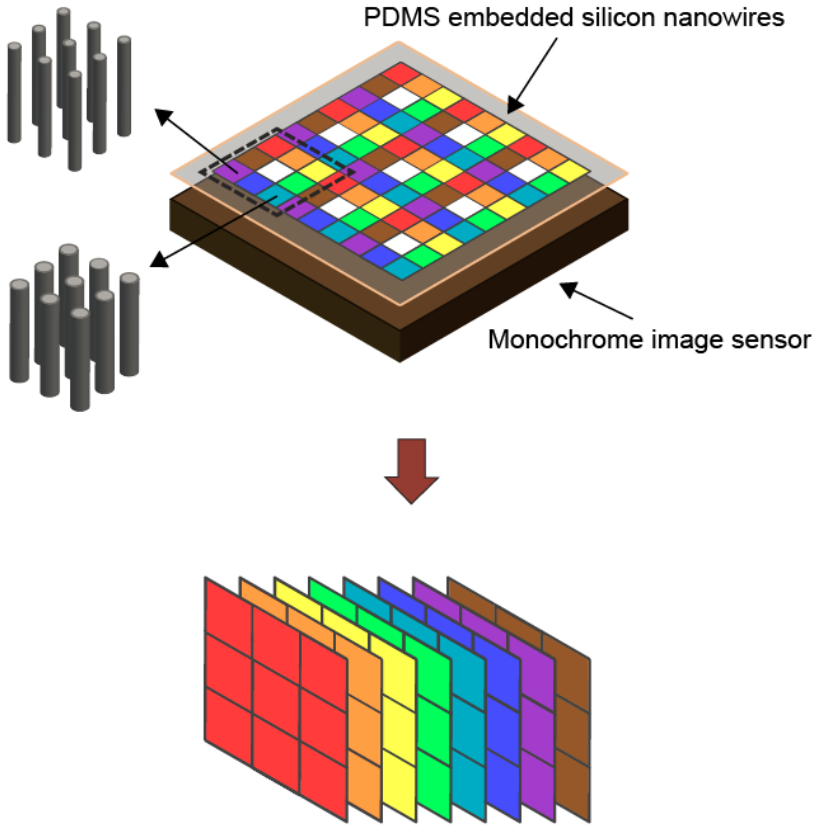

Figure 3.1 Top: multispectral filter based on vertical Si nanowires. Bottom: concept schematic of multispectral imaging system.

3.1 Fabrication of silicon nanowire based multispectral filter

The fabrication process for the multispectral filter is shown as Figure 3.2. The process [19] starts with a silicon wafer (<100> orientation) that is coated with polymethylmethacrylate (PMMA) resist. Electron-beam lithography (Elionix, ELS-7000) is performed. An aluminum etch mask (40 nm thick) is fabricated using thermal evaporation and the lift-off process. The wafer is then dry etched using inductively coupled plasma reactive ion etching (ICP-RIE) with SF_6 and C_4F_8 gases. We next spin coat PDMS (ratio of base to curing agent is 5:1) at 1000 rpm for 60 seconds onto the wafer containing the vertical silicon nanowires. The PDMS is then cured at 230 ℃ on a hotplate for an hour. The cured PDMS film is removed by cutting it from the substrate with a razor blade. The film is mounted on a monochrome CCD image sensor (ICX098BL, Sony) in a camera (DMK21AF04, Imaging Source). The resolution of image sensor is 640 by 480 pixels, and the pixel pitch is 5.6 μm. The cover glass of image sensor is removed to enable the multispectral filter to be directly attached to the surface of the image sensor. No adhesive is needed.

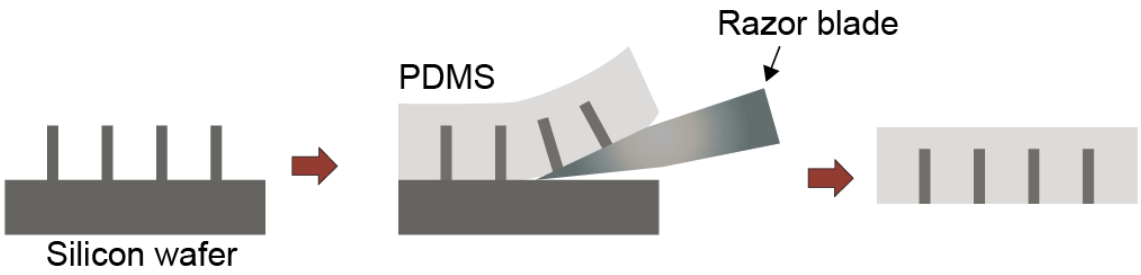

Figure 3.2 Fabrication steps for formation of multispectral filter.

It should be noted that the vapor liquid solid (VLS) method could present an alternate means for realizing this array of vertical silicon wires[43]. We furthermore note that, while we do not make use of this feature here, the transferal of micro- and nanostructures to PDMS has been shown to enable new applications, due its flexible and stretchable nature [39, 64, 72].

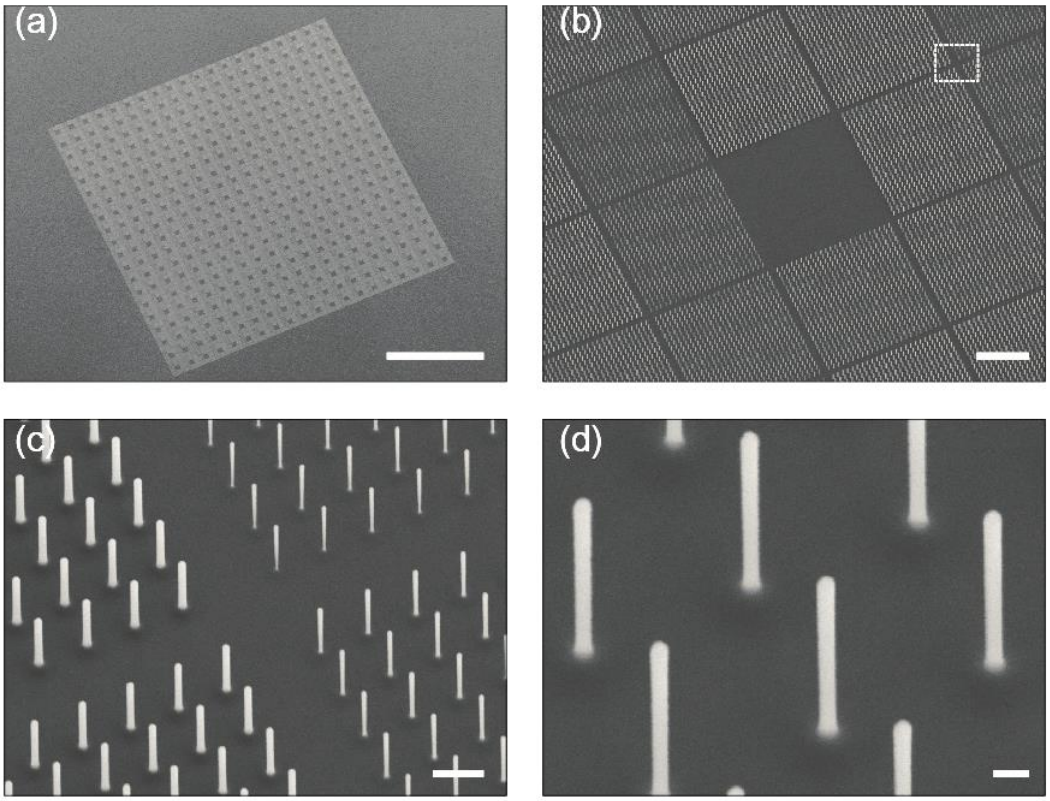

Figure 3.3 SEM image of array of etched vertical silicon nanowires (30° tilted view). (a) Array is composed of 20 × 20 unit cells. Each unit cell (75 × 75 μm) has eight different filters (each 23 × 23 μm), plus transparent region in its center. Each filter is composed of 24 × 24 nanowires and has an extent that corresponds to 4 × 4 pixels of the image sensor employed in our experiments. We intentionally choose the size of each filter to correspond to multiple image sensor pixels, rather than to a single pixel, to make it easier to align the device to the sensor chip. Scale bars for a-d are 500 μm, 10 μm, 1 μm and 200 nm. Nanowires with eight different radii (45 nm to 80 nm in 5 nm steps) are fabricated. Heights of all nanowires are 1.67 μm, and pitch is 1 μm. (c) magnified view of boxed area of panel ii. Radii of nanowires are 45 nm, 50 nm, 70 nm and 75 nm (counter clockwise from upper right corner). (d) nanowires with radii of 50 nm.

Figure 3.3 shows scanning electron microscope (SEM) images of a vertical silicon nanowire array after etching. An optical microscope image of an array of vertical silicon

nanowires on a silicon substrate is shown in Figure 3.4(a). The color difference between the nanowires with different radii is clearly seen. A transmission-mode microscope image of the vertical silicon nanowires after they are embedded in PDMS is shown as Figure 3.4(b). The silicon nanowires still show their vivid colors. It can be seen that embedding the nanowires in PDMS results in a small spectral shift to longer wavelengths.

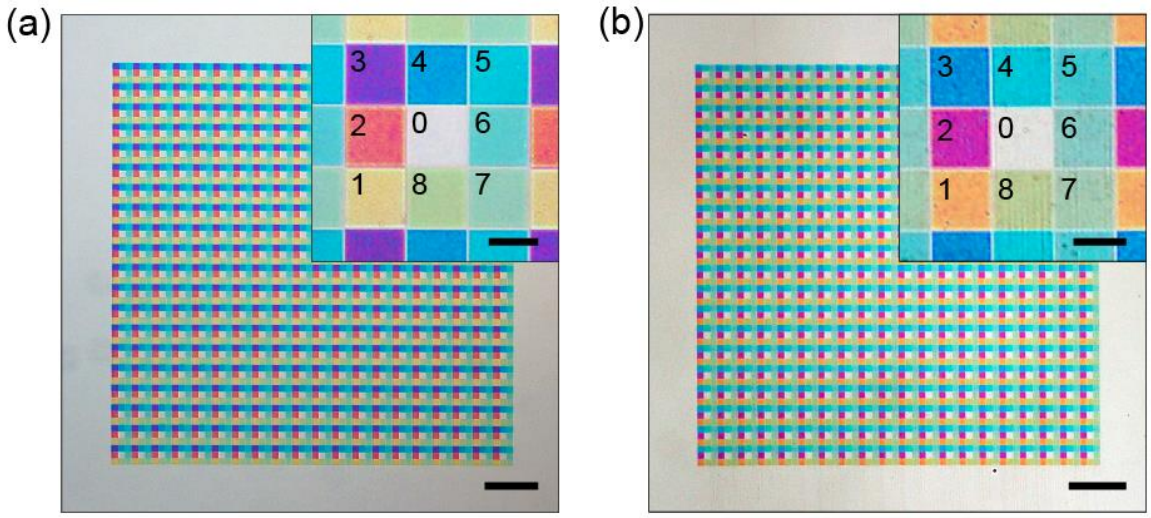

Figure 3.4 (a) Reflection-mode optical microscope image of etched vertical silicon nanowire array on silicon substrate. Scale bars are 200 μm and 20μm (inset). Inset shows magnified image of unit cell of array. Channels are numbered and contain nanowires with radii as follows. Channel 0: no nanowires, 1: 45 nm, 2: 50 nm, 3: 55 nm, 4: 60 nm, 5: 65 nm, 6: 70 nm, 7: 75 nm, 8: 80 nm. (b) Transmission-mode optical microscope image of PDMS-embedded vertical silicon nanowire array. Scale bars are 200 μm and 20 μm (inset).

3.2 Characteristics of fabricated multispectral filter

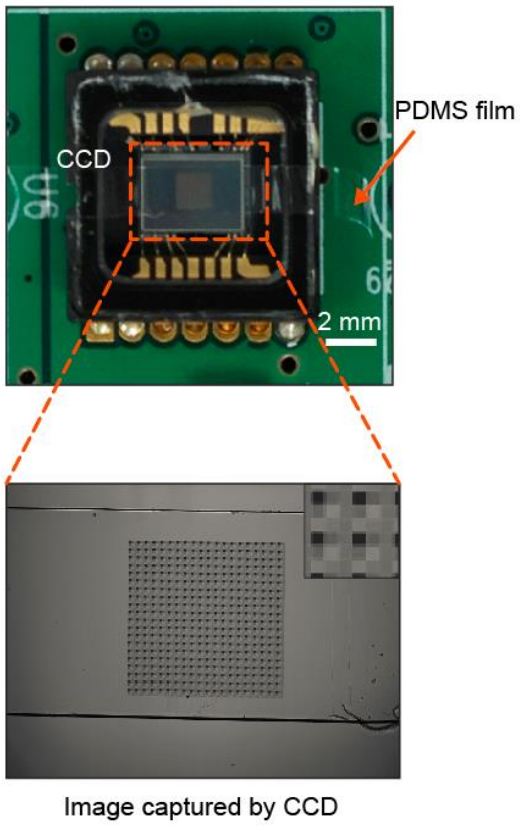

Figure 3.5 Top: photograph of multispectral filter mounted on 1/4 inch monochrome charge-coupled device (CCD) image sensor. Bottom: image captured by sensor under uniform illumination from monochromator (λ center = 600 nm). Inset: magnified image of filter area, with ~2×2 unit cells shown. Dark squares corresponds to filters containing nanowires with diameters of 55 nm nanowires, as these have transmission dip at λ≈ 600 nm.

After fabrication, the multispectral filter is mounted on the image sensor (Figure 3.5), directly on its microlens array. We measure the spectral response of our multispectral imaging system by sweeping the wavelength of the light from the monochromator from 400

nm to 1000 nm in steps of 10 nm. From the image captured by the CCD at each wavelength, the value of the pixels associated with each filter channel is recorded. This enables us to find the transmission spectra ($T(\lambda)$) of our filter channels, which are shown as Figure 3.6 along with the image sensor's relative response [73]. It can be seen that the nanowires act as subtractive color filters, suppressing specific colors (transmission dip). To find the relative response of each filter channel, we multiply the image sensor's response (black dashed line of Figure 3.6) by $1-T(\lambda)$. Multiplying it by this factor, rather than $T(\lambda)$, is convenient because the transmission dips are converted to response peaks. The results are shown as Figure 3.7. It can also be seen that the eight filters (Channels 1-8) cover visible to NIR wavelengths as desired. The filter response in a multispectral imaging experiment will depend on the nature of the application. Our approach enables a variety of filter functions to be realized. As an example, we assume that our goal is for the system to have the spectral response shown as Figure 3.8. We assign Channels VIS1-3 to have the ideal response of the CIE (1964) 10-deg color matching functions [74]. We assign Channels NIR1-5 to have Gaussian shapes with full-widths-at-half-maximum (FWHMs) of 100 nm, and center wavelengths that match those of Channels 4-8, respectively. We then use the least squares method to find the linear combination of Channels 1-8 (Figure 3.6) that achieves the most similar response to the model (goal) response of Figure 3.8. The results of this optimization process are shown as Figure 3.9. It can be seen that there are differences between the actual (Figure 3.9) and model (Figure 3.8) responses, but that these are far smaller than the un-optimized result of Figure 3.7. It should be noted that Channels VIS1-3 are reconstructed by linear combinations of Channels 1-4 to avoid them being sensitive to NIR wavelengths.

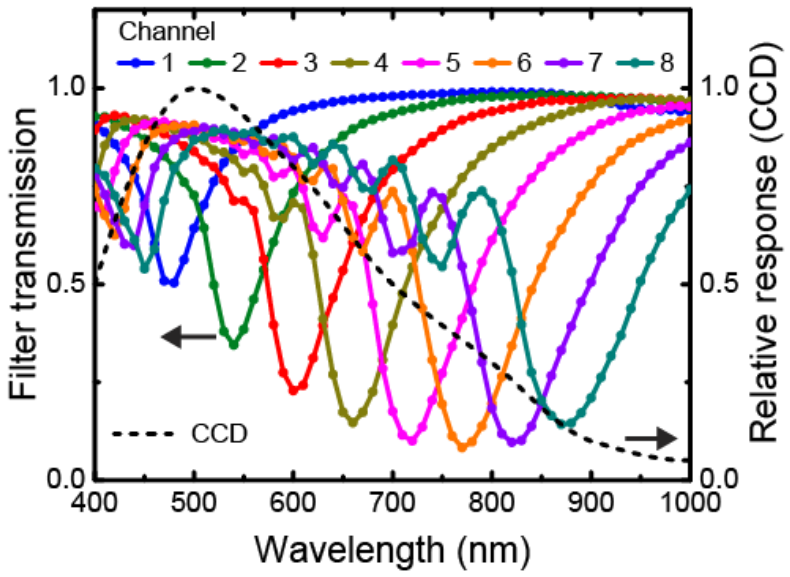

Figure 3.6 Colored lines and symbols: measured filter transmission spectra, which are found by normalizing the value of the pixels associated with each filter channel by those measured from the reference area (Channel 0, no nanowires). Black dashed line: image sensor's relative response from datasheet.

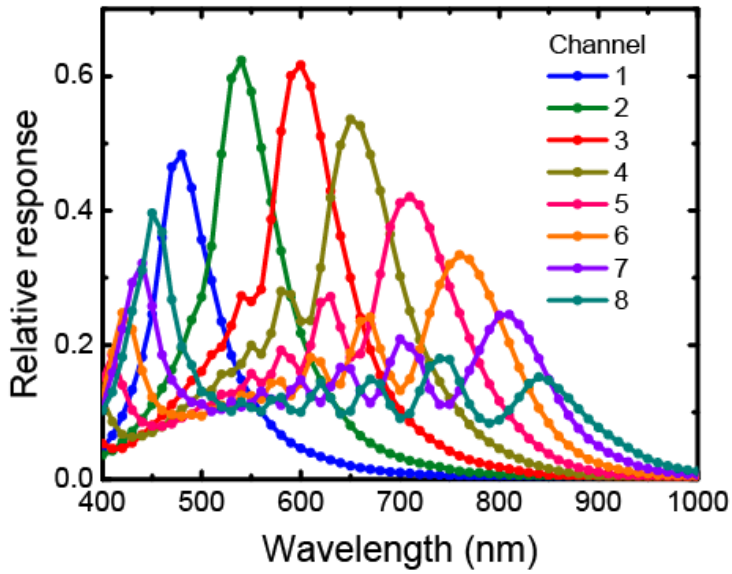

Figure 3.7 Relative response of multispectral imaging system. Channel 1-8 corresponds to the filters in Figure 3.4(b).

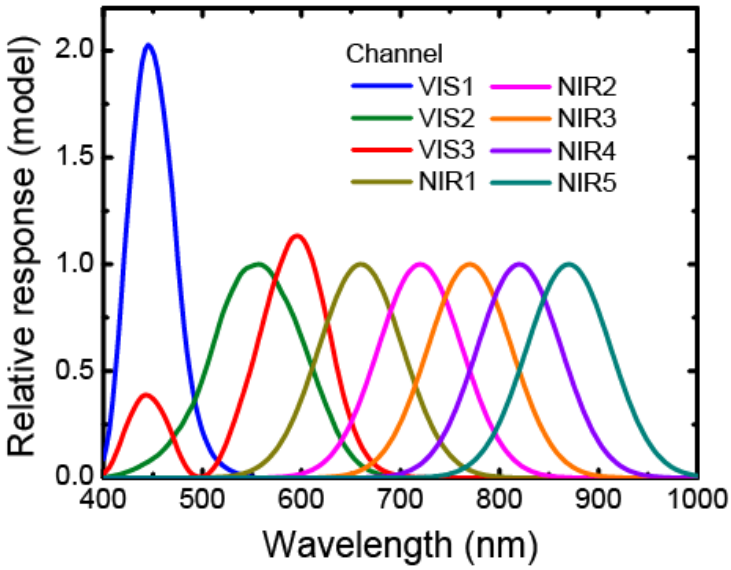

Figure 3.8 Model (goal) response of multispectral image system.

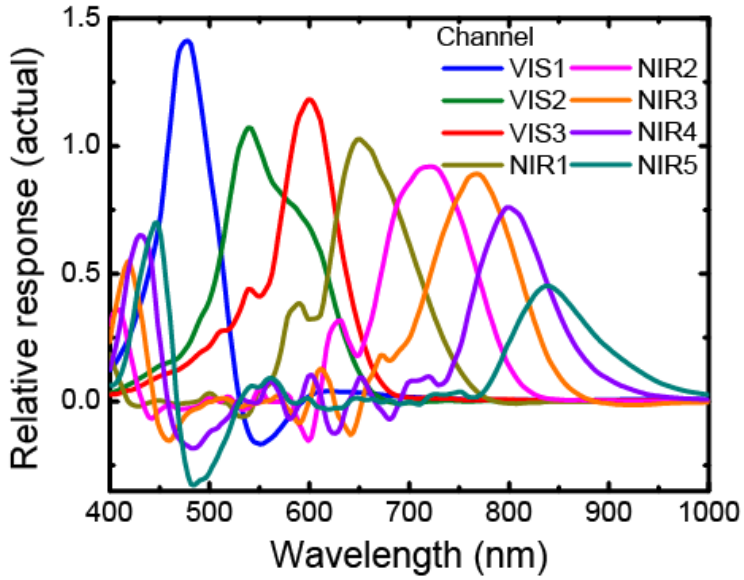

Figure 3.9 optimized via least squares method to make achieve results similar to model response (Figure 3.8).

3.3 Multispectral imaging experiment

Imaging experiments are performed using our nanowire-based multispectral system (Figure 3.10). No additional optical filters (e.g. IR blocking filter) are used. Nine images of each scene are taken, with the image sensor mechanically translated in a 3 × 3 array. This is done in order to increase the resolution and reduce the pixel calculation error due to the geometrical position mismatch between color filters (Channel 0 and Channels 1-8). We combine Channel VIS1-3 to obtain the linear standard red/green/blue (sRGB) image of Figure 3.10. We then apply color correction using the results of imaging a Macbeth ColorChecker [75] card.

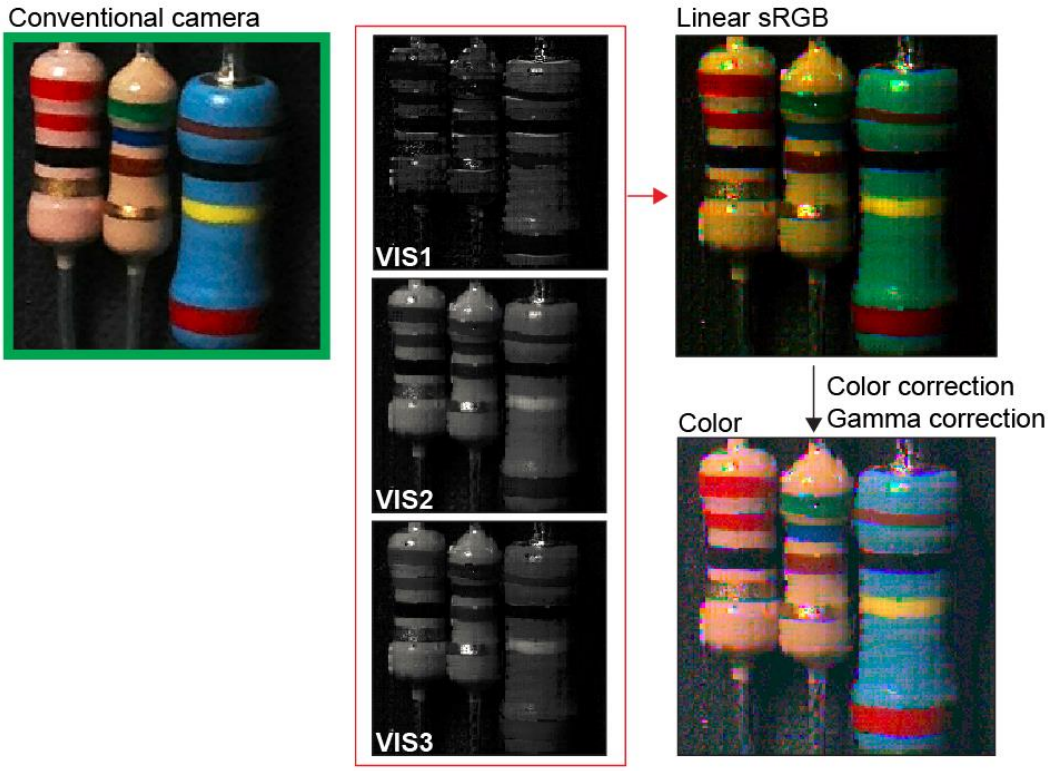

Figure 3.10 Imaging experiments. Visible color imaging of resistor. Leftmost image is taken by conventional color digital camera. Linear sRGB image generated from Channels VIS1-3. Color calibration and gamma correction are applied (gamma = 2.2) to linear sRGB image to produced corrected image.

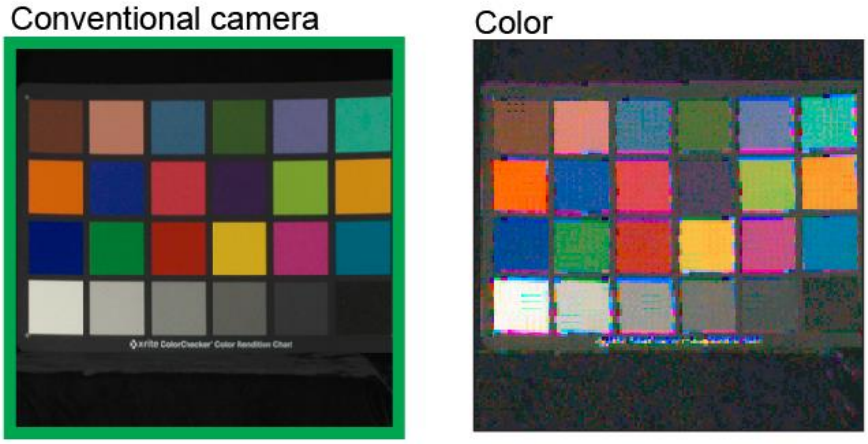

Figure 3.11 Images of Macbeth ColorChecker card by conventional camera (left) and our nanowire-based system (right).

A lens (model SMC Pentax-M 1:1.4 50 mm, Pentax) with a focal length of 50 mm and an f-number of 5.6 is used for resistor imaging experiment. A daylight compact fluorescent light bulb (CFL, model 37919, Westinghouse) is used as the light source for Figure 3.10. Our multispectral filter comprises an array of 20 × 20 unit cells, each of which contains 3 × 3 patches (eight filter functions plus transparent region in center). We sample 3 × 3 pixels in each patch. Thus, the resolution of a single-exposure image is 60 × 60 pixels. After the mechanical scanning of the camera is carried out (3 × 3), the image resolution becomes 180 × 180 pixels. Every acquired image uses eight frames averaging for noise reduction. The visible color reference image is taken by a commercial camera (8 megapixel camera of iPhone 4S, Apple). For visible color imaging, first we convert the CIE XYZ tristimulus values (Channel VIS3, VIS2 and VIS1) into the linear sRGB space (D65 illumination). This linear sRGB image is multiplied by a color correction matrix. Gamma correction of 1/2.2 is then applied. The color correction matrix is found by imaging the Macbeth ColorChecker card (ColorChecker Classic, X-Rite) and finding the linear sRGB values of the 24 color patches of the acquired image. The matrix that transforms these to the desired linear sRGB values with minimum error is then found. The resultant color image produced by our nanowire-based imaging system can be seen to be very similar to that produced by a conventional camera. It can be seen that the resistor color codes are vivid. Figure 3.11 also shows images of the Macbeth ColorChecker card obtained by our nanowire-based imaging system. The measured RMS color difference ΔE*ab of the 24 color patches is 16.3 [74, 76].

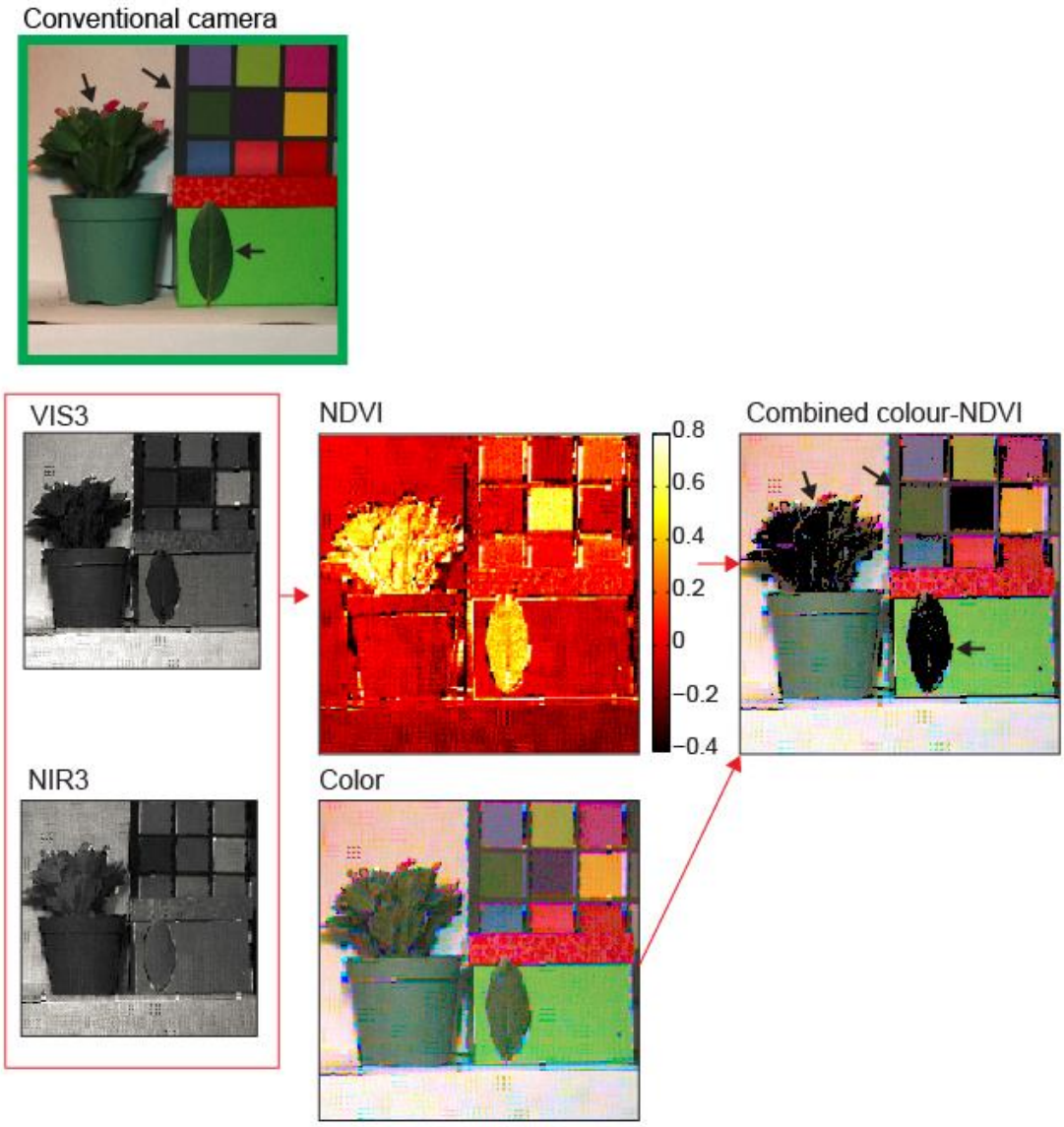

Figure 3.12 NDVI imaging of green leaves. Black arrows indicate regions (leaves and square from Macbeth ColorChecker) with similar dark green colors. The leaves and green square appear very similar in color images, but can be readily distinguished in NDVI image. Rightmost image is combined color-NDVI image, in which black shading is applied to regions whose NDVI index exceeds 0.3. Note that, due to its material properties, the violet color patch also has a high NDVI index.

Our multispectral system has five NIR channels and can be used for NIR imaging applications. As a proof-of-concept, we present a normalized difference vegetation index (NDVI) image as Figure 3.12. NDVI images are used for mapping vegetation, and represent the ratio between visible and NIR channels [77]. Vegetation areas exhibit high NDVI values because their NIR reflectance is high and their visible-wavelength reflectance is low (due to high absorption)[77]. To demonstrate our NDVI capability, we image a scene containing a plant, a single leaf and the Macbeth ColorChecker card. A lens (model M0814-MP2, Computar) with a focal length of 8 mm and an f-number of 5.6 is used for the NDVI experiments. The CFL (model 37919, Westinghouse) and an incandescent lamp (power: 40 W, GE) are used as light sources for the NDVI imaging. The leaves have dark green colors that are similar to one of the patches of the Macbeth ColorChecker card. In producing the NDVI image, we take Channel VIS3 as the visible channel and Channel NIR3 as the NIR channel. From the NVDI image of Figure 3.12, it is can be seen that the leaves have higher NDVI values than the dark green color patch. This confirms that ability of our nanowire-based multispectral imaging system to identify vegetation.

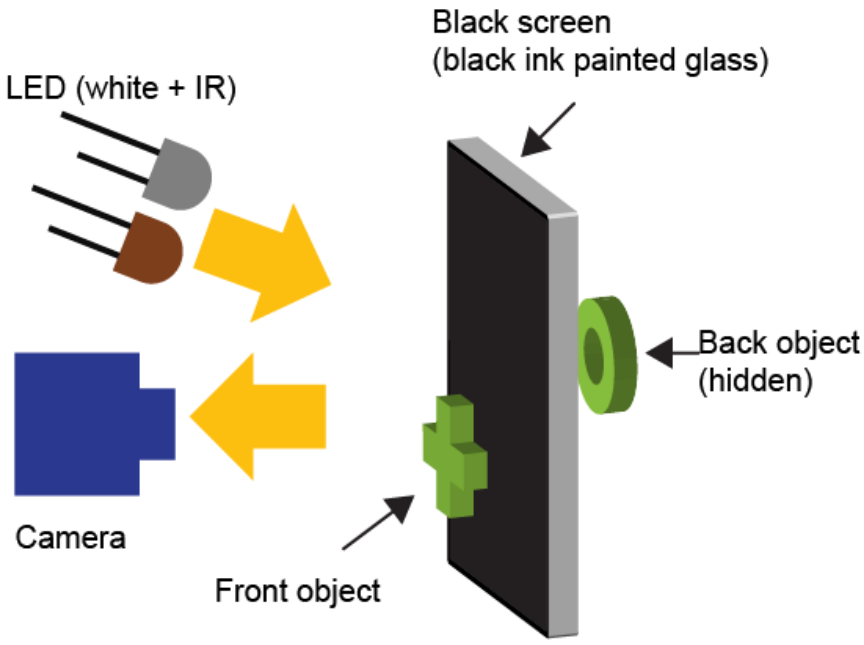

Figure 3.13 Demonstration of NIR imaging through object that is opaque at visible wavelengths (black ink on glass). Both white and IR light emitting diodes (LEDs) are used as light sources.

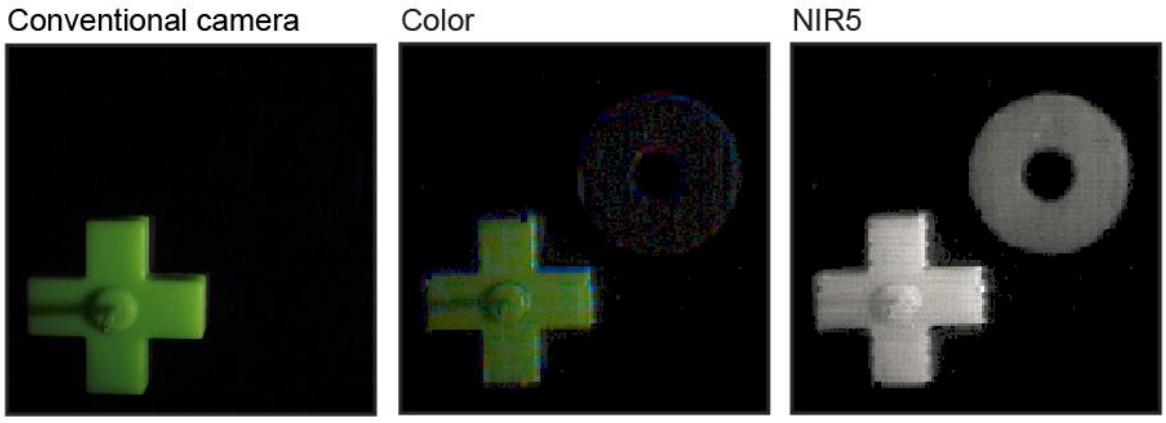

Figure 3.14 In color images obtained by conventional camera and our nanowire-based system, object in front of screen is visible, while object behind screen is very difficult to observe. Both front and back objects are observed in NIR image (Channel NIR5, gamma corrected with gamma = 2.2).

We next demonstrate that our nanowire-based system enables imaging to be carried out through objects that are impervious at visible wavelengths. We make use the fact that a number of dyes are transparent at NIR wavelengths[78]. A glass plate painted with a black permanent marker is used as a screen that is opaque to visible light (Figure 3.13). A cross-shaped green object is located in front of the black screen, while a donut-shaped green object is located behind it. We uses both a white LED (model 276-320, RadioShack) and an IR LED (model 276-143, λ_{center} = 950 nm, RadioShack) as light sources. The results are shown as Figure 3.14. In the visible-wavelength images collected by a conventional camera and by our nanowire-based system, the object in front of the screen is visible, while the back object is observed only with difficulty. The NIR channel (NIR5) image collected by our nanowire-based system, however, shows both front and back objects.

3.4 Conclusion

Through the creation of filter based on vertical silicon nanowires, we have demonstrated multispectral imaging from the visible to NIR regions. The described method is very practical from a manufacturing standpoint because all filter functions are defined at the same time through a single lithography step, that then only needs to be combined with two simple additional steps (etching and embedding in PDMS) to produce a fully-functional device. We anticipate that this work will facilitate multispectral imaging systems that are more compact and lower in cost than current approaches.

Chapter 4

Filter-free image sensor pixels comprising silicon nanowires with selective color absorption

In this Chapter, we make use of the unique optical properties of semiconductor nanowires, namely that their spectral absorption can be engineered, for filter-free color imaging. A key motivating factor for the field of nanotechnology is that the properties of materials can be dramatically altered when they take the form of one-dimensional nanostructures. Semiconductor nanowires are especially of interest due to their unique optical and electrical characteristics.[37, 39, 41, 50] It has been demonstrated that horizontal germanium [46, 47] and silicon[79] nanowires show light absorption and photocurrent spectra that vary with nanowire radius. In addition, wavelength selective photodetectors have been demonstrated using self-aligned silicon fins in metallic slits.[80] To the best of our knowledge, however, no color or multispectral imaging experiments have been performed that make use of this, probably because of difficulty in assembling reasonable numbers of the vapor liquid solid (VLS) grown nanowires into devices and in forming the necessary p-

i-n junctions. These spatial distributions depend on the nanowire radius.[48, 49, 81] The nanowires are in arrays, but the effect does not originate from diffractive effects, but can be understood at the level of the individual nanowire. An important advantage of this approach is that a single lithography step defines the nanowire radii, and therefore their optical responses. We have previously shown that, when embedded into a transparent film, the nanowires can be used as passive color filters for multi-spectral imaging.[71, 82] Here, we demonstrate a conceptually-different mode of operation. Rather than acting as passive filters, the nanowires incorporate photodetectors, meaning that absorbed photons are converted to photocurrent. This permits color imaging.

4.1 Fabrication of vertical silicon nanowires photodetector

The concept of our vertical silicon nanowire-based p-i-n photodetector is illustrated schematically as Figure 4.1. Photodetectors based on vertical silicon nanowires have been previously reported, and shown to exhibit high phototransistive gain and infra-red response.[83, 84] The wavelength-selective absorption properties of nanowires have not been used for color imaging however, to the best of our knowledge.

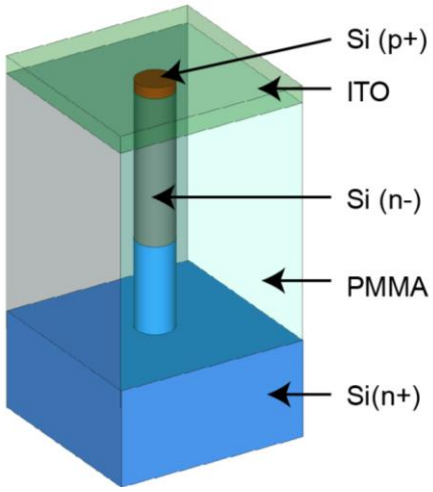

Figure 4.1 Concept schematic of p-i-n photodetectors based on vertical silicon nanowires.

Key steps of our fabrication process are shown in Figure 4.2. We start with a silicon epitaxial wafer (substrate: n+, epitaxial layer: n-). A silicon epitaxial wafer with n-type substrate (n+, <100> orientation, R = 0.01 Ω•cm) and n-type epitaxial layer (n-, R > 100 Ω•cm, ~ 2 μm thick) is prepared. We dope the top of the epitaxial layer to p+ using boron diffusion from a spin-on dopant (PBF2.0A, Filmtronics) in a furnace (Lindberg Blue/M, Thermo Electron Corporation, O2: 100 sccm, N2: 300 sccm, 950 ℃ for 20 min). After removing the resulting thermal oxide (BOE 1:5 for 20 min), polymethylmethacrylate (PMMA495-A2 and PMMA950-A2, Microchem) resists are spin-coated on the wafer and e-beam lithography (ELS-7000, Elionix) is performed. The wafer is developed. An aluminum etch mask (Al, 40 nm) is fabricated using thermal evaporation and the lift-off process. The wafer is then dry etched using inductively coupled plasma reactive ion etching (ICP-RIE) with SF_6 / C_4F_8 gases with flow rates of 60 sccm / 160 sccm respectively. The aluminum masks are removed using an aluminum etchant (Type-A, Transene). We then spin coat and

cure PMMA (PMMA495-A8, Microchem) onto the wafer containing the vertical silicon nanowires. This is used as the spacer to form a top electrical contact. The PMMA spacer is dry etched using an oxygen plasma (SCE106, Anatech LTD) to expose the tops of the nanowires. We then sputter (Orion3, AJA) indium tin oxide (ITO, 60 nm thick) to make a transparent electrical contact to the tops of the nanowires. A scriber (LSD-100 Scriber/Cleaver, Loomis Industries) is used to cut the ITO layer to ensure that the nanowire arrays are electrically separated. Finally, the sample is mounted on a printed circuit board (PCB) and electrical connections are established between each of the segments of the ITO layer and separate PCB pads using gold wires and silver epoxy. The n+ substrate is also connected to the PCB ground.

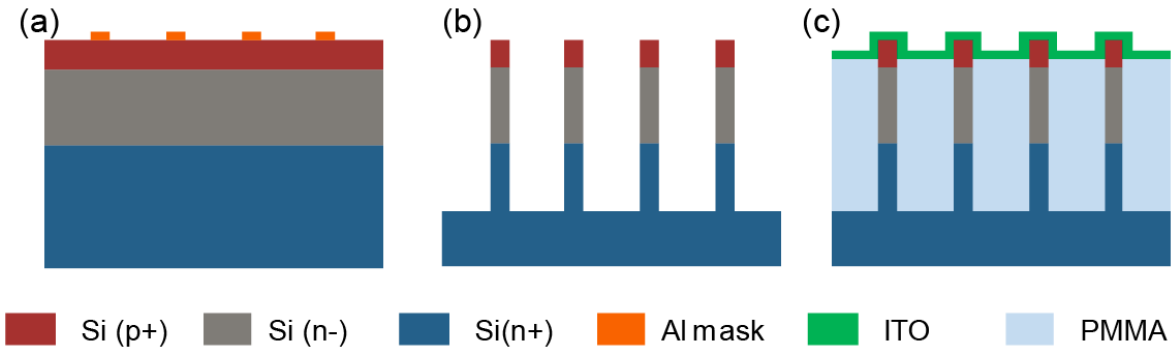

Figure 4.2 Fabrication steps. (a) Epitaxially-grown n+/n- wafer doped with p+ on top. Aluminum (Al) etch mask is fabricated using e-beam lithography, evaporation and lift-off. (b) Vertical silicon nanowires are dry etched. (c) PMMA is spun cast and cured. Top of PMMA is dry etched to expose nanowires. ITO is sputtered to make a transparent electrical contact to nanowires.

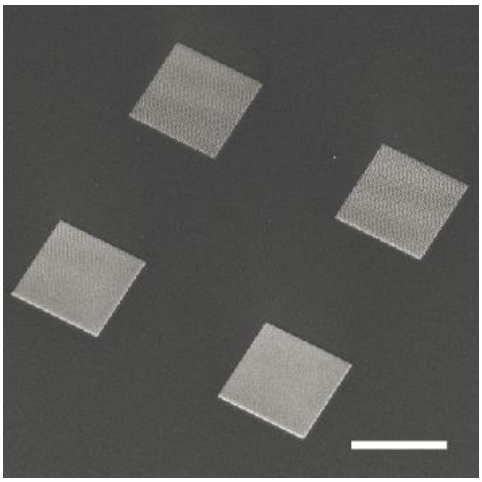

Figure 4.3 SEM image of nanowires in step ii of Figure 4.2 (b). (30° tilted view). Each array contains 100 × 100 nanowires. Arrays contain nanowires with radii of 80 nm, 100 nm, 140 nm and 120 nm (clockwise from upper left corner). Heights of all nanowires are 2.7 μm, and pitch is 1 μm. Scale bar is 100 μm.

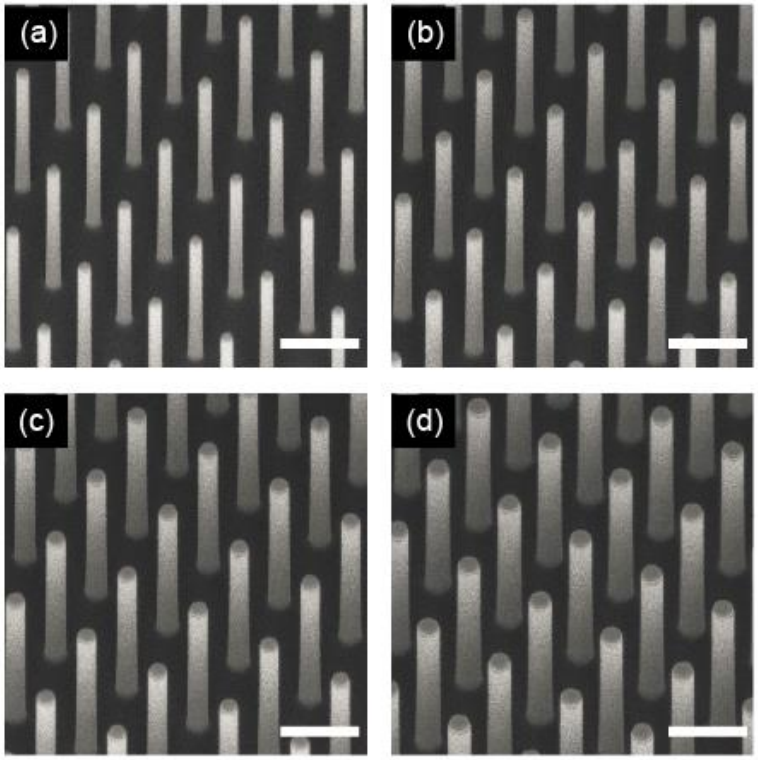

Figure 4.4 Magnified view of nanowires. (a-d) nanowires with radii of 80 nm/ 100 nm/ 120 nm/ 140 nm. Scale bars are 1 μm.

We fabricate arrays containing nanowires with radii of 80 nm, 100 nm, 120 nm and 140 nm. It should be noted that these, and all other radii quoted in this Chapter, are the design values in the electron beam lithography step. All nanowires are 2.7 μm tall with a pitch of 1 μm. We choose these parameters for fabrication considerations. We can etch nanowires with this height without them collapsing. The period is chosen to guarantee the uniform filling of polymethylmethacrylate (PMMA) between the nanowires in the later spacer fabrication step. Each nanowire array comprises 100 × 100 vertical nanowires, and has an extent of 100 μm × 100 μm. The nanowires have vertical p-i-n junctions, consisting of p+ / n- / n+ layers with thicknesses of about 200 nm / 1500 nm / 1000 nm, respectively. Figure 4.3 and Figure 4.4 show scanning electron microscope (SEM) images of arrays of etched vertical silicon nanowires. These images are obtained from a dummy sample fabricated using the same process as the actual device used in imaging experiments. This is done to prevent possible damage of the actual device from electron beam radiation and to minimize contamination.[85]

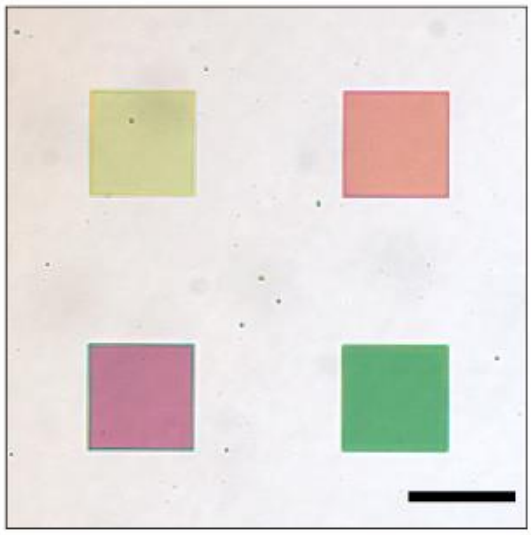

Figure 4.5 Reflection-mode optical microscope images of etched nanowires arrays. Scale bar is 100 μm. Radii of nanowires are 80 nm, 100 nm, 140 nm and 120 nm (clockwise from upper left corner).

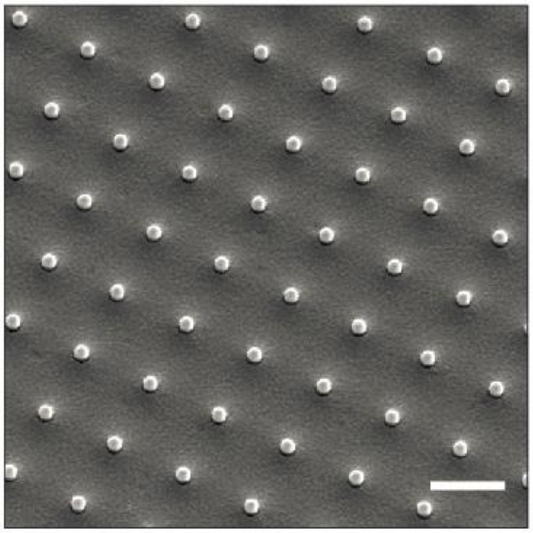

Figure 4.6 SEM image of nanowires embedded in PMMA and covered by ITO. Scale bar is 1 μm.

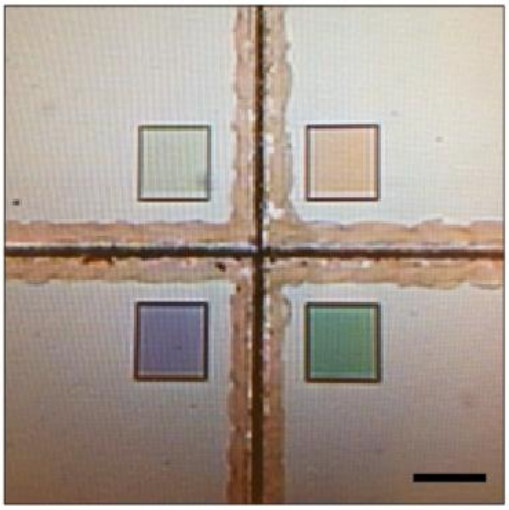

Figure 4.7 Device after scribing has been performed on ITO layer to electrically separate nanowire arrays. Scale bar is 100 μm.

An optical microscope image of an array of etched vertical silicon nanowires on a silicon substrate is shown in Figure 4.5. The color difference between the nanowires with different radii is clearly seen. Figure 4.6 shows an SEM image of the silicon nanowires (radii: 80 nm) after the PMMA is etched and ITO is sputtered. It is evident that the tops of the nanowires are exposed as desired, meaning that electrical contact can be established. To electrically separate the nanowire arrays, the ITO layer is next scribed (Figure 4.7). Finally, the device is mounted on a PCB and electrical contact is made by gold bond wires and silver paste (Figure 4.8).

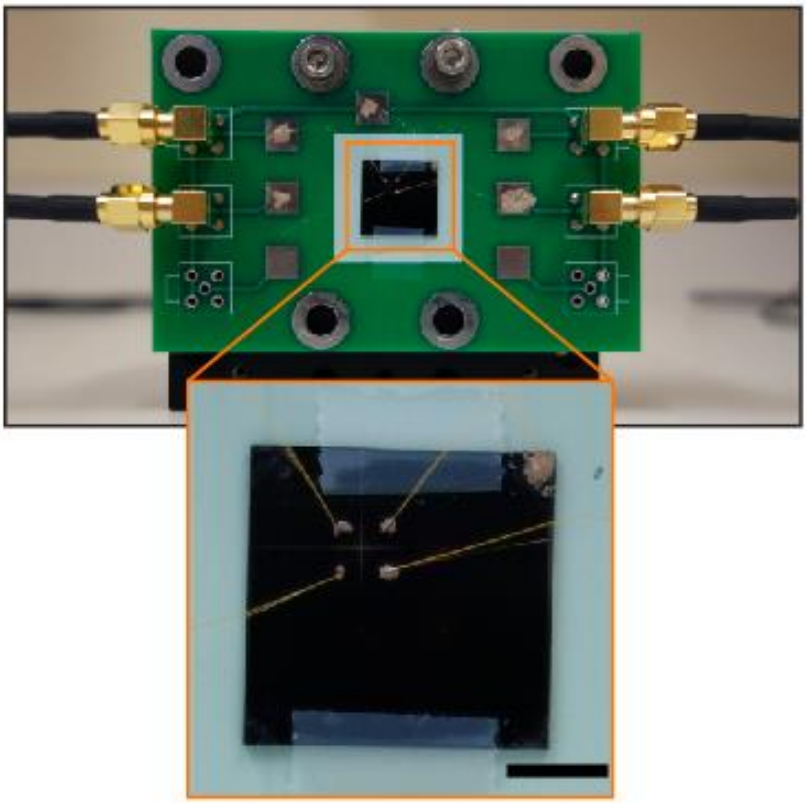

Figure 4.8 Photograph of fabricated device mounted on PCB. Inset shows magnified image of device. Scale bar is 5 mm. Electrical connection established using gold wires and silver epoxy.

4.2 Electrical measurement and optical simulation

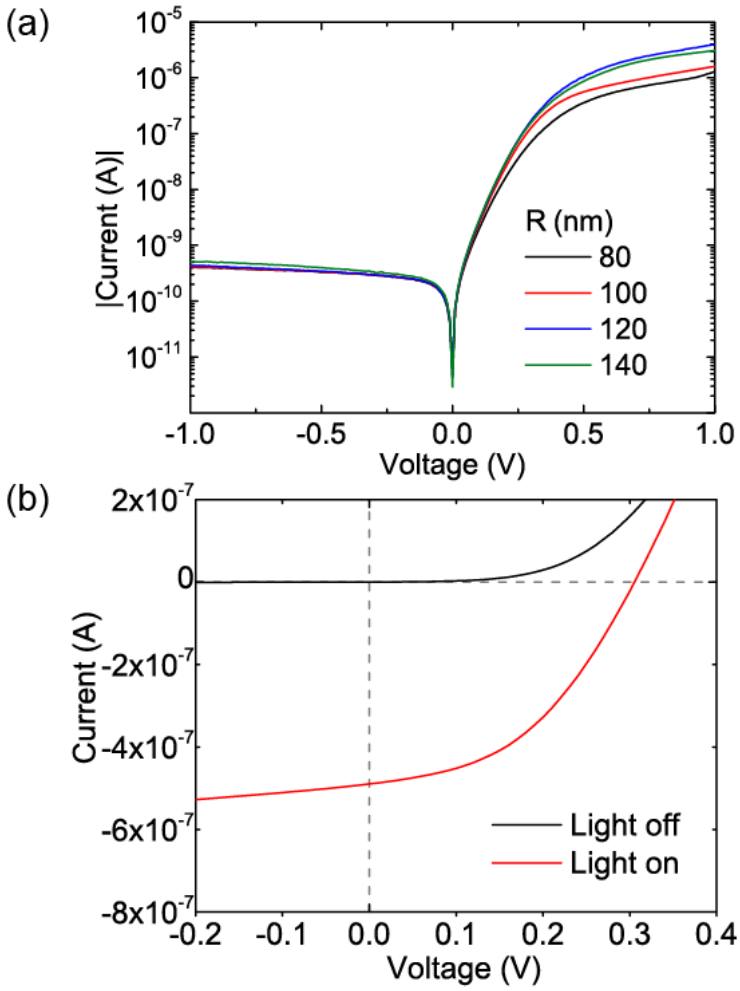

Figure 4.9 Electrical measurement and optical simulation of fabricated device. (a) Dark state I-V curve of fabricated device (log scale) (b) I-V measured in dark state, and under illumination of 270 mW / cm^2 at a wavelength at 633 nm. Nanowires have radii of 140 nm.

The current-voltage (I-V) characteristics measured from un-illuminated (dark state) fabricated nanowire arrays with four different radii are shown as Figure 4.9(a). I-V characteristic of an array of nanowires with radii of 140 nm under dark and illuminated

conditions is shown in Figure 4.9(b). A sourcemeter (2400, Keithley) is used for the I-V measurements. The device is connected to the source meter and the voltage is swept from -1 V to 1 V in 0.05 V steps. We use a He-Ne laser (Melles Griot, λ=633 nm) for the I-V measurement performed under light illumination. Each array contains 100 × 100 nanowires, and all measurements are conducted at room temperature. The dark current measured from each array is ~300 pA at a bias of -1 V. The dark current density is therefore ~3 $\mu A / cm^2$, which is significantly higher than state-of-the-art CMOS devices (3.8 pA / cm^2).[86] We believe this comes from thermal generation due to surface states that are increased by the large surface-to-volume ratio of the nanowires and damage to the silicon crystal structure from dry etching.[87, 88] We anticipate that the dark current could be reduced by synthesizing the nanowires using alternative methods or by adding passivation layers. Alternative synthesis methods could include metal-assisted chemical etching[89] or VLS growth[43], as these frequently yield nanowires with smoother surfaces than dry etching. It has been reported that surface passivation using silicon dioxide[90] or amorphous silicon[91] reduce nanowire surface states.

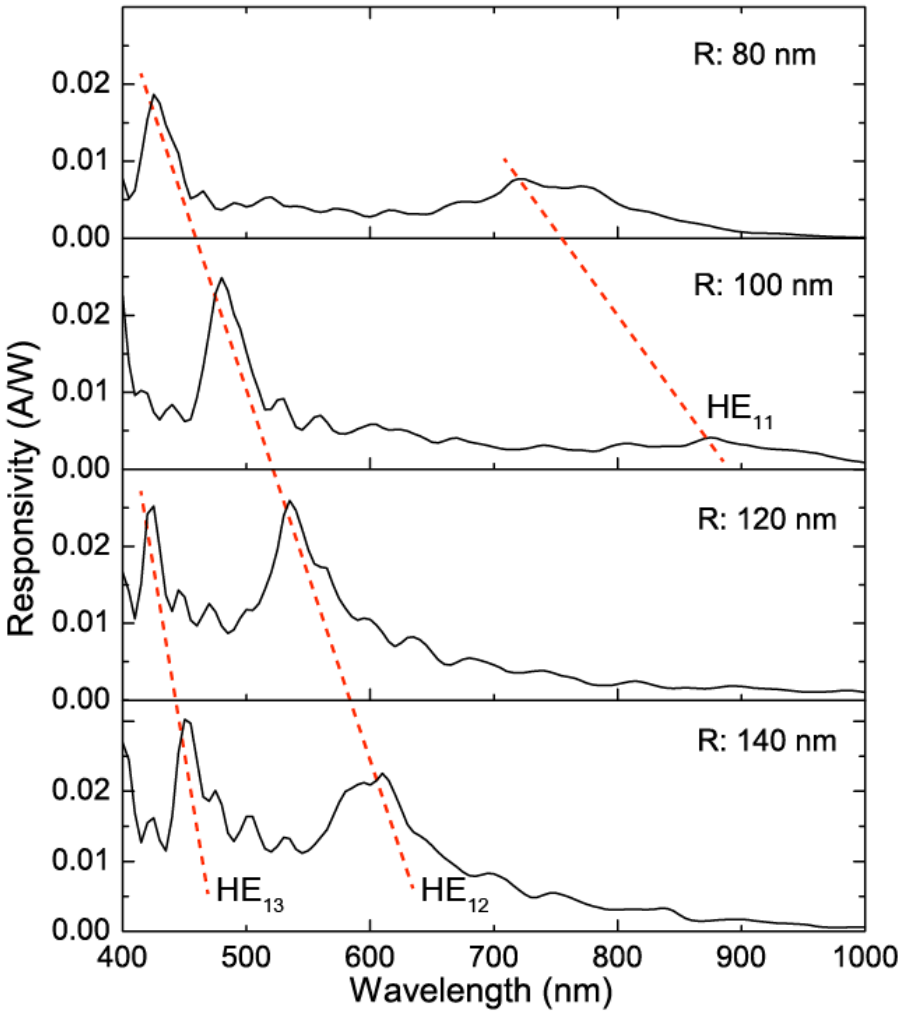

Figure 4.10 Measured responsivities of photodetectors with nanowire radii (R) of 80 nm, 100 nm, 120 nm and 140 nm.

We measure the responsivities of devices containing nanowires with radii (R) of 80 nm, 100nm, 120 nm, and 140 nm at 0 V bias. A monochromator (MS257, Oriel instruments) with a halogen lamp is used for measuring the responsivities of the silicon nanowire arrays. The

output bandwidth of monochromator is 5 nm. The light from the monochromator goes through a pinhole (200 μm diameter) and is focused onto the nanowires array using an objective lens (10×, NA 0.28, Mitutoyo). The power of light incident onto the nanowires array at the wavelength of 630 nm is 20 nW. A beam splitter is located between the pinhole and objective lens to image the sample using a CCD camera (DMK21AU04, Imaging Source). We adjust position of the sample so that spot of focused light from the monochromator is incident upon the nanowire array. The photocurrent from the nanowire array is measured by a picoammeter (6485, Keithley). The power of the light incident upon the device is measured using a reference silicon photodetector. This enables us to calculate the responsivity. The external quantum efficiency (EQE) is found using EQE = R (hf / q) (R : responsivity, h: Planck's constant, f: frequency of light, q: magnitude of electron charge). The results are presented as Figure 4.10, and demonstrate that the choice of nanowire radius strongly modifies the positions of the responsivity peaks.

The major peaks correspond to HE_{11}, HE_{12} and HE_{13} modes.[49] It should be furthermore noted that, by adding a bottom photodetector, it would be possible to convert the light that is not absorbed by the nanowires to photocurrent. This presents the exciting prospect of image sensor pixels with significantly higher photon efficiencies than current filter-based approaches as in principle all light incident on the device can be converted to photocurrent. This is pursued in Chapter 6.

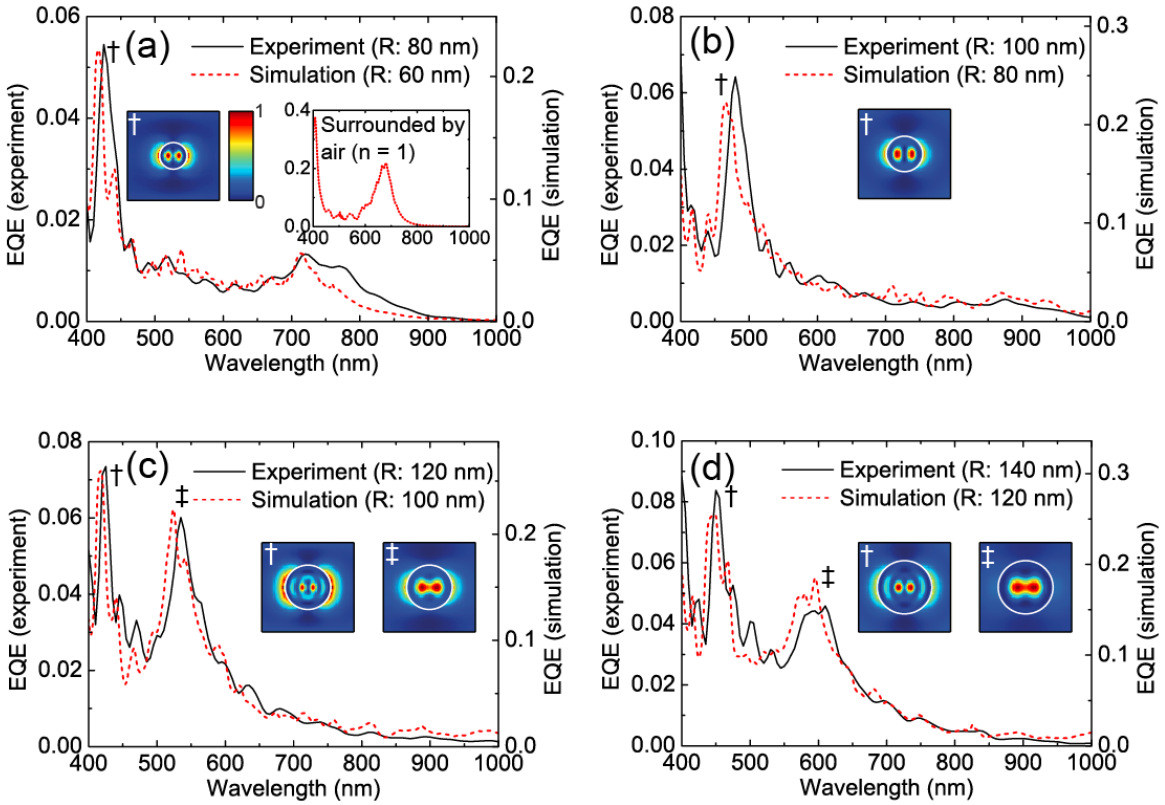

Figure 4.11 Measured and simulated external quantum efficiencies (EQEs) for nanowire devices with different radii. Insets show electric field intensity profiles (normalized) simulated at wavelengths of peaks of EQE spectra (simulations) denoted by dagger or double dagger. Profiles are horizontal slices (400 nm × 400 nm) at tops of intrinsic regions, i.e. 200 nm below nanowire top ends. White circle shows nanowire outline. Inset of (a) shows simulated EQE of nanowires (R = 60 nm) when embedded in air (n=1) rather than PMMA (n=1.495). HE_{11} mode around 700 nm is distinct when surrounding medium is air, but suppressed when embedded in PMMA.

The method furthermore has advantages over the approach to filter-free color imaging that uses the wavelength-dependent absorption length of light in silicon, as the spectral absorption properties in our case can be controlled by nanowire geometry, rather than being a fixed material property. From the responsivity data, the external quantum efficiency is found and plotted as Figure 4.11. To estimate the internal quantum efficiency, we perform

electromagnetic simulations using the finite-difference time-domain (FDTD) method. The geometries of the simulated structures are chosen to match those of the actual devices except for the nanowire radii. A nanowire is located on the silicon substrate and length of the nanowire is 2.7 μm. The nanowire radii vary from 60 nm to 120 nm in steps of 20 nm. The PMMA layer (2.5 μm thick) covers the nanowire and substrate. The refractive index of PMMA is taken to be 1.495. An ITO layer (60 nm) is on top of the PMMA layer. The ITO refractive index is taken to be 1.95. Periodic boundary conditions are applied in the x- and y-directions, where the z-direction is along the nanowire axis. The unit cell size is 1 μm × 1 μm. The illumination is taken as a normally-incident plane wave. The absorption of intrinsic region of nanowire is then calculated. Length of intrinsic region is taken to be 1.5 μm. The intrinsic region starts at 200 nm below the top of the nanowire. The electric field intensity profile of Figure 4.11 is plotted on the (horizontal) $x - y$ plane at the top of the intrinsic region.

We find that improved agreement between experiments and simulations is achieved when the simulated nanowires have radii 20 nm smaller than the design values of the actual devices. We believe that this is due to fabrication imperfections in the actual devices. The top radii of etched nanowires tend to be slightly smaller than the actual etch mask. This is consistent with previous reports of ~5 nm notches for nanowires with diameters of 100 nm.[69] In addition, the simulations assume perfect cylinders, and do not account for the tapered sidewalls present in the real structures that result from undercutting in the etching step. The simulated external quantum efficiency is taken as the ratio between the power absorbed in the intrinsic region and the incident power, meaning that the internal quantum

efficiency is assumed to be 100 %. To estimate the internal quantum efficiency of the fabricated devices, use the least squares method to find the factor that, when multiplied by the simulated external quantum efficiency, results in the best fit to the experimental data. This factor is then the internal quantum efficiency. For nanowires with radii of 80 nm / 100 nm / 120 nm / 140 nm, the measured external quantum efficiencies are in reasonable agreement with the simulated external quantum efficiencies for internal quantum efficiencies of 0.24 / 0.26 / 0.28 / 0.30. That these are not unity is likely to be mainly due to surface recombination at the etched surfaces of the nanowires. We believe that the internal quantum efficiency can be increased by passivating nanowires using the methods mentioned above. In addition, the external quantum efficiency can be enhanced by optimizing the height and period of the nanowire arrays.

Simulations indicate that light absorption increases as period decreases or height increases. Figure 4.12 shows the effect of nanowire period on the absorption spectra. The spectral peak increases in height as the period decreases. This shows that amount of light absorbed strongly depends on the nanowire period. The simulated external quantum efficiency lineshapes are largely unchanged as the period is varied, for periods greater than 0.6 μm. When the nanowires are sufficiently close (period = 400 nm), however, the coupling between the waveguide modes of the nanowires is strong enough to induce absorption peak broadening. Figure 4.13 shows the effect of intrinsic region length on the absorption spectra. The absorption increases as the length of intrinsic region increases while the spectral lineshapes are largely unchanged. This implies that the amount of light absorbed in the nanowires strongly depends on their height.

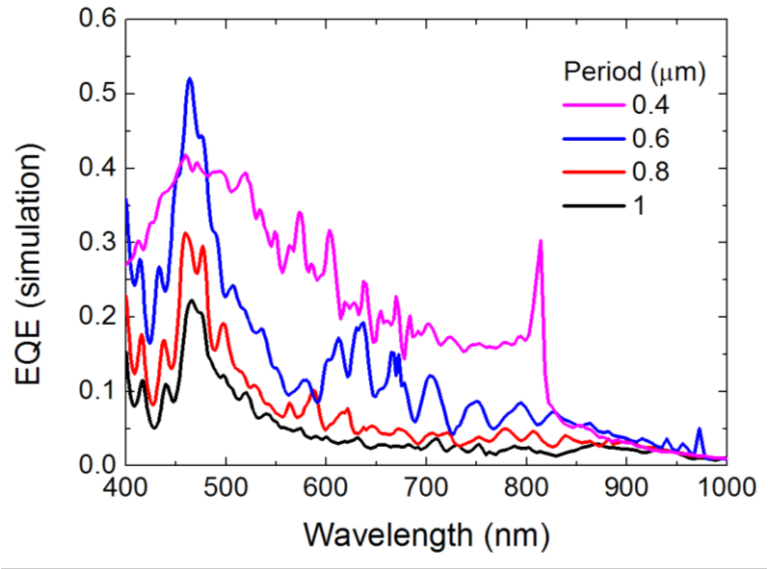

Figure 4.12 Simulated external quantum efficiencies for nanowire devices with different periods. Radii of the nanowires are 80 nm. Heights of nanowires are 2.7 μm.

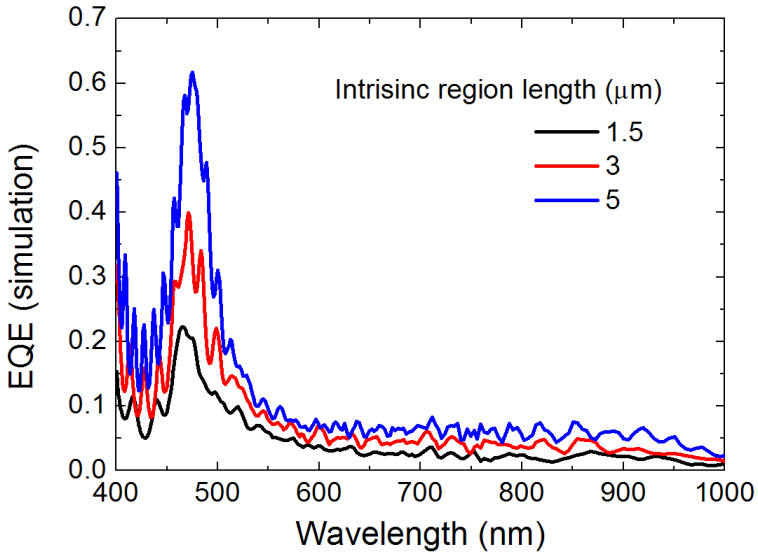

Figure 4.13 Simulated external quantum efficiencies (EQEs) for nanowire devices with different intrinsic region lengths. Radii of the nanowires are 80 nm. Period is 1 μm.

In Figure 4.11 (inset), the simulated external quantum efficiency is shown for the case that the nanowires are embedded in air, rather than PMMA. The HE_{11} mode can be seen to generate strong absorption peak at $\lambda \approx 700$ nm. This peak is suppressed when the nanowires are in PMMA. It is for this reason that we use higher order absorption peaks, rather than the HE_{11} mode, despite the fact that they produce multiple absorption peaks in the visible range.

4.3 Color imaging with nanowire based photodetectors

Imaging experiments are performed using the nanowire-based photodetectors. In Figure 4.14, the ideal response of the CIE (1964) 10-deg color matching functions is shown.[74] We choose a linear combination of the signals from the four nanowires arrays (Figure 4.10) to achieve a response similar to the standard color response of Figure 4.14. It can be seen that there are differences between the standard response (Figure 4.14(a)) and that of our device (Figure 4.14(b)) because of the multiple peak nature of the responsivities of our devices (Figure 4.10). We assign channels VIS1-3 to be the red, green and blue (RGB) channels, respectively. In Figure 4.15, images of the Macbeth ColorChecker card[75] obtained with our nanowire-based imaging system are shown. These are obtained by recording photocurrents from the four nanowire photodetector arrays as the device is mechanically translated in a 180 × 128 array.

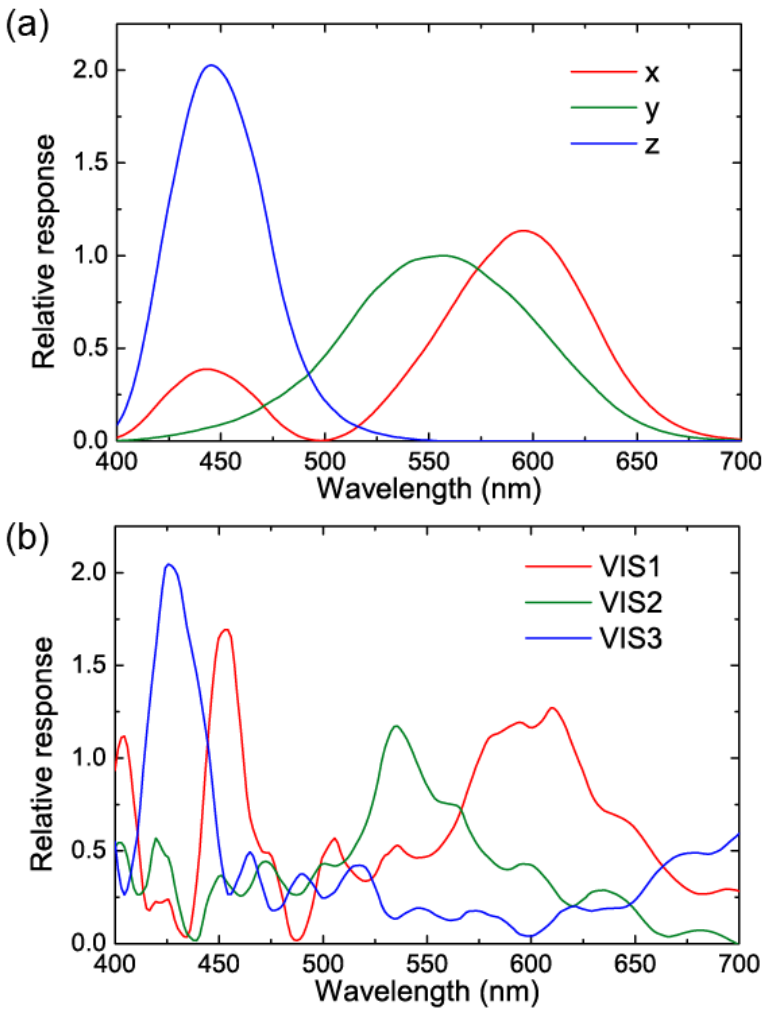

Figure 4.14 (a) CIE 1964 XYZ color matching functions. (b) Channels VIS 1-3 represent linear combination of four relative responses (R = 80 nm, 100 nm, 120 nm, 140 nm). Linear combination is chosen to achieve result similar to standard color responses.

A lens (Pentax) with a focal length of 50 mm and operated at an f-number of 2.0 is used for the imaging experiments. The light source consists of three daylight compact fluorescent light bulbs (CFL 30W, EiKO). Mechanical scanning of the device is carried out (180 × 128 positions) using two motorized stages (T-LSM050A, Zaber Technologies). The scanning step

is 142.875 μm. The overall extent of the scanned area is 25.57 mm × 18.15 mm. For the linear RGB image, we assign channels VIS1, VIS2 and VIS3 as corresponding to red, green and blue. This linear RGB image is then multiplied by a color correction matrix. Gamma correction of 1 / 2.2 is then applied. The color correction matrix is found by imaging the Macbeth ColorChecker card (ColorChecker Classic, X-Rite) and extracting the linear RGB values of the 24 color patches of the acquired image. The matrix that transforms these to the desired linear RGB values with minimum error is then found.

We combine the images obtained by the nanowire photodetector arrays (Figure 4.15(a-d)) to obtain a linear RGB image. We then apply color correction and gamma correction (Figure 4.15(e)). The resultant color image produced by our nanowire-based photodetector can be seen to be similar to the actual color chart. The measured RMS color difference ΔE*ab of the 24 color patches is 22.28.[74, 76] We also take the image of a scene of test objects with our device. Figure 4.16(a) shows the color corrected image. It can be seen that this is very similar to that obtained with a conventional camera (Figure 4.16(b)), with the slight differences due to the spectral response of our device (Figure 4.14(b)) not being perfectly matched to the standard response (Figure 4.14(a)).

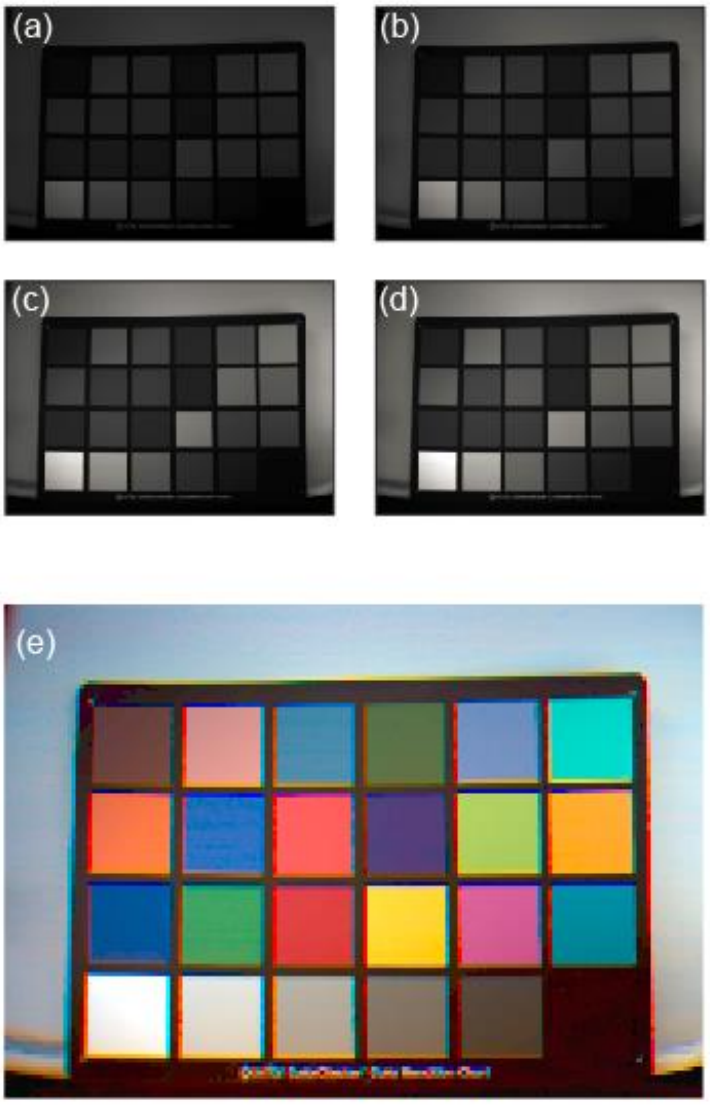

Figure 4.15 Images captured by our nanowire arrays. (a) R = 80 nm (b) R = 100 nm (c) R = 120 nm (d) R = 140 nm. (e) Color calibration and gamma correction are applied (gamma = 2.2) to linear RGB image to produced corrected image.

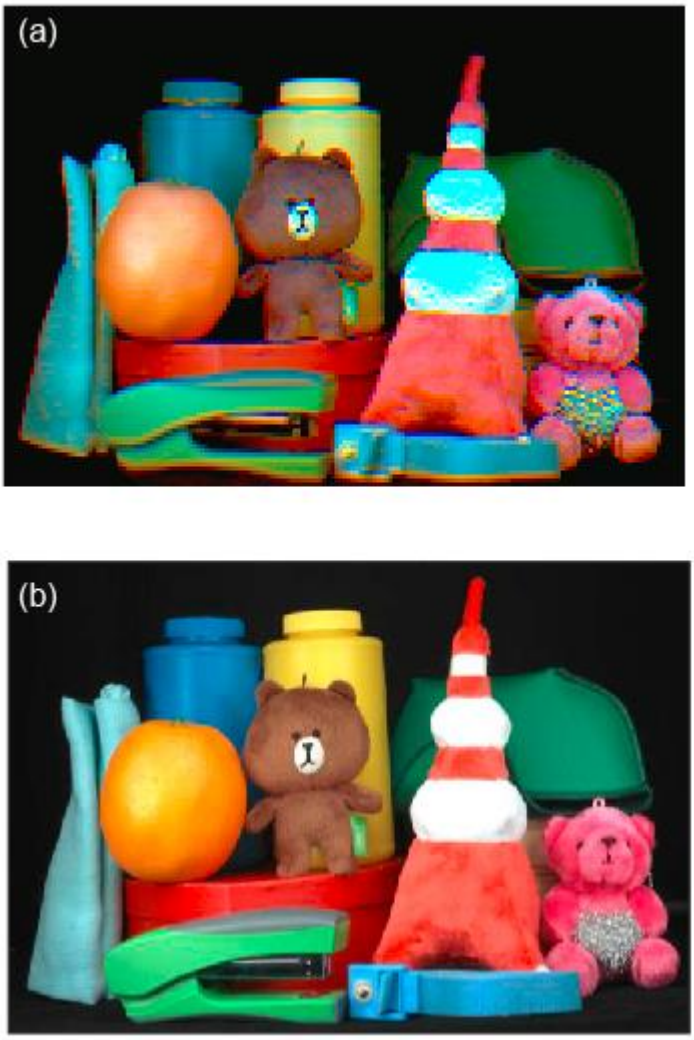

Figure 4.16 (a) Color image of test objects taken by our nanowire arrays. (b) Color image of test objects taken by conventional digital camera.

4.4 Conclusion

In conclusion, we have demonstrated filter-free color imaging using vertical silicon nanowire p-i-n photodetectors whose spectral responsivities are controlled by nanowire radius. Our method is not only simplifies the fabrication process, because the optical

responses of the color pixels are defined simultaneously through a single lithography step, but also opens the way to collect the photons that would be otherwise absorbed in conventional color filters. This method also presents the exciting opportunity for wideband multispectral imaging via the use of nanowires made from other semiconductor materials, for example heterogeneous epitaxial nanowires.[40]

Chapter 5

Elliptical silicon nanowire photodetectors for polarization-resolved imaging

In previous Chapter, we demonstrated color imaging using vertical silicon nanowire photodetectors. A key benefit of etched nanowire is that the nanowire's cross section, i.e. its shape and size, can be chosen at-will, being defined by lithography. Making use of this benefit, our group demonstrated lens elements - reconfigurable by polarization - that comprised amorphous silicon nanowires with elliptical cross sections.[92]

Here, we demonstrate vertical silicon nanowire photodetectors with elliptical cross sections. The elliptical nanowires have polarization dependent absorption, with the absorbed photons being converted to photocurrent and collected by integrated p-i-n junctions. We present measurements that show the polarization dependence of the responsivities of fabricated devices and perform polarization-resolved imaging. In our approach, no additional polarization filters, such as those based on metal wire grids and dichroic materials, are needed. Importantly, our approach is conceptually different from polarization imaging with

conventional polarization filters, as absorbed light in our case is not discarded, but rather converted to photocurrent. As we discuss later, this fundamental difference between this and previous approaches could be employed in future devices to achieve higher efficiency.

5.1 Vertical silicon nanowires photodetector with elliptical cross-section

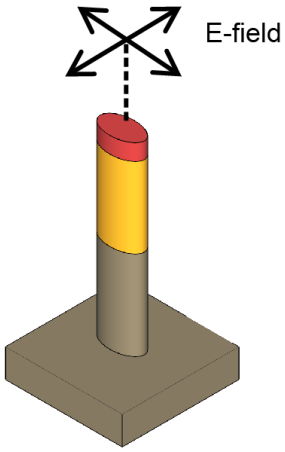

Figure 5.1 Schematic concept of photodetectors based on elliptical silicon nanowires. Nanowire's absorption depends on polarization state of incident light.

Figure 5.1 shows the operating principle of the device we introduce. The absorption spectrum of an elliptical nanowire depends on the polarization state of the illumination. We have previously shown [48, 93] that vertical silicon nanowires with circular cross sections exhibit absorption spectra containing peaks. The wavelength of each peak is highly

dependent on the nanowire's radius, being determined by interplay between the coupling coefficient and confinement factor of a mode supported by the nanowire. Due to symmetry, the absorption spectra of circular nanowires are polarization-independent. By contrast, for elliptical nanowires, the absorption spectra differ depending on whether the incident light is polarized along the long or short axis. We use this phenomenon for polarization-resolved imaging.

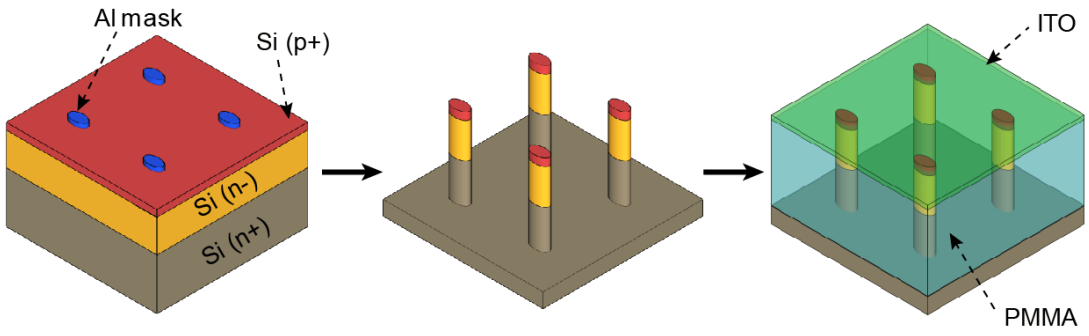

Figure 5.2 Fabrication process for elliptical silicon nanowire photodetectors. Epitaxially-grown n-/n+ wafer is doped p+ on top. Etch mask that comprises aluminum elliptical disks is patterned on wafer and dry etching is performed to fabricate vertical nanowires. PMMA spacer is fabricated and transparent top contact (ITO) is deposited.

Fabrication starts with an n-type silicon substrate on which an n- layer of epitaxial silicon has been grown (Figure 5.2). We dope the top surface of the n- epitaxial layer to p+ using a dopant diffusion process in a furnace. After removing the resultant thermal oxide, we spin coat polymethylmethacrylate (PMMA) to perform e-beam lithography to make arrays of

ellipse patterns. We fabricate an aluminum (Al, 40 nm) etch mask using metal evaporation followed by the lift-off process. We dry etch the wafer to form nanowires with a height of 2.7 μm. After removing aluminum mask using wet etching, PMMA is spin-coated onto the wafer with nanowires and cured. This PMMA layer is dry etched in an oxygen plasma until the tops of the nanowires are exposed. Indium tin oxide (ITO) with a thickness of 60 nm is then sputtered to deposit a transparent top electrical contact. We use the substrate as the bottom electrical contact.

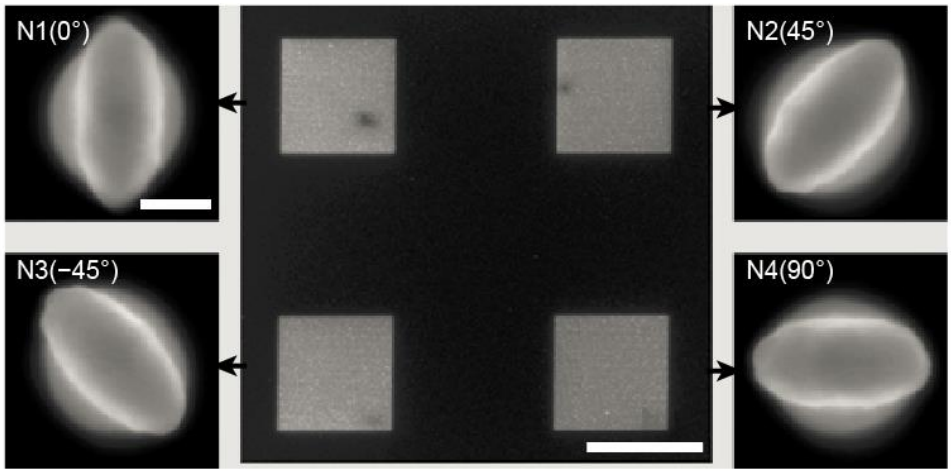

Figure 5.3 SEM image of elliptical nanowires after dry etching. Four arrays (each 100 x 100 nanowires) of elliptical nanowires with different orientation are fabricated (image in center). Scale bar is 100 μm. Magnified views (side images) of arrays (N1, N2, N3 and N4) show that constituent nanowires have different orientations (0°, 45°, -45°, 90°). Scale bar in magnified image is 100 nm.

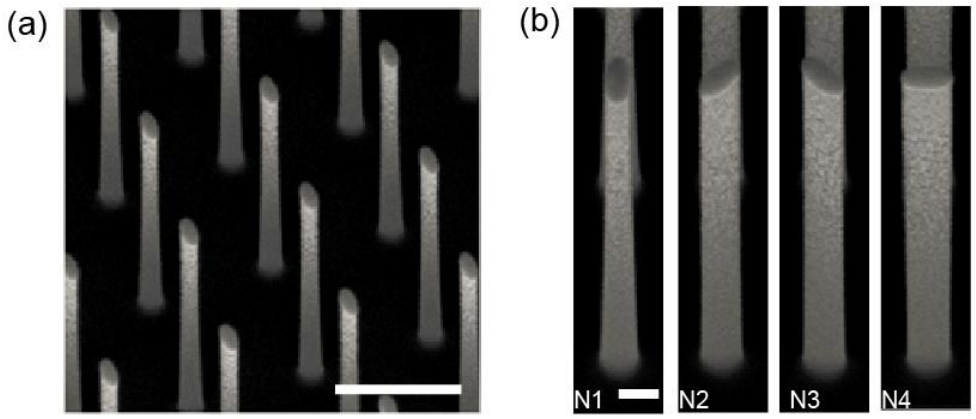

Figure 5.4 (a) 30° tilted view of elliptical nanowire array. Nanowires have heights of 2.7 μm. Scale bar is 1 μm. (b) Side view of nanowires from four arrays. Scale bar is 200 nm.

We fabricate four arrays of elliptical nanowires, each with its own orientation to calculate the first three Stokes parameters. These allow determination of angle of polarization (AOP) and degree-of-linear polarization (DOLP). The nanowire arrays are denoted N1(0°), N2(45°), N3(-45°) and N4(90°). The angle in parenthesis refers to the orientation of the elliptical nanowires of the array. Figures 5.3 and Figure 5.4 are scanning electron microscope (SEM) images of the elliptical silicon nanowires. The fabricated nanowires are 2.7 μm tall and are on a square array with a pitch of 1 μm. Each array has 100 × 100 elliptical nanowires with an extent of 100 μm × 100 μm. The elliptical cross-section of each nanowire has minor and major radii of 60 nm and 120 nm, respectively. The nanowires comprise vertical p-i-n junctions with p+/n-/n+ layers. Each layer has thicknesses of 200 nm / 1200 nm / 1300 nm. The color that each array appears depends on the orientation of the constituent elliptical nanowires and the polarization angle (Figure 5.5).

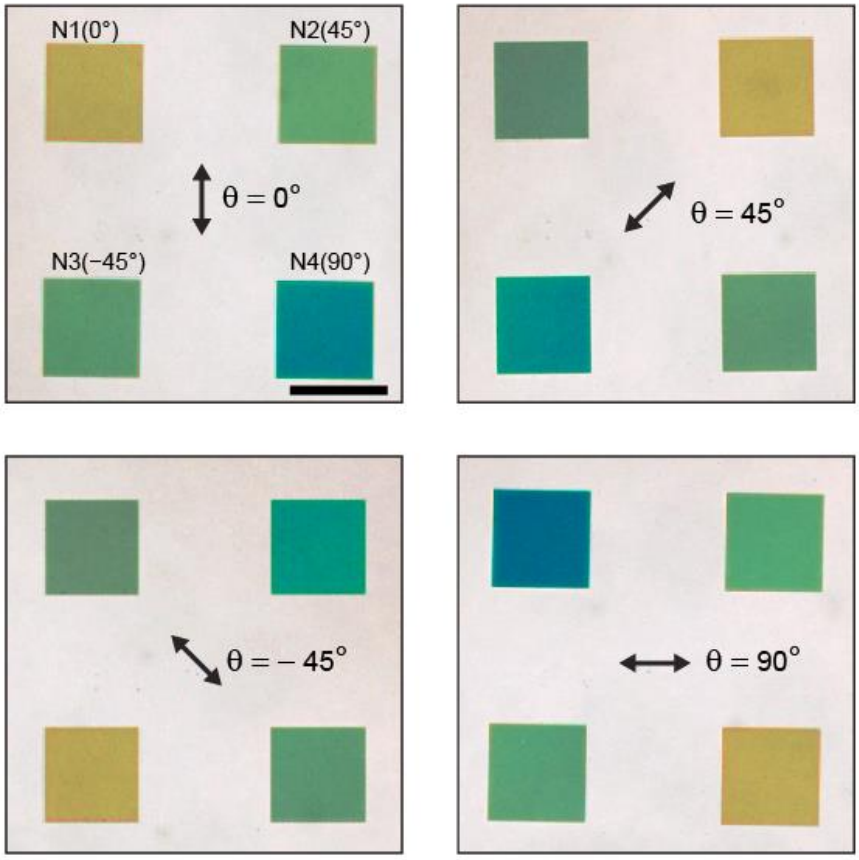

Figure 5.5 Optical microscope images of elliptical nanowire arrays, in reflection mode with linearly polarized illumination. Arrow indicates polarization of incident light (polarization angle θ = 0°, 45°, -45° and 90°). Color that each elliptical nanowire array appears depends on orientation of array and polarization angle of incident light. Scale bar is 100 μm.

5.2 Device characterization

We measure current-voltage (I-V) characteristics for fabricated nanowire arrays (Figure 5.6 and Figure 5.7). A general purpose sourcemeter (2400, Keithley) is used for the current-voltage curve measurements. We sweep the voltage from -1 V to 1 V in 0.01 V steps and measure the current. We use a He-Ne laser (λ=633 nm, Melles Griot) for the I-V measurements that are performed with illumination. These measurements are conducted in a dark environment at room temperature. The dark current is ~ 2 nA at a bias of -1V. Figure 5.7 shows measured I-V characteristics of the N4 array under dark and illuminated conditions. We next measure the photocurrent generated in response to linearly-polarized light provided by the combination of a monochromator (λ = 400-1000 nm, steps of 10 nm) and a linear polarization filter. To measure the responsivities of the devices, light from a monochromator (MS257, Oriel instruments) is focused into a pinhole (diameter: 200 μm), then passes through a polarizer (10GT04, Newport). The resultant linearly polarized light is focused onto the nanowire array using an objective lens (magnification 10×, NA 0.28, Mitutoyo). A 50:50 non-polarizing cube beam splitter is installed between the pinhole and polarizer in order for the light reflected from the nanowire device to be collected and imaged onto a charge-coupled device camera (DMK21AU04, Imaging Source). A picoammeter (6485, Keithley) measures photocurrent from the nanowire array. The power of the light incident on the nanowire device is measured with a reference photodetector.

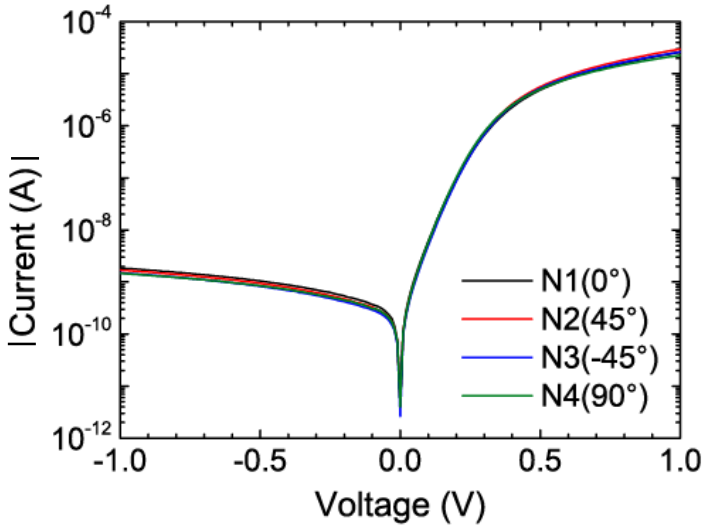

Figure 5.6 Log scale I-V curve of nanowire arrays in dark (no illumination).

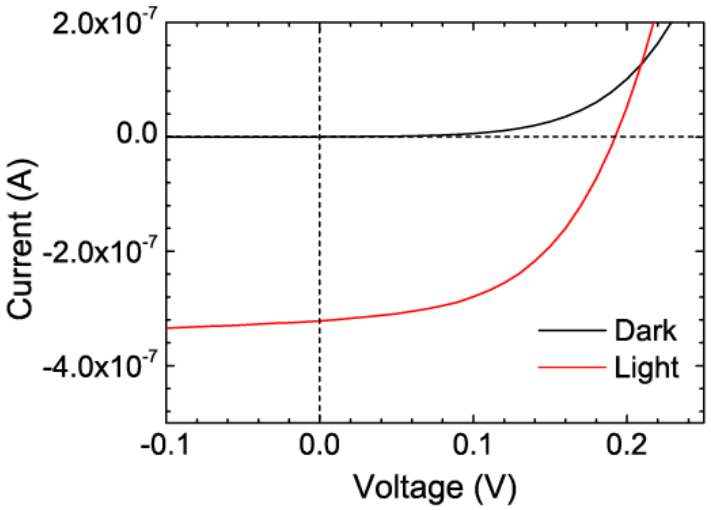

Figure 5.7 I-V curve of array N4 in dark and under illumination of 820 mW / cm^2 at a wavelength at 633 nm. Light is linearly polarized parallel to major axis of elliptical nanowires.

The photocurrent of the N1 array is measured by a pico-ammeter (0V bias: photovoltaic mode). It can be seen that the spectral response of the elliptical nanowires depends on the

polarization state of the incident light (Figure 5.8). We also perform finite-difference time-domain (FDTD) method simulations of the external quantum efficiency (QE), assuming an internal QE of 100% (Figure 5.9). We obtain reasonable agreement between the measured external QE lineshapes and external QE lineshapes simulated for elliptical nanowires with minor and major radii of 40 nm and 80 nm, respectively. That these dimensions differ from those of the actual devices could be due to fabrication imperfection. Comparison between measurements and simulations indicates that the internal quantum efficiency of our device is 20 %. That this is less than unity is attributed to surface recombination due to surface damage from the dry etching process.[88]

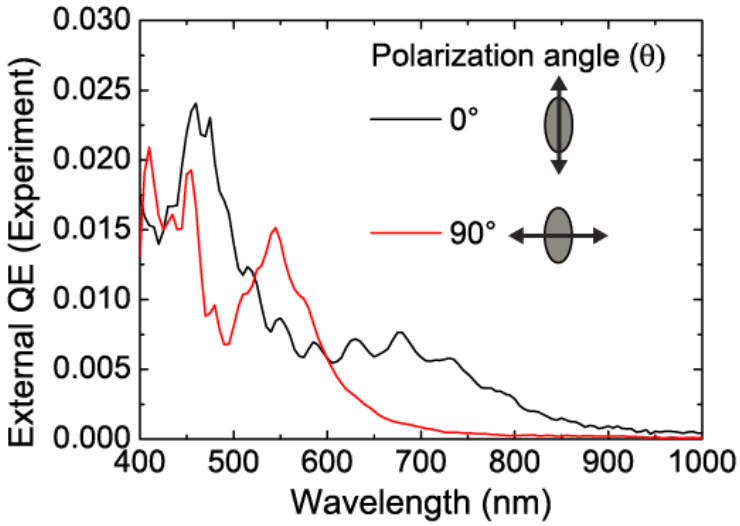

Figure 5.8 Measured external quantum efficiency (QE) spectra of array N1 under vertically- and horizontally-polarized illumination.

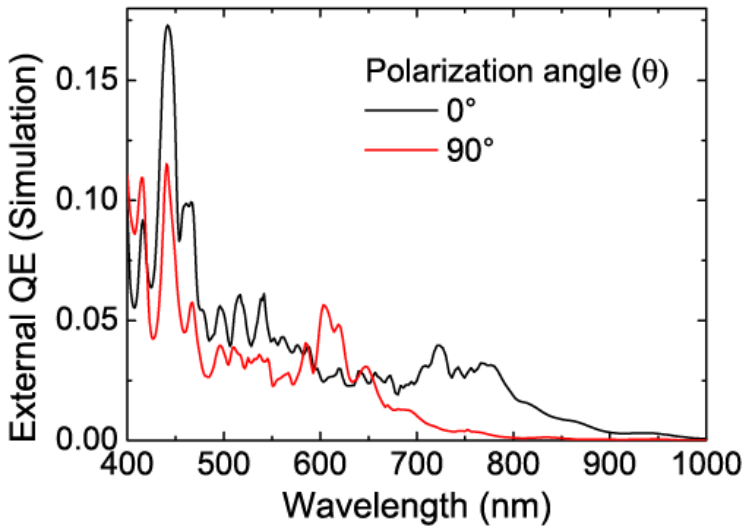

Figure 5.9 Simulated external QE spectra of array N1.

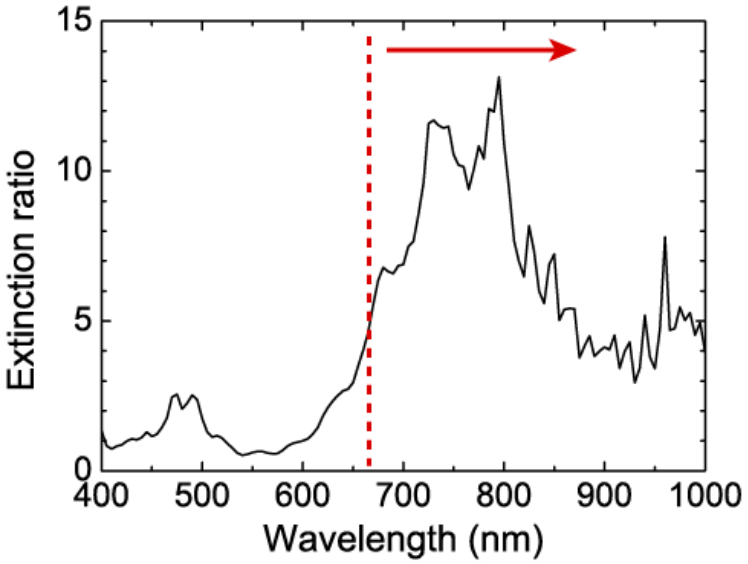

Figure 5.10 Extinction ratio calculated from measured external QE. Dotted line indicates cut off wavelength ($\lambda_{cut\text{-}off}$ = 665 nm) of long pass filter used in later experiments.

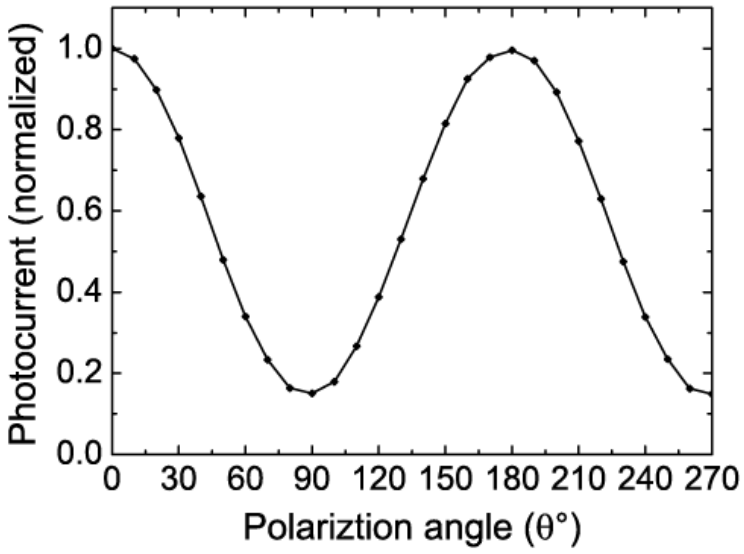

Figure 5.11 Normalized photocurrent at wavelength of 700 nm as a function of polarization angle θ.

From the measured QE spectra (Figure 5.8), we find the extinction ratio as the QE for light polarized along the nanowire's long axis divided by the QE for light polarized along the short axis. The results are shown as Figure 5.10. Because the nanowire array absorption depends on wavelength and has a multiple peak nature [48, 49, 81], the extinction ratio varies with the wavelength. It can be seen that the external QE of the array N1 under vertically polarized illumination is higher than that under horizontally polarized illumination in the wavelength range from 600 nm to 1000 nm. To demonstrate polarization-resolved imaging, we therefore install a long pass filter ($\lambda_{cut\text{-}off}$ = 665 nm) in front of our device. For λ > 655 nm, the elliptical nanowire photodetector has an extinction ratio exceeding 2.9. Figure 5.11 shows the normalized photocurrent of array N1 as a function of polarization angle

θ (illumination at λ=700 nm). It can be seen that the response approximately follows Malus's law, being approximately proportional to $\cos^2\theta$.

5.3 Polarization-resolved imaging with elliptical nanowire photodetector

Polarization-resolved imaging is performed using the elliptical nanowire photodetectors. We take images of 3-D glasses (Figure 5.12) that comprise pairs of orthogonal linear polarization filters (45°, -45°) by measuring photocurrents from the four elliptical nanowire photodetector arrays (N1, N2, N3 and N4) as they are mechanically translated in an array of 150 × 150 positions. A single-lens reflex (SLR) camera lens (focal length: 50 mm) operated at an f / 2.0 is used for imaging experiments. A long pass filter ($\lambda_{cut\text{-}off}$ = 665 nm, FGL665S, Thorlabs) is installed between the camera lens and the nanowire device. Two incandescent bulbs (60 W each) illuminate the front side of the 3-D glasses and one incandescent bulb (60 W) illuminates the back side of the 3-D glasses. Two motorized linear stages (T-LSM050A, Zaber Technologies) are used for scanning the nanowire device in a sequence of 150 × 150 positions with a scanning step of 119 μm. AOP and DOLP are calculated using the following equations. $DOLP = \sqrt{S_1^2 + S_2^2}/S_0$, $AOP = 1/2(\tan^{-1}(S_2/S_1))$. S_0, S_1, and S_2, are Stokes parameters. These are obtained from $S_0 = I(0^\circ) + I(90^\circ)$, $S_1 = I(0^\circ) - I(90^\circ)$ and

$S_2 = I(45^\circ) - I(-45^\circ)$ where $I(\theta)$ is electric field intensity transmitted through a polarization filter with orientation angle θ.

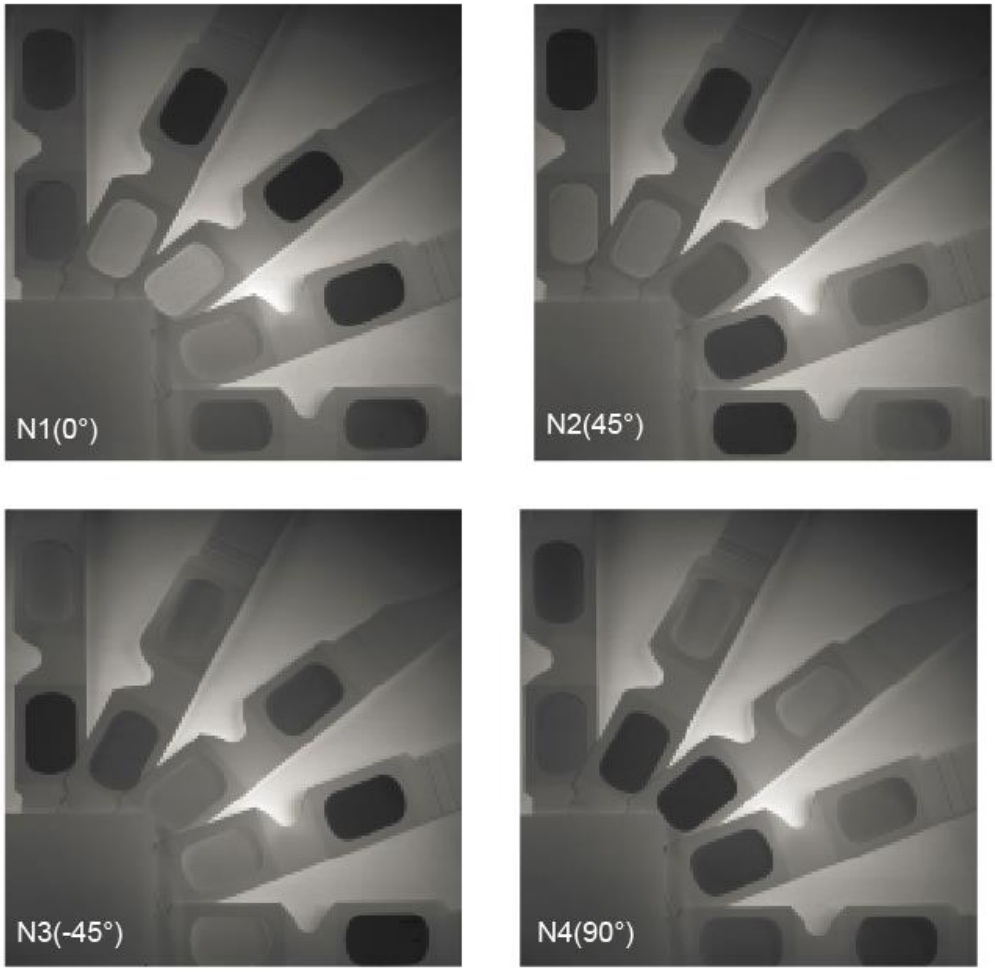

Figure 5.12 Polarization-resolved imaging using fabricated device. Images captured by nanowire arrays N1(0°), N2(45°), N3(-45°) and N4(90°).

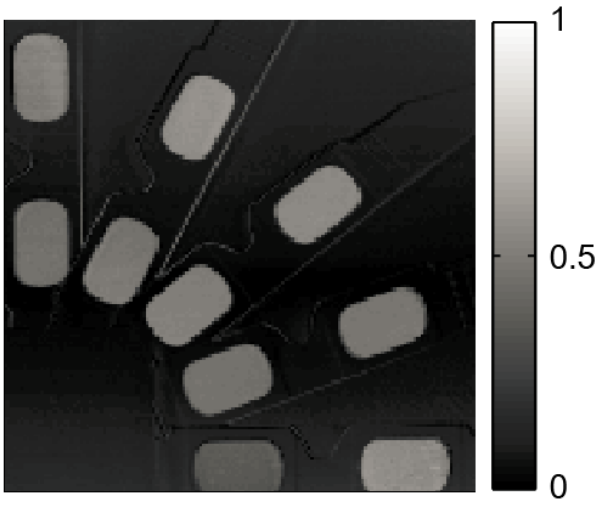

Figure 5.13 Degree-of-linear polarization (DOLP) image found from images.

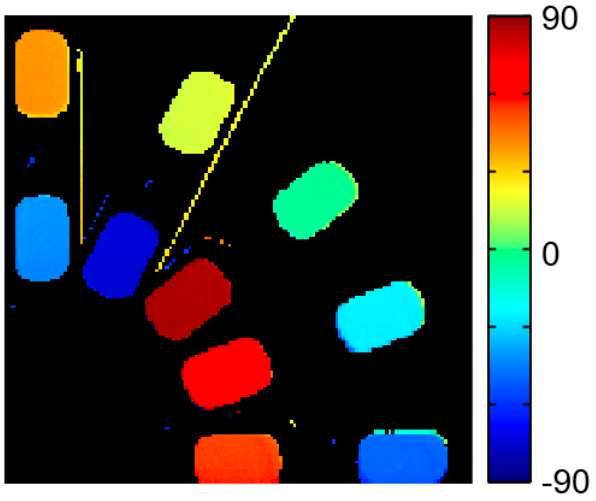

Figure 5.14 Angle of polarization (AOP) image found from images.

It can be clearly seen that each polarization filter of the 3-D glasses has a brightness that varies with the angle between its polarization axis and the orientation of the elliptical nanowires of the array. We next calculate the angle of polarization (AOP) and the degree of

linear polarization (DOLP). The polarization filters of the 3-D glasses are measured to exhibit high DOLP values as expected (Figure 5.13). The DOLP values measured by our nanowire devices (Figure 5.13) are lower than their true values however, due to the limited extinction ratio of our devices.[94] From Figure 5.14, it can be seen that the AOP images produced by our nanowire devices correctly display the orientations of the polarization axes of the filters of the 3-D glasses.

The most ubiquitous approach in which polarization is used to improve imaging contrast is that of polarized sunglasses. Glare from horizontal surfaces, e.g. water, is polarized parallel to these surfaces. In order to reduce this glare, polarized sunglasses therefore comprise filters that transmit vertical polarization. We next demonstrate that our elliptical nanowire photodetectors can achieve this functionality. Figure 5.15 shows the experimental setup. A tilted glass slide is situated near a piece of white cardboard attached to a vertical surface. Light can be reflected or scattered by the white cardboard and then reflected by the glass slide. This reflected light reduces the visibility of the object (coin) under the glass slide. For this experiments, two incandescent bulbs (60W each) are used for front side illumination. We then apply the gamma correction of 1 / 2.2 to the images taken by our nanowire device.

Figure 5.16 shows images taken by a conventional camera with horizontal and vertical polarization filters. When the horizontal polarization filter is used, the resultant image shows a strong reflection from the glass slide. By contrast, this reflected light is suppressed and the coin is clearly seen when the vertical polarization filter is used. We take images of the same scene using our elliptical nanowire photodetectors (Figure 5.17). In the image recorded by

array N1, the reflection from the glass slide is suppressed, and the visibility of the coin is enhanced.

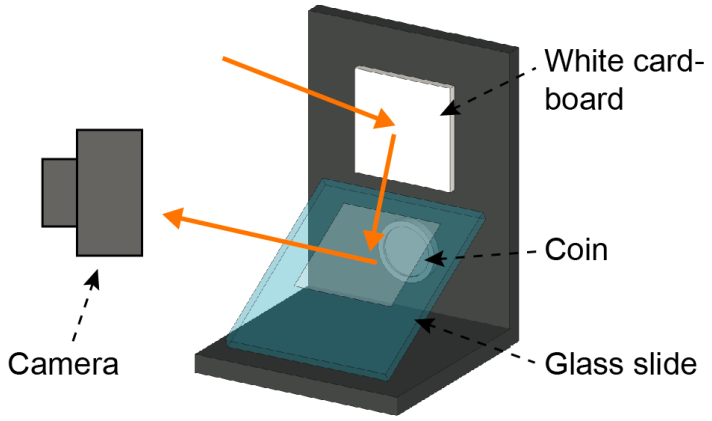

Figure 5.15 Schematic of experimental setup used for demonstrating polarization-resolved imaging with nanowire device. Coin below glass slide cannot be seen clearly due to strong reflection from glass.

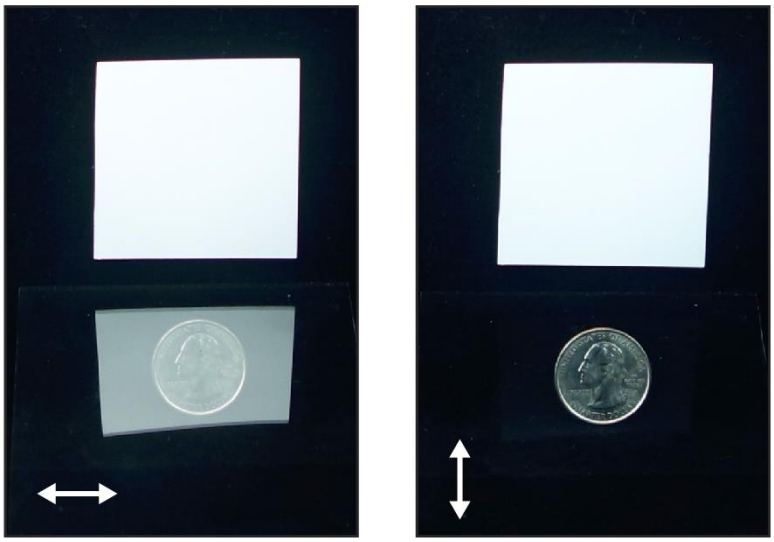

Figure 5.16 Image taken by conventional camera with horizontal and vertical polarization filters. Arrow indicates axis of polarization filter.

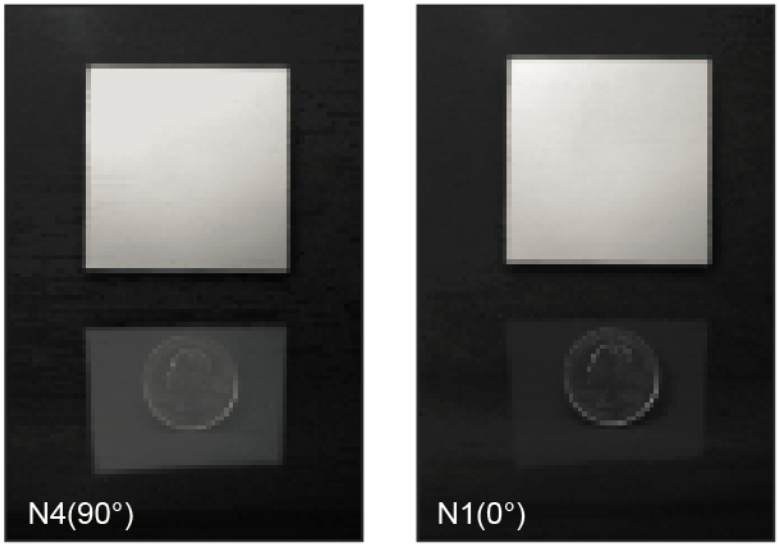

Figure 5.17 Images captured by our elliptical nanowire arrays N4(90°) and N1(0°). Gamma correction of 1 / 2.2 is applied.

5.4 Conclusion

In summary, we have demonstrated polarization-resolving photodetectors consisting of silicon nanowires with elliptical cross sections. Our approach is conceptually different from that employed in division-of-focal plane imaging polarimeters based on polarization filter arrays. In such devices, the unwanted polarization is discarded via absorption (or reflection) by the filter. By contrast, in our approach, absorbed light is converted to photocurrent. In our current configuration, the light not absorbed by the elliptical nanowires is largely transmitted into the substrate. The incorporation of a second photodetector in the substrate to convert this light to photocurrent would permit the compelling possibility of polarization-resolving pixels with very high efficiency.

Chapter 6

Implementation of substrate photodetector for higher efficiency

In the previous Chapters, we experimentally demonstrated color and polarization-resolved imaging using photodetectors incorporated into silicon nanowires. These nanowire photodetectors have the unusual and technologically-useful property that the spectral absorption can be engineered by changing the radii of the nanowires or by changing the cross-sectional shape. In this Chapter, we describe the demonstration of a more advanced configuration, in which a second photodetector is added to the substrate, i.e. beneath the nanowires. This could form the basis of an image sensor pixel in which part of the spectrum would be captured by the nanowire photodetector, and converted to photocurrent. The remainder of the spectrum would be captured by the substrate photodetector, and again converted to photocurrent. In this way, photon capture would be performed in a highly efficient manner, as photons would be not discarded by absorptive filters. Figure 6.1 shows the concept schematic of this dual photodetector device. The nanowire photodetector selectively absorbs part of spectrum and the substrate photodetector absorbs the light not absorbed by the nanowire.

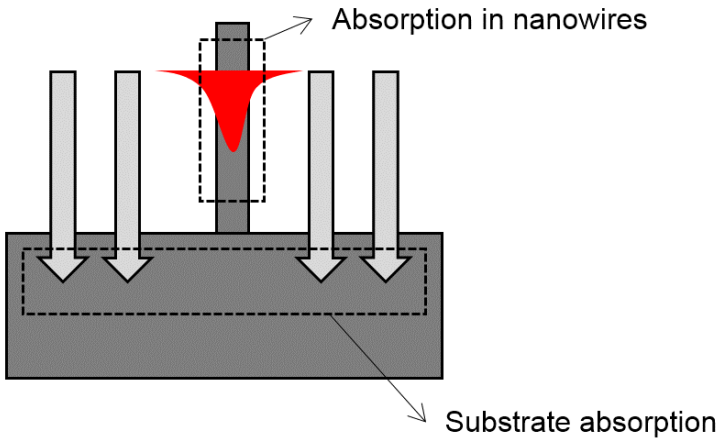

Figure 6.1 Schematic of dual photodetector device.

6.1 Fabrication of dual detector device

The starting substrate for our device is a silicon wafer on which multiple layers have been grown epitaxially. The use of an epi-wafer is motivated by the fact that to collect the photons from the nanowires and the substrate, both parts need to contain p-i-n junctions. Our multilayer epitaxial wafer contains p+/n-/n+/n-/p+ layers. Figure 6.2 shows the layers of the epitaxial wafer. Nanowire photodetectors are to be fabricated in the top p+/n-/n+ layers. The bottom n+/n-/p+ layers are for the bottom p-i-n junction. We ordered wafers from the company IQE Silicon (UK), providing to them the specification shown in Figure 6.3. The top p+/n-/n+ section thickness is 3.2 μm. This is chosen to match the intended heights of our nanowires. This is in turn dictated by the capabilities of our fabrication process, as to etch nanowires that are taller than this is challenging. For bottom photodetector, we choose the n-layer to be fairly thick (4 μm), in order to absorb as much of the light (not absorbed by the

nanowires) as possible. We measure the doping profile using secondary ion mass spectrometry (SIMS) performed by Evans Analytical Group (USA). The SIMS method use an ion beam to break apart materials, with mass spectroscopy performed on the atoms separated from the substrate. The measured depth profile (Figure 6.3) generally shows good agreement with the design that was provided to the manufacturer (Figure 6.2). The main difference is that rather than being completely abrupt, as indicated in the idealized schematic illustration of Figure 6.2, in the actual wafer there are transition regions at the junctions between the layers.

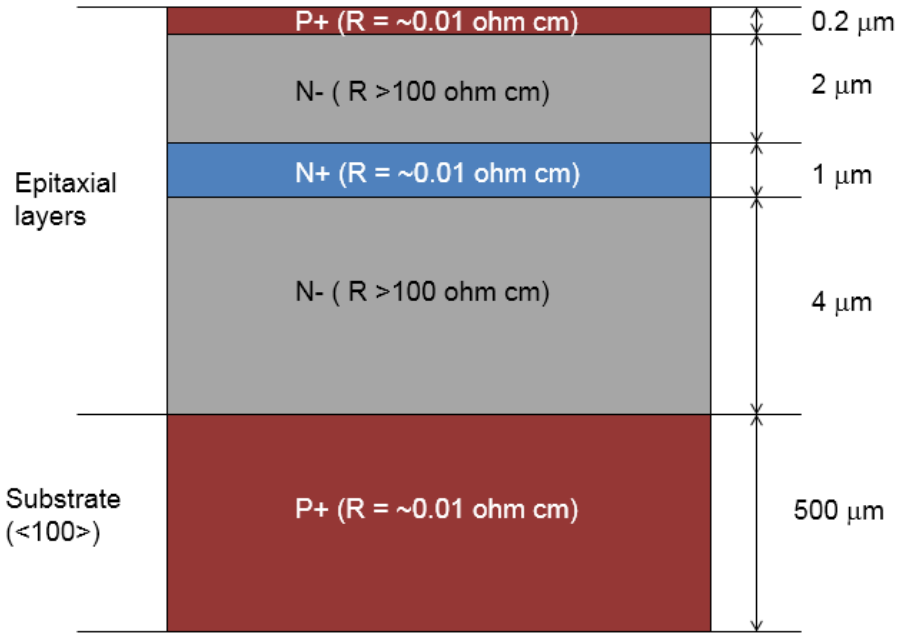

Figure 6.2 Design of epitaxial structure with p+/n-/n+/n-/p+ layers.

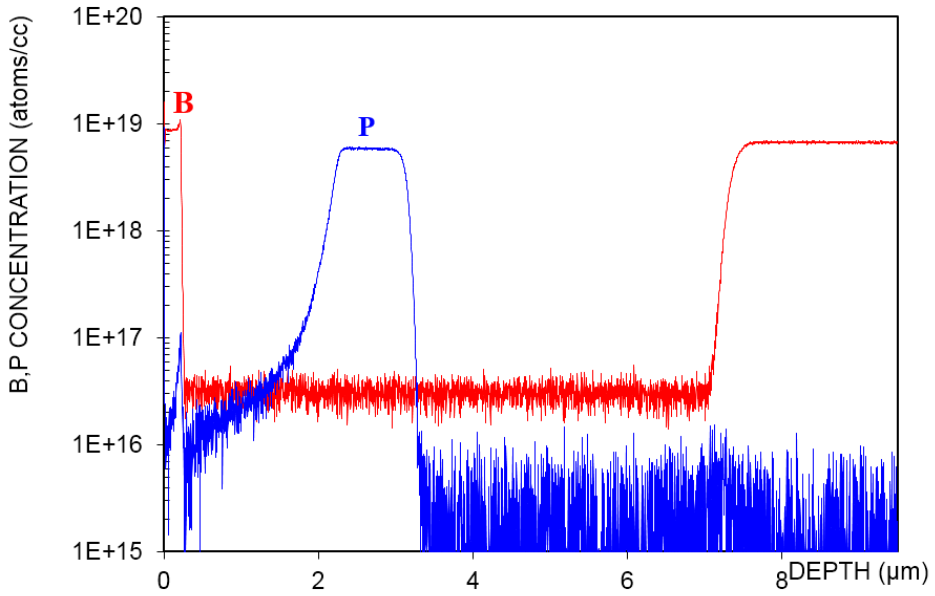

Figure 6.3 Depth profiling using SIMS. 'B' indicates the boron and 'P' indicates phosphorus.

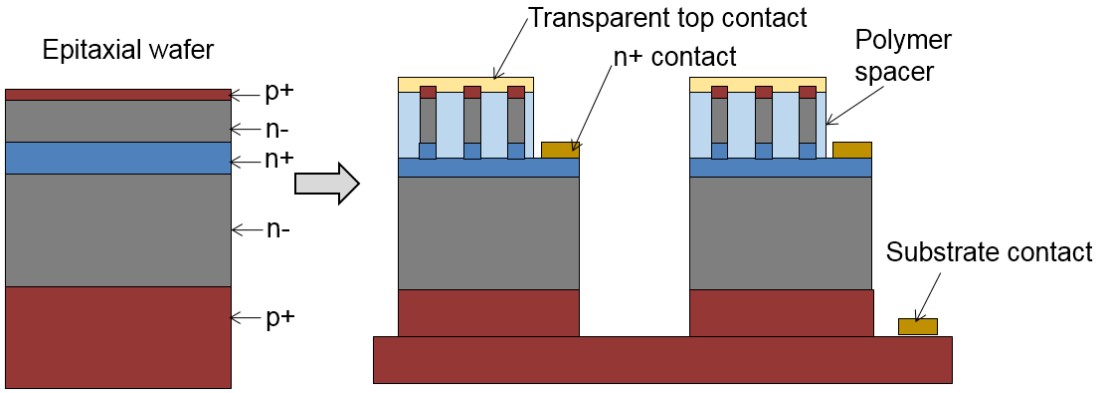

Figure 6.4 Schematic illustration of dual photodetector device: starting substrate (left) and final device (right).

In Figure 6.4, we provide a schematic illustration of the dual photodetector device. Fabrication begins with etching nanowires using the methods previously described in Chapters 4 and 5. It is important, however, that the etching depth be well-controlled to ensure that the resultant nanowires do indeed contain p+/n-/n+ junctions. We therefore choose to etch the nanowires until middle of the n+ layer. The next step is to define the substrate photodetector. We pattern thick photoresist (~4 μm thickness). We etch a mesa structure to a depth of ~8 μm, so that the substrate (p+) is exposed. This defines the substrate photodetector. We use deep reactive-ion etching (DRIE) for this process. The photoresist is then removed by a solvent stripper (PG Remover from MicroChem). As indicated in Figure 6.5, the device at this stage consists of etched nanowires formed on a mesa. The nanowires have heights of 2.6 μm and the height of mesa is 8.8 μm.(Figure 6.5(a)) Scanning electron micrographs (SEMs) of nanowires with radii of 80 nm are shown as Figure 6.5(b). We fabricate arrays of 100 x 100 nanowires with a pitch of 1 μm. The radii mentioned here are the design values in the electron beam lithography step. Scanning electron microscopy reveals that the nanowires are undercut. The SEM image in Figure 6.5(c) shows the mesa structure. The lateral extent of the mesa is 3mm x 3 mm. This size is chosen to permit PMMA spacer fabrication to be carried out. If the mesa is too small, then the PMMA coating will be very non-uniform. Figure 6.6 shows optical microscope images of the structures comprising nanowire arrays on mesas. It can be seen that, like the results of the previous Chapters, the nanowire arrays show vivid colors.

To fabricate the top transparent contact, we spin coat PMMA onto the sample. We then place the sample in an oxygen plasma in order to etch the PMMA and expose the tops of the

nanowires. An ITO layer is then sputtered on top. We use silver epoxy and gold wires to establish three contacts (ITO, n+ and substrate). The result is shown as Figure 6.7(a). The contact in the bottom right corner of Figure 6.7(b) corresponds to the n+ layer contact. This formed by scratching away the PMMA to expose the n+ layer.

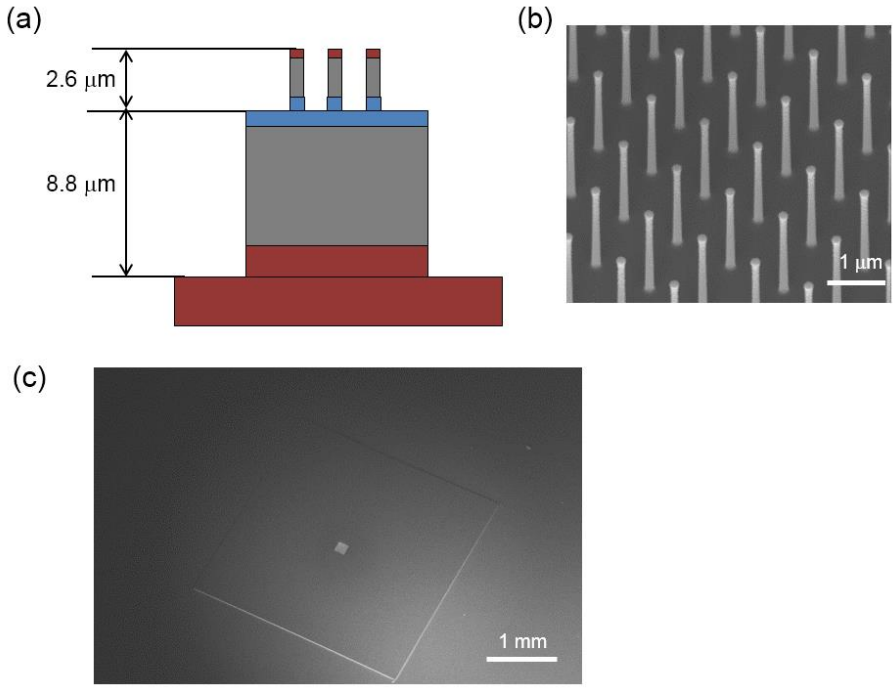

Figure 6.5 SEM image of etched structure. (a) height of nanowires and a mesa (b) etched nanowires (c) etched nanowires on a mesa structure.

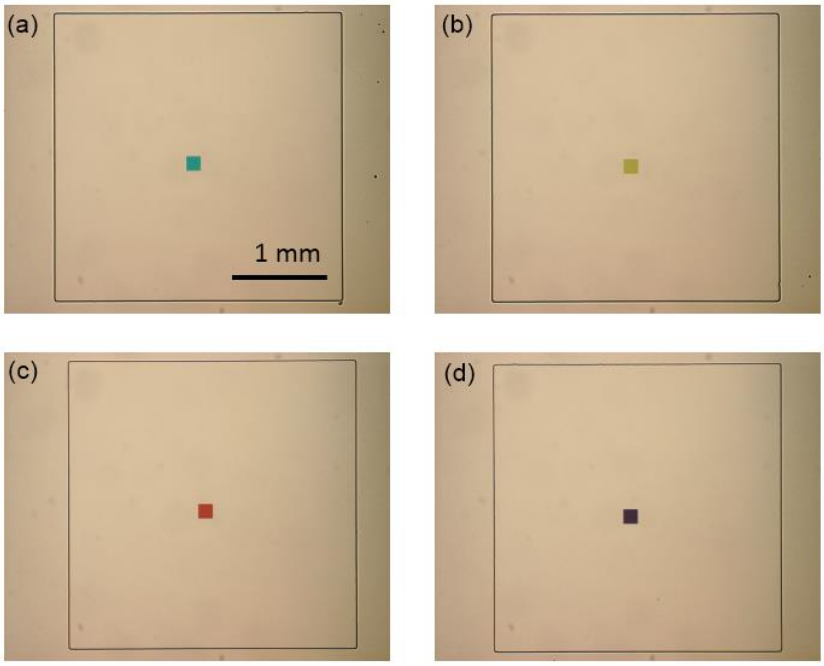

Figure 6.6 Optical microscope images of nanowire arrays fabricated on mesa structures that each contains a substrate photodetector. (a-d) arrays of nanowires with radii of 80 / 100 / 120 / 140 nm.

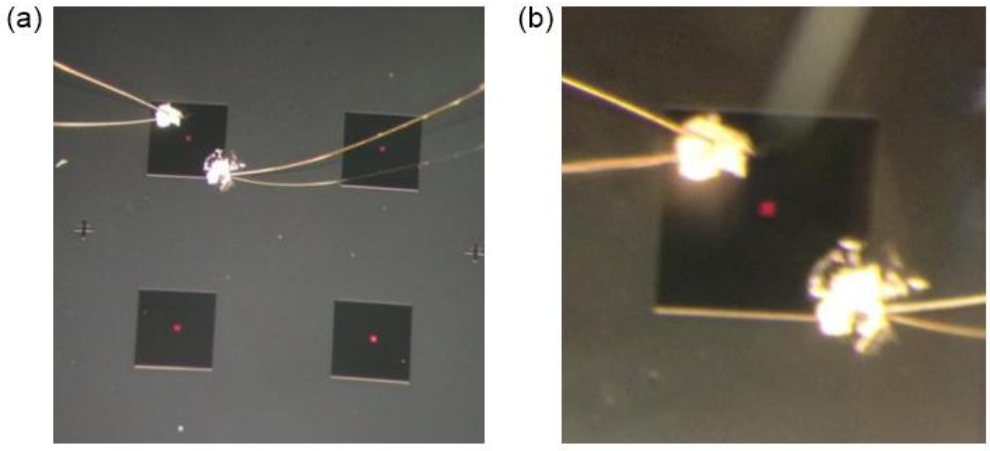

Figure 6.7 Wire bonding to fabricated device (a) wire bonding for the ITO and middle n+ layer (b) magnified view of the contact.

6.2 Measurement of fabricated device

We measure the responsivities of both the nanowire and substrate photodetectors using the method described in Chapter 4. The responsivity of the photodetector comprising nanowires with radii of 80 nm is shown in Figure 6.8. It can be seen that, like the devices of Chapters 4 and 5, the responsivity spectrum shows distinct peaks. The magnitude of the responsivity is however ~10 times smaller than that of previous devices. We believe that this is due to the changes in the etching characteristics of the ICP-RIE machine (STS) used for this work that occurred after the results of Chapters 4-5 were obtained. These changes to the etching characteristics resulted in increased damage to the nanowire surface. That the etching characteristics changed is evidenced by the fact that the nanowires have more strongly undercut profiles than before. By contrast the substrate photodetector (Figure 6.9) shows responsivity (~ 0.25) that can be considered good, being similar to that of a conventional silicon photodetector without an anti-reflection coating. However, the responsivity of substrate photodetector does not shows distinct dips that correspond to the absorption peaks of the nanowire. This is because light extinction due to the absorption in the nanowire is relatively small (~ 20 %). In addition, the ripples in the substrate photodetector's response make it harder to see.

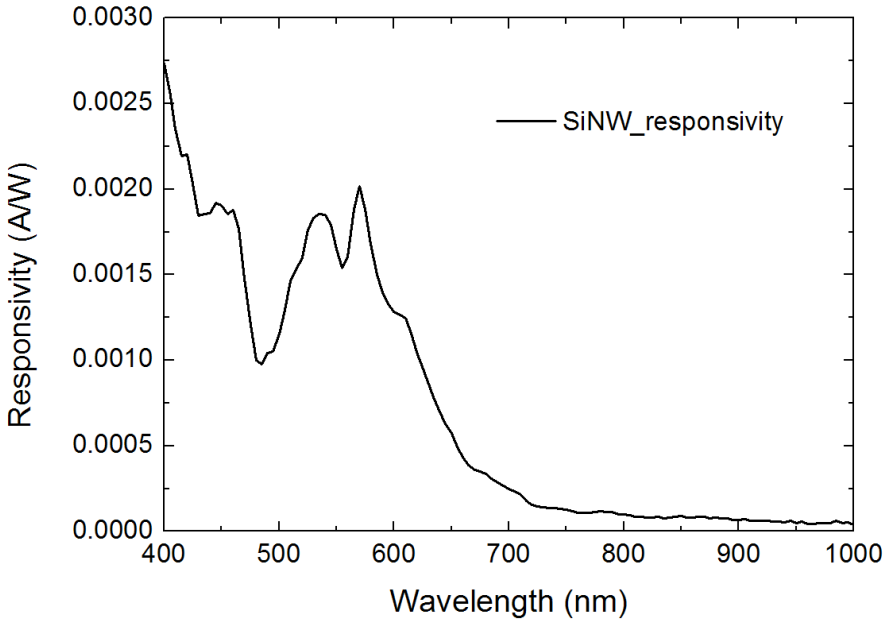

Figure 6.8 Responsivity of nanowire photodetector.

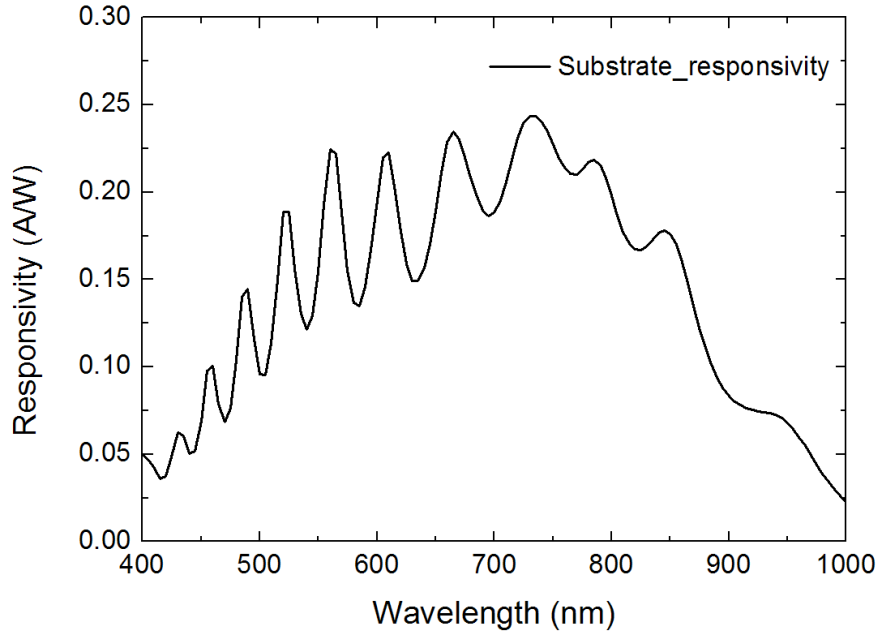

Figure 6.9 Responsivity of substrate photodetector.

As discussed above, the peak responsivity of the substrate photodetector (Figure 6.9) can be considered good. At short wavelengths, however, the responsivity is lower than that of an idealized device in which all incident photons are converted to photocurrent, due to the fact that the incident photons are absorbed near the top surface in the highly-doped n+ region (~500 nm thick) rather than being absorbed in the intrinsic (n- region) and generating electron-hole pairs that are collected. Similarly, the responsivity is lower at near-infrared wavelengths than that of an idealized device (in which all incident photons are converted to photocurrent) as the intrinsic region of the substrate photodetector is only ~4 μm thick. This means that the longer-wavelength photons have a tendency to exit the intrinsic region without being absorbed. Modulation of the responsivity spectrum of the substrate photodetector, i.e. ripples, can also be seen. This is because the PMMA film containing the embedded nanowires acts as a Fabry-Perot cavity, resulting in modulation of the spectrum of the light transmitted into the substrate.

To better understand the capabilities of the dual photodetector structure, we perform simulations of the light absorbed in different regions of the device (nanowires vs substrate). The simulation configuration is shown as Figure 6.10. We intentionally do not include the ITO layer and we assume that the PMMA layer is infinitely thick. This is done to remove the Fabry-Perot effect seen in Figure 6.9, in order to understand the device behavior that would occur were an anti-reflection coating used. Furthermore, we assume that the n+ and p+ regions of the nanowire have heights of 500 nm / 100 nm in each. The nanowire has a height of 2 μm, meaning that the intrinsic region therefore has a height of 1.4 μm. In finding the absorption spectrum of the nanowire, we consider the power absorbed in this region. The

simulation results are shown as Figure 6.11. Well-defined peaks can be seen in the absorption cross section spectrum of the nanowire at wavelengths of 410 nm and 520 nm. These result in dips in the substrate absorption cross section spectrum at these wavelengths. One can therefore regard the power absorbed in the nanowire as being analogous to the power absorbed in a photodetector of an image sensor containing a red-green-blue (RGB) Bayer filter. Similarly, the spectrum of power absorbed in the substrate (Figure 6.11) can be thought of as analogous to the power absorbed in a photodetector of an image sensor containing a cyan-magenta-yellow (CMY) filter. This approach should thus permit color imaging to be performed with high efficiency.

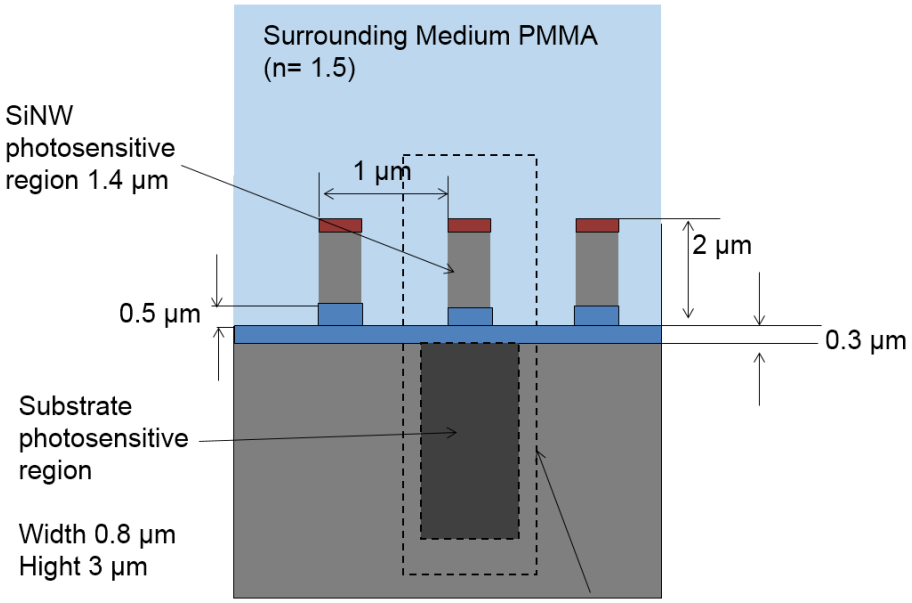

Figure 6.10 Simulation configuration. Radius of nanowire is 100 nm.

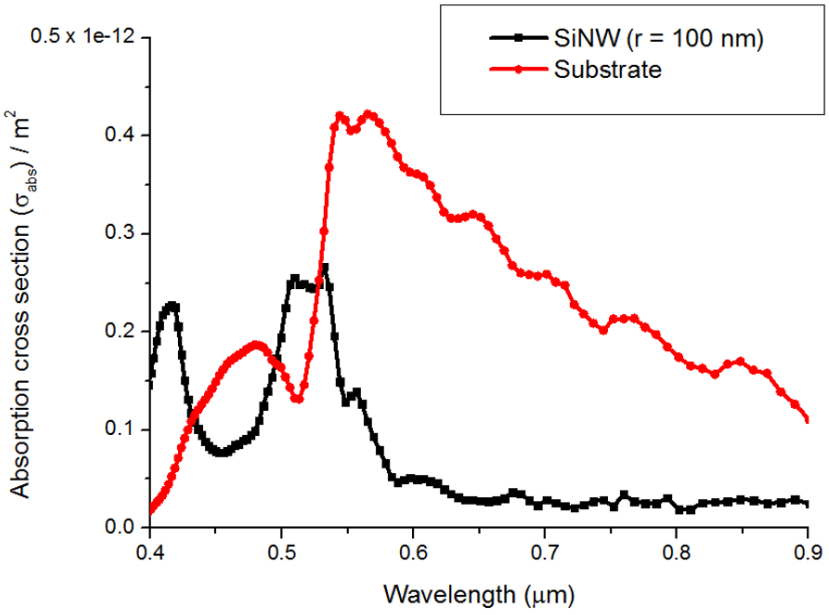

Figure 6.11 Absorption cross-section of nanowire photodetector and substrate photodetector.

6.3 Conclusion

We fabricate a dual photodetector device comprising silicon nanowires, each containing a photodetector, formed above a substrate that also contains a photodetector. The measured responsivities show that nanowire and substrate photodetectors each absorb parts of the spectrum of the illumination. Our approach enables us to collect photons, i.e. absorb and convert to photocurrent that would be otherwise discarded by conventional color filters.

References

[1] S. Yokogawa, S. P. Burgos and H. A. Atwater, "Plasmonic Color Filters for CMOS Image Sensor Applications," *Nano Letters,* vol. 12, 4349-4354 (2012).

[2] T. Xu, Y.-K. Wu, X. Luo and L. J. Guo, "Plasmonic nanoresonators for high-resolution colour filtering and spectral imaging," *Nature Communications,* vol. 1, 59 (2010).

[3] P. B. Catrysse and B. A. Wandell, "Integrated color pixels in 0.18 μm complementary metal oxide semiconductor technology," *Journal of the Optical Society of America A,* vol. 20, 2293-2306 (2003).

[4] S. Nishiwaki, T. Nakamura, M. Hiramoto, T. Fujii and M.-a. Suzuki, "Efficient colour splitters for high-pixel-density image sensors," *Nature Photonics.,* vol. 7, 248-254 (2013).

[5] R. B. Merrill, "Color separation in an active pixel cell imaging array using a triple-well structure," U.S. Patent 5,965,875 (1999).

[6] *Foveon*, Available: http://www.foveon.com/article.php?a=69 (Accessed September 10, 2014).

[7] D. L. Gilblom, S. K. Yoo and P. Ventura, "Operation and performance of a color image sensor with layered photodiodes," *AeroSense*, 318-331 (2003).

[8] J. F. Bell, S. W. Squyres, R. E. Arvidson, H. M. Arneson, D. Bass, W. Calvin, W. H. Farrand, W. Goetz, M. Golombek, R. Greeley, J. Grotzinger, E. Guinness, A. G. Hayes, M. Y. H. Hubbard, K. E. Herkenhoff, M. J. Johnson, J. R. Johnson, J. Joseph, K. M. Kinch, M. T. Lemmon, R. Li, M. B. Madsen, J. N. Maki, M. Malin, E. McCartney, S. McLennan, H. Y. McSween, D. W. Ming, R. V. Morris, E. Z. N. Dobrea, T. J. Parker, J. Proton, J. W. Rice, F. Seelos, J. M. Soderblom, L. A. Soderblom, J. N. Sohl-Dickstein, R. J. Sullivan, C. M. Weitz, and M. J. Wolff, "Pancam Multispectral Imaging Results from the Opportunity Rover at Meridiani Planum," *Science,* vol. 306, 1703-1709 (2004).

[9] M. O. Smith, S. L. Ustin, J. B. Adams and A. R. Gillespie, "Vegetation in deserts: I. A regional measure of abundance from multispectral images," *Remote Sensing of Environment,* vol. 31, 1-26 (1990).

[10] R. M. Levenson and J. R. Mansfield, "Multispectral imaging in biology and medicine: Slices of life," *Cytometry Part A*, vol. 69A, 748-758 (2006).

[11] B. Park, K. C. Lawrence, W. R. Windham and D. P. Smith, "Multispectral imaging system for fecal and ingesta detection on poul try carcasses," *Journal of Food Process Engineering*, vol. 27, 311-327 (2004).

[12] C. Hong, A. Koschan, M. Abidi, S. G. Kong and W. Chang-Hee, "Multispectral visible and infrared imaging for face recognition," *Computer Vision and Pattern Recognition Workshops (CVPRW)*, 1-6 (2008).

[13] F. Koenig and W. Praefcke, "Practice of multispectral image acquisition," *Proc. SPIE 3409, Electronic Imaging: Processing, Printing, and Publishing in Color*, vol. 34, 34-41 (1998).

[14] J. H. Everitt, D. E. Escobar, I. Cavazos, J. R. Noriega and M. R. Davis, "A three-camera multispectral digital video imaging system," *Remote Sensing of Environment*, vol. 54, 333-337 (1995).

[15] T. S. Hyvarinen, E. Herrala and A. Dall'Ava, "Direct sight imaging spectrograph: a unique add-on component brings spectral imaging to industrial applications," *Proc. SPIE 3409, Electronic Imaging: Processing, Printing, and Publishing in Color*, vol. 34, 165-175 (1998).

[16] J. Y. Hardeberg, F. Schmitt and H. Brettel, "Multispectral color image capture using a liquid crystal tunable filter," *Optical Engineering*, vol. 41, 2532-2548 (2002).

[17] G. A. Baone and H. Qi, "Demosaicking methods for multispectral cameras using mosaic focal plane array technology," *Proc. SPIE 6062, Spectral Imaging: Eighth International Symposium on Multispectral Color Science*, vol. 6062, 60620A (2006).

[18] Y. M. Lu, C. Fredembach, M. Vetterli and S. Susstrunk, "Designing color filter arrays for the joint capture of visible and near-infrared images," *IEEE International Conference on Image Processing (ICIP)*, 3797-3800 (2009).

[19] Q. Chen, D. Das, D. Chitnis, K. Walls, T. D. Drysdale, S. Collins and D. R. S. Cumming, "A CMOS Image Sensor Integrated with Plasmonic Colour Filters," *Plasmonics*, vol. 7, 695-699 (2012).

[20] A. Sweeney, C. Jiggins and S. Johnsen, "Insect communication: Polarized light as a butterfly mating signal," *Nature*, vol. 423, 31-32 (2003).

[21] T. Labhart, "Polarization-opponent interneurons in the insect visual system," *Nature*, vol. 331, 435-437 (1988).

[22] J. N. Lythgoe and C. C. Hemmings, "Polarized Light and Underwater Vision," *Nature*, vol. 213, 893-894 (1967).

[23] T. W. Cronin, N. Shashar, R. L. Caldwell, J. Marshall, A. G. Cheroske and T.-H. Chiou, "Polarization Vision and Its Role in Biological Signaling," *Integrative and Comparative Biology*, vol. 43, 549-558 (2003).

[24] V. Gruev, R. Perkins and T. York, "CCD polarization imaging sensor with aluminum nanowire optical filters," *Optics Express*, vol. 18, 19087-19094 (2010).

[25] S.-S. Lin, K. M. Yemelyanov, J. E. N. Pugh and N. Engheta, "Separation and contrast enhancement of overlapping cast shadow components using polarization," *Optics Express*, vol. 14, 7099-7108 (2006).

[26] J. O. Stenflo and H. Povel, "Astronomical polarimeter with 2-D detector arrays," *Applied Optics*, vol. 24, 3893-3898 (1985).

[27] W. Groner, J. W. Winkelman, A. G. Harris, C. Ince, G. J. Bouma, K. Messmer and R. G. Nadeau, "Orthogonal polarization spectral imaging: A new method for study of the microcirculation," *Nature Medicine*, vol. 5, 1209-1212 (1999).

[28] E. Salomatina-Motts, V. A. Neel and A. N. Yaroslavskaya, "Multimodal polarization system for imaging skin cancer," *Optics and Spectroscopy*, vol. 107, 884-890 (2009).

[29] Z. Nan, J. Xiaoyu, G. Qiang, H. Yonghong and M. Hui, "Linear polarization difference imaging and its potential applications," *Applied Optics*, vol. 48, 6734-6739 (2009).

[30] J. S. Tyo, M. P. Rowe, E. N. Pugh and N. Engheta, "Target detection in optically scattering media by polarization-difference imaging," *Applied Optics*, vol. 35, 1855-1870 (1996).

[31] M. P. Rowe, J. S. Tyo, N. Engheta and E. N. Pugh, "Polarization-difference imaging: a biologically inspired techniquefor observation through scattering media," *Optics Letters*, vol. 20, 608-610 (1995).

[32] L. B. Wolff, T. A. Mancini, P. Pouliquen and A. G. Andreou, "Liquid crystal polarization camera," *IEEE Transactions on Robotics and Automation*, vol. 13, 195-203 (1997).

[33] A. G. Andreou and Z. K. Kalayjian, "Polarization imaging: principles and integrated polarimeters," *IEEE Sensors Journal*, vol. 2, 566-576 (2002).

[34] Z. Xiaojin, F. Boussaid, A. Bermak and V. G. Chigrinov, "Thin Photo-Patterned Micropolarizer Array for CMOS Image Sensors," *IEEE Photonics Technology Letters*, vol. 21, 805-807 (2009).

[35] V. Gruev, A. Ortu, N. Lazarus, J. Van der Spiegel and N. Engheta, "Fabrication of a dual-tier thin film micropolarization array," *Optics Express*, vol. 15, 4994-5007 (2007).

[36] M. Kulkarni and V. Gruev, "Integrated spectral-polarization imaging sensor with aluminum nanowire polarization filters," *Optics Express*, vol. 20, 22997-23012 (2012).

[37] M. Law, J. Goldberger and P. Yang, "Semiconductor nanowires and nanotubes," *Annual Review of Materials Research*, vol. 34, 83-122 (2004).

[38] J. Hu, T. W. Odom and C. M. Lieber, "Chemistry and Physics in One Dimension: Synthesis and Properties of Nanowires and Nanotubes," *Accounts of Chemical Research*, vol. 32, 435-445 (1999).

[39] Z. Fan, H. Razavi, J.-W. Do, A. Moriwaki, O. Ergen, Y.-L. Chueh, P. W. Leu, J. C. Ho, T. Takahashi, L. A. Reichertz, S. Neale, K. Yu, M. Wu, J. W. Ager, and A. Javey, "Three-dimensional nanopillar-array photovoltaics on low-cost and flexible substrates," *Nature Materials*, vol. 8, 648-653 (2009).

[40] J. C. Shin, K. H. Kim, K. J. Yu, H. Hu, L. Yin, C.-Z. Ning, J. A. Rogers, J.-M. Zuo and X. Li, "InxGa1-xAs Nanowires on Silicon: One-Dimensional Heterogeneous Epitaxy, Bandgap Engineering, and Photovoltaics," *Nano Letters*, vol. 11, 4831-4838 (2011).

[41] J. Ahn, H.-S. Kim, K. J. Lee, S. Jeon, S. J. Kang, Y. Sun, R. G. Nuzzo and J. A. Rogers, "Heterogeneous Three-Dimensional Electronics by Use of Printed Semiconductor Nanomaterials," *Science*, vol. 314, 1754-1757 (2006).

[42] G. Zheng, W. Lu, S. Jin and C. M. Lieber, "Synthesis and Fabrication of High-Performance n-Type Silicon Nanowire Transistors," *Advanced Materials*, vol. 16, 1890-1893 (2004).

[43] R. S. Wagner and W. C. Ellis, "Vapor-liquid-solid mechanism of single crystal growth," *Applied Physics Letters*, vol. 4, 89-90 (1964).

[44] A. I. Hochbaum, R. Fan, R. He and P. Yang, "Controlled Growth of Si Nanowire Arrays for Device Integration," *Nano Letters,* vol. 5, 457-460 (2005).

[45] B. M. Kayes, M. A. Filler, M. C. Putnam, M. D. Kelzenberg, N. S. Lewis and H. A. Atwater, "Growth of vertically aligned Si wire arrays over large areas with Au and Cu catalysts," *Applied Physics Letters,* vol. 91, 103110 (2007).

[46] L. Cao, J. S. White, J.-S. Park, J. A. Schuller, B. M. Clemens and M. L. Brongersma, "Engineering light absorption in semiconductor nanowire devices," *Nature Materials,* vol. 8, 643-647 (2009).

[47] L. Cao, J.-S. Park, P. Fan, B. Clemens and M. L. Brongersma, "Resonant Germanium Nanoantenna Photodetectors," *Nano Letters,* vol. 10, 1229-1233 (2010).

[48] K. Seo, M. Wober, P. Steinvurzel, E. Schonbrun, Y. Dan, T. Ellenbogen and K. B. Crozier, "Multicolored Vertical Silicon Nanowires," *Nano Letters,* vol. 11, 1851-1856 (2011).

[49] B. Wang and P. W. Leu, "Tunable and selective resonant absorption in vertical nanowires," *Optics Letters,* vol. 37, 3756-3758 (2012).

[50] B. Tian, X. Zheng, T. J. Kempa, Y. Fang, N. Yu, G. Yu, J. Huang and C. M. Lieber, "Coaxial silicon nanowires as solar cells and nanoelectronic power sources," *Nature,* vol. 449, 885-889 (2007).

[51] C. Yang, C. J. Barrelet, F. Capasso and C. M. Lieber, "Single p-Type/Intrinsic/n-Type Silicon Nanowires as Nanoscale Avalanche Photodetectors," *Nano Letters,* vol. 6, 2929-2934 (2006).

[52] F. Patolsky, B. P. Timko, G. Yu, Y. Fang, A. B. Greytak, G. Zheng and C. M. Lieber, "Detection, Stimulation, and Inhibition of Neuronal Signals with High-Density Nanowire Transistor Arrays," *Science,* vol. 313, 1100-1104 (2006).

[53] D. C. Duffy, J. C. McDonald, O. J. A. Schueller and G. M. Whitesides, "Rapid Prototyping of Microfluidic Systems in Poly(dimethylsiloxane)," *Analytical Chemistry,* vol. 70, 4974-4984 (1998).

[54] G. M. Whitesides, "The origins and the future of microfluidics," *Nature,* vol. 442, 368-373 (2006).

[55] D. Psaltis, S. R. Quake and C. Yang, "Developing optofluidic technology through the fusion of microfluidics and optics," *Nature,* vol. 442, 381-386 (2006).

[56] H. Schmidt and A. Hawkins, "Optofluidic waveguides: I. Concepts and implementations," *Microfluidics and Nanofluidics*, vol. 4, 3-16 (2008).

[57] E. Schonbrun, P. E. Steinvurzel and K. B. Crozier, "A microfluidic fluorescence measurement system using an astigmatic diffractive microlens array," *Optics Express*, vol. 19, 1385-1394 (2011).

[58] A. Orth, E. Schonbrun and K. B. Crozier, "Multiplexed pressure sensing with elastomer membranes," *Lab on a Chip*, vol. 11, 3810-3815 (2011).

[59] B. Kuswandi, Nuriman, J. Huskens and W. Verboom, "Optical sensing systems for microfluidic devices: A review," *Analytica Chimica Acta*, vol. 601, 141-155 (2007).

[60] O. Hofmann, X. Wang, A. Cornwell, S. Beecher, A. Raja, D. D. C. Bradley, A. J. deMello and J. C. deMello, "Monolithically integrated dye-doped PDMS long-pass filters for disposable on-chip fluorescence detection," *Lab on a Chip*, vol. 6, 981-987 (2006).

[61] H. Fudouzi and T. Sawada, "Photonic Rubber Sheets with Tunable Color by Elastic Deformation," *Langmuir*, vol. 22, 1365-1368 (2005).

[62] H. Fudouzi and Y. Xia, "Photonic Papers and Inks: Color Writing with Colorless Materials," *Advanced Materials*, vol. 15, 892-896 (2003).

[63] S. M. Wells, I. A. Merkulov, I. I. Kravchenko, N. V. Lavrik and M. J. Sepaniak, "Silicon Nanopillars for Field-Enhanced Surface Spectroscopy," *ACS Nano*, vol. 6, 2948-2959 (2012).

[64] K. E. Plass, M. A. Filler, J. M. Spurgeon, B. M. Kayes, S. Maldonado, B. S. Brunschwig, H. A. Atwater and N. S. Lewis, "Flexible Polymer-Embedded Si Wire Arrays," *Advanced Materials*, vol. 21, 325-328 (2009).

[65] J. M. Weisse, D. R. Kim, C. H. Lee and X. Zheng, "Vertical Transfer of Uniform Silicon Nanowire Arrays via Crack Formation," *Nano Letters*, vol. 11, 1300-1305 (2011).

[66] V. J. Logeeswaran, A. M. Katzenmeyer and M. S. Islam, "Harvesting and Transferring Vertical Pillar Arrays of Single-Crystal Semiconductor Devices to Arbitrary Substrates," *IEEE Transactions on Electron Devices*, vol. 57, 1856-1864 (2010).

[67] C. F. Bohren and D. R. Huffman, "Absorption and Scattering by a Sphere," in *Absorption and Scattering of Light by Small Particles*, Wiley-VCH Verlag GmbH, 2007.

[68] A. M. Cardenas-Valencia, J. Dlutowski, D. Fries and L. Langebrake, "Spectrometric Determination of the Refractive Index of Optical Wave Guiding Materials Used in Lab-On-a-Chip Applications," *Applied Spectroscopy,* vol. 60, 322-329 (2006).

[69] M. D. Henry, "ICP etching of silicon for micro and nanoscale devices," Ph.D. dissertation, California Institute of Technology, 2009.

[70] L. Cao, P. Fan, E. S. Barnard, A. M. Brown and M. L. Brongersma, "Tuning the Color of Silicon Nanostructures," *Nano Letters,* vol. 10, 2649-2654 (2010).

[71] H. Park, K. Seo and K. B. Crozier, "Adding colors to polydimethylsiloxane by embedding vertical silicon nanowires," *Applied Physics Letters,* vol. 101, 193107 (2012).

[72] H. C. Ko, M. P. Stoykovich, J. Song, V. Malyarchuk, W. M. Choi, C.-J. Yu, J. B. Geddes Iii, J. Xiao, S. Wang, Y. Huang, and J. A. Rogers, "A hemispherical electronic eye camera based on compressible silicon optoelectronics," *Nature,* vol. 454, 748-753 (2008).

[73] *ICX098BL datasheet*. Available: http://www.sony.net/Products/SC-HP/datasheet/01/data/E01409A3Z.pdf (Accessed September 10, 2014).

[74] G. Wyszecki and W. S. Stiles, *Color Science: Concepts and Methods, Quantitative Data and Formulae,* Wiley, New York, 1982.

[75] C. McCamy, H. Marcus and J. Davidson, "A color-rendition chart," *Journal of Applied Photographic Engineering,* vol. 2, 95-99 (1976).

[76] B. Tannenbaum, *Color Image Processing with* Available: MATLAB http://www.mathworks.com/matlabcentral/fileexchange/15552-color-image-processing-webinar-files (Accessed September 10, 2014).

[77] F. J. Kriegler, W. A. Malila, R. F. Nalepka and W. Richardson, "Preprocessing transformations and their effects on multispectral recognition," *Proceedings of the Sixth International Symposium on Remote Sensing of Environment,* 97-131 (1969).

[78] S. Süsstrunk and C. Fredembach, "Enhancing the Visible with the Invisible: Exploiting Near Infrared to Advance Computational Photography and Computer Vision," *SID Symposium Digest of Technical Papers,* vol. 41, 90-93 (2010).

[79] S. Kim, R. W. Day, J. F. Cahoon, T. J. Kempa, K.-D. Song, H.-G. Park and C. M. Lieber, "Tuning Light Absorption in Core/Shell Silicon Nanowire Photovoltaic Devices through Morphological Design," *Nano Letters,* vol. 12, 4971-4976 (2012).

[80] K. C. Balram and D. A. B. Miller, "Self-aligned silicon fins in metallic slits as a platform for planar wavelength-selective nanoscale resonant photodetectors," *Optics Express,* vol. 20, 22735-22742 (2012).

[81] B. C. P. Sturmberg, K. B. Dossou, L. C. Botten, A. A. Asatryan, C. G. Poulton, C. M. de Sterke and R. C. McPhedran, "Modal analysis of enhanced absorption in silicon nanowire arrays," *Optics Express,* vol. 19, A1067-A1081 (2011).

[82] H. Park and K. B. Crozier, "Multispectral imaging with vertical silicon nanowires," *Scientific Reports,* vol. 3, 2460 (2013).

[83] A. Zhang, H. Kim, J. Cheng and Y.-H. Lo, "Ultrahigh Responsivity Visible and Infrared Detection Using Silicon Nanowire Phototransistors," *Nano Letters,* vol. 10, 2117-2120 (2010).

[84] Y. Zhou, Y.-h. Liu, J. Cheng and Y.-H. Lo, "Bias Dependence of Sub-Bandgap Light Detection for Core–Shell Silicon Nanowires," *Nano Letters,* vol. 12, 5929-5935 (2012).

[85] R. F. Egerton, P. Li and M. Malac, "Radiation damage in the TEM and SEM," *Micron,* vol. 35, 399-409 (2004).

[86] B. Fowler, C. Liu, S. Mims, J. Balicki, W. Li, H. Do and P. Vu, "Low-light-level CMOS image sensor for digitally fused night vision systems," *Proc. SPIE,* vol. 7298, 72981D (2009).

[87] S. Schaefer and R. Ludemann, "Low damage reactive ion etching for photovoltaic applications," *Journal of Vacuum Science & Technology A,* vol. 17, 749-754 (1999).

[88] D. Misra and E. L. Heasell, "Electrical damage to silicon devices due to reactive ion etching," *Semiconductor Science and Technology,* vol. 5, 229 (1990).

[89] X. Li, "Metal assisted chemical etching for high aspect ratio nanostructures: A review of characteristics and applications in photovoltaics," *Current Opinion in Solid State and Materials Science,* vol. 16, 71-81 (2012).

[90] O. Demichel, V. Calvo, A. Besson, P. Noé, B. Salem, N. Pauc, F. Oehler, P. Gentile and N. Magnea, "Surface Recombination Velocity Measurements of Efficiently Passivated Gold-Catalyzed Silicon Nanowires by a New Optical Method," *Nano Letters,* vol. 10, 2323-2329 (2010).

[91] Y. Dan, K. Seo, K. Takei, J. H. Meza, A. Javey and K. B. Crozier, "Dramatic Reduction of Surface Recombination by in Situ Surface Passivation of Silicon Nanowires," *Nano Letters,* vol. 11, 2527-2532 (2011).

[92] E. Schonbrun, K. Seo and K. B. Crozier, "Reconfigurable Imaging Systems Using Elliptical Nanowires," *Nano Letters,* vol. 11, 4299-4303 (2011).

[93] H. Park, Y. Dan, K. Seo, Y. J. Yu, P. K. Duane, M. Wober and K. B. Crozier, "Filter-Free Image Sensor Pixels Comprising Silicon Nanowires with Selective Color Absorption," *Nano Letters,* vol. 14, 1804-1809 (2014).

[94] T. York and V. Gruev, "Characterization of a visible spectrum division-of-focal-plane polarimeter," *Applied Optics,* vol. 51, 5392-5400 (2012).